

Dark Matter Phenomenology at Colliders

Dissertation
zur
Erlangung des Doktorgrades (Dr. rer. nat.)
der
Mathematisch-Naturwissenschaftlichen Fakultät
der
Rheinischen Friedrich-Wilhelms-Universität Bonn

von
ZHANG, Zhongyi
中一
aus
Peking, P.R. China
北京

Bonn, October 2019

Dieser Forschungsbericht wurde als Dissertation von der Mathematisch-Naturwissenschaftlichen Fakultät der Universität Bonn angenommen und ist auf dem Hochschulschriftenserver der ULB Bonn <https://nbn-resolving.org/urn:nbn:de:hbz:5-57633> elektronisch publiziert.

1. Gutachter: Prof. Manuel Drees
2. Gutachter: Prof. Herbert Dreiner

Tag der Promotion: 22.01.2020
Erscheinungsjahr: 2020

Abstract

Dark Matter candidates are required in physics beyond the Standard Model. The preferable models should not only explain the observed phenomena, but also be testable by experiments including direct detection, indirect detection, and collider searches. In this thesis, we focus on simplified Dark Matter models, and try to combine the experiments at colliders with non-collider data to scrutinize such models. On the theoretical side, the models considered in this thesis are the simplified Dark Matter models containing spinor or scalar Dark Matter particles and a massive vector mediator, which couples to both Dark Matter and Standard Model particles including quarks and leptons. On the experimental side, recent collider analyses related to the simplified Dark Matter models are mainly from ATLAS and CMS collaborations at LHC. Nevertheless, we also apply some old LEP data at e^+e^- collider to probe the parameter region where the LHC data are insensitive. The analyses used in this thesis cover collider signatures with mono-jet+ \cancel{E}_T , di-jet+ \cancel{E}_T , di-jet resonance, 4-jet, di-lepton+ \cancel{E}_T , and multi-lepton final states. However, the published analyses are not always well designed for the selected models related to Dark Matter. Therefore, we further study the optimization for the signal-to-background ratio and the selection efficiency for Dark Matter models, in order to improve the results from published analyses through both the cut based methods and the Machine Learning based algorithms.

Acknowledgements

I am very grateful for all the help during my PhD study in Bonn. I am really appreciate various kinds of support during the past year in both scientific research and personal life.

My greatest gratitude goes to my supervisor Manuel Drees. He offers me not only a series of support to step in the phenomenology research, but also many inspiring discussions on extensive topics inside or outside physics. Moreover, as a fan of caffeine, the coffee offered by him in workdays helps me enjoy my life in Bethe Center for Theoretical Physics. I am also very thankful to Professor Herbi Dreiner for spending time and effort on reading and refereeing my thesis, and to Ian Brock and Andreas Weber for joining my defence committee.

I have already studied in Bonn for 6 years summing up Master and PhD periods. During my study in Bonn, the lectures including Advanced Theoretical Particle Physics from Hans Peter Nilles, and Advanced Quantum Field Theory from Akaki Rusetsky impress me the most. The lecturers show the beauty of physics for me. Additionally, other lecture series, forums, and conferences in BCTP give me a wide knowledge of physics beyond my personal research area. Moreover, during the past 6 years, the financial support from Bonn Cologne Graduate School always helps me. I sincerely thank the support from BCGS for a foreigner.

My colleges in BCTP, including Jie Gu, Raghuvver Garani, Meng Shi, Yong Xu, etc., offer me a good work environment with interesting discussion and useful supports. In particular, Zeren Simon Wang helps me a lot through his multi-language talent, especially in German and English. I also thank the secretaries and other supporters in BCTP, containing Petra Weiss, Patricia Zündorf, Christa Börsch, Andreas Wißkirchen and all others.

I learnt Data Structure and Algorithms together with Yifan Wang in high school around 13 years ago. I am very glad that we can have a chance to discuss topics not only in computer science, but also in physics at Bonn and Cologne for years. His knowledge of quantum gravity widen my view of theoretical physics.

Turing to my life in Bonn, I usually enjoy dinners, beverages, and trips, or annually celebrate Chinese New Years with Jiaqi Cai, Wendan Li, and Fanyi Meng. I am really appreciated the impressive memory with them. Finally, as a super fan of alcoholic beverages, Bönnsch and Früh strongly improve the quality of my life during the past years. I would like to thank the great culture of beer in Germany.

List of Publications

The thesis contains results that have been published in

1. M. Drees and Z. Zhang,
“LHC Constraints on a Mediator Coupled to Heavy Quarks”,
arXiv:1903.00496 [hep-ph] [1].
2. M. Drees, M. Shi and Z. Zhang,
“Constraints on $U(1)_{L_\mu-L_\tau}$ from LHC Data”,
arXiv:1811.12446 [hep-ph] [2].
3. M. Drees and Z. Zhang,
“Constraints on a Light Leptophobic Mediator from LEP Data”,
arXiv:1805.02780 [hep-ph] [3].

Contents

I	The 1st Part: Overview	1
1	Introduction	3
1.1	Quantum Field Theory and Standard Model	3
1.2	Dark Matter	7
1.3	Simplified Model	8
1.4	Structure of the Thesis	9
2	Dark Matter	11
2.1	Evidence	12
2.1.1	Rotation Curves of Spiral Galaxies	12
2.1.2	Galaxy Clusters	12
2.1.3	Cosmic Microwave Background (CMB)	15
2.2	Relic Density	15
2.3	Direct Detection	16
2.4	Indirect Detection	17
2.5	Collider Searches	18
II	The 2nd Part: Leptophobic Mediator	25
3	Constraints on Leptonphobic Mediator from LEP data	27
3.1	Overview and Previous Researches	27
3.2	The Simplified Model	28
3.2.1	Lagrangian and Free Parameters	29
3.2.2	Dark Matter Constraints	29
3.2.3	Perturbativity Condition	32
3.2.4	Unitarity Condition	32
3.2.5	Summary: Free Parameters of the Model	33
3.3	Application of LEP Data	33
3.3.1	Two Jets Plus Missing Energy	34
3.3.2	Four Jet Analysis	39
3.4	Improved Analysis of LEP2 Data	41
3.5	Conclusions	54

4	Constraints on Leptophobic Mediator from LHC data	57
4.1	Overview and Previous Researches	57
4.2	The Simplified Model	58
4.2.1	Lagrangian and Free Parameters	58
4.2.2	Perturbativity and Unitarity Conditions	59
4.3	Application to LHC Data	59
4.4	Conclusions	64
III	The 3rd Part: Leptophilic Mediator	67
5	Constraints on Leptophilic Mediator from LHC data	69
5.1	Overview and Previous Researches	69
5.2	The Simplified Model	71
5.3	Application to LHC Data	73
5.4	Conclusions	77
6	Application on Machine Learning Based Classifiers	81
IV	The 4th Part: Summary, Bibliography and Appendix	87
7	Summary	89
	Bibliography	93
A	Appendix	109
A.1	The Cross Section of $N-\chi$ Scattering from Contact Operator	109
A.1.1	Contact Operator	109
A.1.2	Spin-independent Interaction	110
A.1.3	Spin-dependent Interaction	110
A.2	Interaction Rates in Detector	111
A.2.1	General Formula	111
A.2.2	A Simple Case for Maxwellian Halo	112
A.2.3	Relative Movement Between Earth and Sun	113
A.3	Best Cut Efficiencies of LEP Analysis	114
	List of Figures	117
	List of Tables	121

Part I

The 1st Part: Overview

Introduction

1.1 Quantum Field Theory and Standard Model

During the past decades, the Standard Model (SM) of elementary particles has been well established. It contains the basic blocks of our physical world (Fig. 1.1), namely quarks, leptons, gauge bosons and Higgs boson. The last missing block in the SM, the Higgs Boson, was confirmed in 2012 [4, 5]. The SM is built on a fundamental theory called Quantum Field Theory (QFT), which uses the quantized fields that are representations of Lorentz group to construct a quantum theory satisfying Special Relativity. As the upgrade of Classical Field Theory (CFT), fields are the basic concept in QFT, and particles are the excitation of quantized fields. To describe the elementary particles, physicists use Lagrangian density constructed by quantized fields which are representations of Poincaré group and gauge groups. Compared to Hamiltonian or other frameworks, Lagrangian framework has the advantage to ensure the Lorentz invariance of the physical system, which is required by Special Relativity, through the Lorentz invariance of Lagrangian density.

In the Classical Electrodynamics, the electromagnetic interaction is described as 4–vector field A_μ , while electron particle is described as a point–like particle with mass and charge. As the upgrade of the CFT of electromagnetism, the Quantum Electrodynamics (QED) contains a massless vector field (A_μ) and a massive spinor field (ψ) to describe photon and electron respectively. The Lagrangian density of QED is invariant under Poincaré transformation and $U(1)_{\text{EM}}$ transformation, where EM denotes electromagnetism. Besides all the successes of the CFT, some very famous triumphs of QED are worked out, e.g the prediction of anomalous magnetic dipole moment of electron and the Lamb Shift of the energy levels of hydrogen. The most remarkable achievement of QED is extremely high precision. Since QED is one of the most accurate theory describing the elementary particles and their electromagnetic interaction, QFT with gauge fields turns to be very attractive for constructing the physical rules of particle physics.

In the SM of particle physics, the gauge group is extended from $U(1)_{\text{EM}}$ to $SU(3)_C \otimes SU(2)_L \otimes U(1)_Y$, where C , L and Y correspond to *color*, *left–chirality* and *hypercharge*, while the fermion content is extended from electron to leptons ($e, \mu, \tau, \nu_e, \nu_\mu, \nu_\tau$) and quarks (u, d, c, s, t, b). Similar to the $U(1)_{\text{EM}}$ group in QED that describes electromagnetism, the $SU(3)_C$ group depicts *Strong Interaction*. The strong dynamics known as Quantum Chromodynamics (QCD) [6] has confinement effect forbidding free quarks from being detected directly and trapping them in the form of hadrons including baryons and mesons. This feature highly influences what can be detected at the collider or other experimental

facilities. As for $SU(2)_L \otimes U(1)_Y$, they describe weak interaction and electromagnetism together, named as electroweak interaction through the model introduced by Glashow, Weinberg and Salam [7, 8]. In the SM, all the particles are massless and then acquire masses through Higgs Mechanism with Spontaneous Symmetry Breaking (SSB). Under the SSB of the SM, the gauge symmetry¹ breaks spontaneously from $SU(3)_C \otimes SU(2)_L \otimes U(1)_Y$ to $SU(3)_C \otimes U(1)_{EM}$. The unbroken $U(1)_{EM}$ still raises photon, while the unbroken $SU(3)_C$ leads to a new massless gauge boson called gluon labeled with g , and the broken symmetries result in 3 massive gauge bosons W^\pm and Z , whose masses are related to the electroweak couplings and vacuum expectation value (VEV), while fermions acquire masses from the Yukawa terms (interactions between the fermions and the Higgs field) in the Lagrangian. Finally, the Higgs boson itself acquires mass around 125 GeV measured in ATLAS [9] and CMS experiments [10].

In the constructed SM gauge group ($SU(3)_C \otimes SU(2)_L \otimes U(1)_Y \rightarrow SU(3)_C \otimes U(1)_{EM}$), both leptons and quarks may have multi-generations. The N dimensional orthogonal matrix, which reflects the real mixing of N generations of quarks, has $N(N-1)/2$ degrees of freedom (d.o.f), while the N dimensional unitary matrix has N^2 d.o.f. Therefore, there are $N^2 - N(N-1)/2 = N(N+1)/2$ parameters raising from the complexness of the unitary matrix. Moreover, there should be $2N-1$ complex d.o.f that can be absorbed to the relative phase of $2N$ quark fields, as the meaningless overall phase of all quark fields. Finally, the number of the remaining complex phase, which can lead to CP violation, is $N(N+1)/2 - (2N-1) = (N-1)(N-2)/2$. Therefore, in order to include CP-violating terms in the weak interaction, which are implied by experiments, there should be at least 3 generations of quarks. On the other hand, there could be CP-violating terms in the Strong Interaction as well through the so called θ term, $\theta F_{\mu\nu}^a \tilde{F}^{a\mu\nu}$. However, the recent experiments have already placed stringent upper bound of θ with $\theta < 10^{-10}$ [11, 12].

Finally, assuming 3 generations of quarks and leptons and massless neutrinos, we end up with 19 free parameters in the model: 3 lepton masses, 6 quark masses, 3 quark mixing angle, 1 weak CP-violating phase, 3 gauge couplings, the Higgs mass, the VEV, and the QCD vacuum angle (θ). If one needs to discuss massive neutrinos, e.g. in the context of neutrino oscillation experiments [13–15], more Yukawa terms with extra couplings should be added beyond the original 19 free parameters.

The SM has obtained its great triumphs in the past half century. Nevertheless, there are still problems within the model, which has already been implied or proved by experiments. The following list some of the most famous potential issues:

- **Gravitation:** In QFT, on which the SM is built, gravitation may lead to non-renormalizable Lagrangian [16]. The scheme for renormalization and regularization does not work as the case for strong, weak, and electromagnetic interactions. Different approaches have been introduced beyond the SM in the past decades. String theory is one of the most famous solutions to combine the gravitation with other interactions that can be described through gauge groups in the SM.
- **Hierarchy Problem:** Given that the Higgs mass is near 125 GeV, there should be a cancellation for loop diagrams to avoid that the loop contribution for the mass may quickly increase according to the increasing energy level, and hence the Higgs mass is extremely large at high energies. To

¹ Some physicists may claim that the gauge symmetry is not a physical symmetry, but a redundancy, since it does not have a conserved Noether current. Here, in this thesis, the word “symmetry” only means the invariance of Lagrangian under some given transformation, instead of physical symmetry, which corresponds to a conserved current. Therefore, both global and local symmetries are defined as symmetries.

achieve the cancellation, fine tuning should be applied. Supersymmetry (SUSY) [17] is one of the solutions to avoid the fine tuning, since SUSY is a non-renormalization theory whose loop contributions automatically cancel.

- **Hierarchy in Yukawa Couplings:** There is no explanation for the huge difference between the heaviest massive fermion (top quark) and the lightest massive fermion (electron) whose masses arise from the Yukawa terms in the Lagrangian of the SM. This implies their Yukawa couplings for them are quite different. Their difference is around $m_t/m_e \sim 10^6$ [18]. Researchers may be curious about the reason behind the 6 orders of magnitude difference. Unfortunately, SM does not offer any potential explanation.
- **Lepton Universality:** In recent LHCb experiments [19–25], the branching ratio of $K^+ \rightarrow B^+ e^+ e^-$ and $K^+ \rightarrow B^+ \mu^+ \mu^-$ are quite different, where the ratio of branching fractions is measured to be $R_K = 0.846_{-0.054-0.014}^{+0.060+0.016}$ (The first error is statistical uncertainty, while the second is systematic uncertainty). In contrast, the SM predicts this ratio to be exactly unity. The derivation between the SM estimation and the experimental measurement is higher than 2.5 standard derivations, sizable enough to claim an incompleteness of SM. Some new models should be built to solve such a large discrepancy.
- **$g_\mu - 2$:** The QFT succeeds in explaining the anomalous magnetic moment of electron labeled with $g_e - 2$, through the calculation of loop diagrams in QED. The prediction from Dirac equation claims $g_e - 2 = 0$ corresponding to tree level effect in the QFT. The effect from 1-loop diagram adjust the value to $\alpha/2\pi$, where α is fine structure constant. After calculating the loop diagrams to higher order, the predicted value of $g_e - 2$ agrees with the experiments result to the level of 10^{-8} , which is one of the most precise estimation of any physics theory. On the contrary, $g_\mu - 2$ is not perfectly explained by the SM. The difference between the SM prediction and the measured value [26] is

$$\Delta a_\mu = a_\mu^{exp} - a_\mu^{th} = (29.0 \pm 9.0) \times 10^{-10}.$$

The positive value of the difference does not veto the SM prediction, but implies some new particles or hidden sectors which are missing in the SM.

- **Neutrino Masses:** Neutrinos are predicted to be massless in SM, and only have left-handed components. The neutrino oscillation [15] among different flavor, however, proves the tiny but non-zero masses of the left-handed neutrino in SM. Therefore, some new mechanism should be introduced to render the neutrinos massive. A class of models as very attractive solutions utilize see-saw mechanism. In such models, typically 3 new right-handed neutrinos are added to the SM, which are neutral for the SM gauge groups, and have Majorana mass terms [27]. The mass eigenvalue of the right-handed neutrinos should be extremely large to prevent themselves from being detected by recent experiments and observations, and to generate very small masses for left-handed neutrinos. A Majorana fermion is its own anti-particle. Therefore, Majorana fermions described in Feynman diagrams may have 2 opposite particle flow directions. This special property allows the neutrinoless double beta decay to take place, if neutrinos are Majorana fermions. However, there has been no experiment evidence so far related to neutrinoless double beta decay in any experiments.

- **Strong CP Problem:** The symmetries of the SM allows the strong CP-violating term, $F_{\mu\nu}\tilde{F}^{\mu\nu}$, known as the θ term in the QCD sector. This term is not forbidden by any symmetry such as Lorentz and gauge invariance in the SM. In contrast, the experiments have put a strong limit on the value of the θ term. An explanation is required to offer a reason for its smallness. The Peccei–Quinn mechanism [28–31] is one of the potential solutions to this problem through a new spontaneously breaking $U(1)$ symmetry, called Peccei–Quinn Symmetry.
- **Dark Matter:** Dark Matter (DM) issues are the main topic of this thesis, and will be discussed in detail in the rest of this thesis.

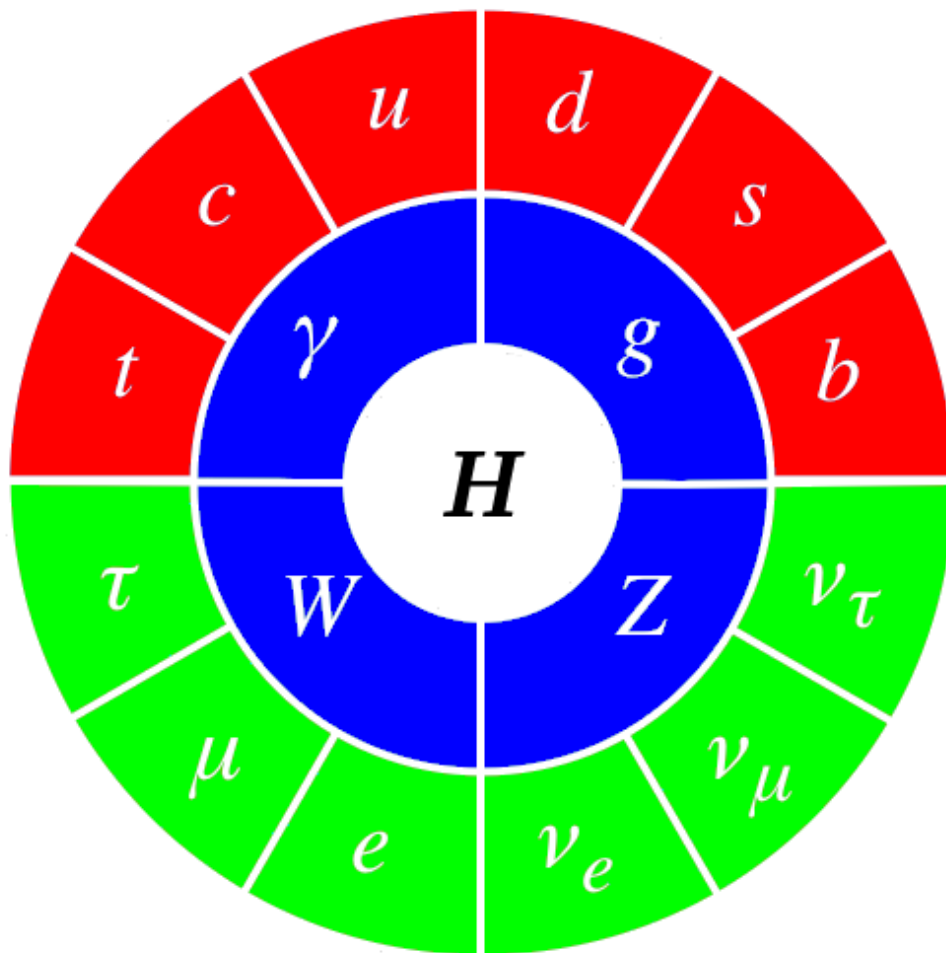


Figure 1.1: Quarks (red), Leptons (green), gauge bosons (blue), and the Higgs boson in Standard Model.

1.2 Dark Matter

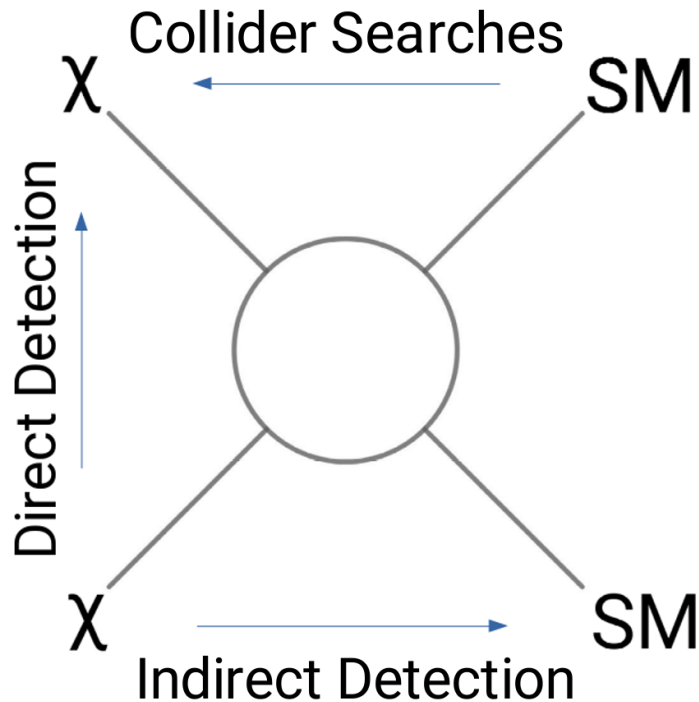


Figure 1.2: The figure summarizes the experiments of DM. The direct detection focuses on the scattering between nuclei (SM particles) and DM particles. The indirect detection focuses on the SM products from DM annihilation. The collider searches focus on the collision of the SM particles that have DM particles in the final states.

The SM has some well known issues, and inspires a series of discoveries beyond the Standard Model (BSM). The lack of adequate candidates of Dark Matter (DM) is one of the most remarkable puzzles. The observations in different macroscopic scales, imply the existence and gravitational effect of DM. Nevertheless, the microscopic interactions of DM remain mysterious, and open a wide and attractive research area. On the theoretical side, the extensions of the SM, String Theory, and Modified Gravity have their different approaches on the topics related to DM. On the experimental side, results from direct detection, indirect detection, relic density, collider searches, etc., can be combined to constrain the parameter space of selected models.

The only known aspect of DM is its gravitational effects in different macroscopic scales. To explore the nature of DM particles, the interactions besides the gravitation need to be studied. Now various experiments have already showed abundant results related to DM. The direct detections of DM is based on the interaction between DM particle and nuclei (corresponding to the up arrow in fig. 1.2). Therefore, the spin-dependent and spin-independent interactions in direct detection experiments always limit the interaction strength between DM and quarks, which form the nuclei as valence quarks or sea quarks. The relic density of DM particles is governed by a Boltzmann equation, which reflects the annihilation and production of the DM particles in the thermal bath of SM particles. When the temperature of the Universe decreases because of its expansion, DM decouples with the SM particles and leaves a constant observable. Therefore, all the interactions between the SM particles and DM

particles are constrained depending on the observation of relic density. The indirect detection of DM focuses on the decay and annihilation products of the DM particles (shown as the right arrow in fig. 1.2), which can be identified from anisotropies of CMB, gamma rays, and cosmic rays. Since the astronomical objects may capture the DM particles because of the gravitational effect, and hence boost the annihilation rate, the measurement of the flux from such astronomical objects are also helpful to study the interactions in DM models, e.g. the neutrinos and muons from the sun.

If DM particles have interactions with the ordinary particles, these interactions should exist at all collider experiments (shown as the left arrow in fig. 1.2), performing as part of the missing energy. Therefore, DM models are also testable in collider searches. The old LEP searches have much lower energy up to only 209 GeV. Their background, however, is relatively clean, and hence the cut efficiency of a given model may be higher than 30%. In contrast, the LHC searches have higher energy up to 13 TeV with complex background events, which leads to low cut efficiency, normally in percentage level or even worse. Some proposed colliders, e.g. ILC or CEPC, share the advantages of e^+e^- colliders and higher energy levels. After applying the same selection rules described in published analyses or designed by ourselves to the result of simulation, a large number of collider searches could be useful materials for discussing the phenomenology of selected DM models. Additionally, the result from collider searches can be easily combined with the non-collider experiments to show the potential of the candidate models, or to close the window for them.

1.3 Simplified Model

Similar to the SM, a series of complete models of DM, e.g. supersymmetric DM models, have been proposed. A complete model is defined as containing all the sectors that respect the gauge symmetry, Poincaré symmetry and other requirements from the QFT, such as the renormalizable condition. The neutralino is one of the candidates of DM in the supersymmetric DM models. The second kind of models are the models built on effective field theory (EFT). For instance, the contact operators between quarks and fermionic DM,

$$\mathcal{L}_{eff} = g_f^V \bar{q} \gamma^\mu q \bar{\chi} \gamma_\mu \chi + g_f^A \bar{q} \gamma^\mu \gamma^5 q \bar{\chi} \gamma_\mu \gamma^5 \chi,$$

are generally used in direct detection experiments. The contact operators describe the interaction between 2 quarks and 2 DM particles, and can be used to predict the DM annihilation in indirect detection or relic density, and DM–nuclei scattering in direct detection. The new terms in the effective Lagrangian are only valid up to some selected energy level, since the Lagrangian itself is non-renormalizable.

The main disadvantage of complete models is that there are too many parameters in the model, and hence the model is not easy to test against experiment data for the whole parameter space or have a series of sectors irrelevant with the problem we concern. For instance, an $U(1)$ extension of SM should have extra degrees of freedom in the Higgs sector to offer the mass to the new gauge boson and DM particles if they are massive. However, this Higgs sector contains not only the Yukawa couplings related to the DM mass and mass of new gauge boson, but also the Higgs mass and extra VEVs. Therefore, the number of parameters quickly increases, when we consider a more complete model. Although the model containing very a large number of parameters always has chance to fit all experiment data, physicists prefer simpler models that are easily testable. A good candidate of DM should be well testable in direct detection, collider searches, and all other experiments, while

the model containing such candidates can be used to explain some special phenomena, e.g. DM annihilation in the early Universe. Obviously, a model with so many free parameters can only be used to fit the special phenomena, but is hard to exclude by experiments. The complete model usually have extra sector irrelevant with the phenomena we concern (mainly DM in this thesis), or extra free parameters that are hard to test. Therefore, the model with a limited number of free parameters, which are relevant to a bunch of complete models, could be more appealing and practical, when we focus on phenomenology research of DM.

On the other hand, if we move from the complete model to the model built on effective field theory, the coupling of every operator may come from quite different sources. For instance, in the contact operator we mentioned $g_f^V \bar{q} \gamma^\mu q \bar{\chi} \gamma_\mu \chi$ derived from a more complete model, the interaction implied by such an operator may be from a vector mediator, a scalar mediator, or some loop structures, while the mass of the mediator and other features in the loop structure are also quite influential for the experimental analysis designed for different signals. The contact operators are equivalent to the case that the inner structure of the 4-point function can be integrated out. In Ref. [32], it is clear to see that the assumption with contact operators strongly weakens the bound compared with more detailed assumptions. Given that most of analyses are designed for special topologies at the collider, only the signature from the new model that can match the selection rules well enough is testable through the published analysis. The contact operators, however, hide the various natures of the inner structure of different models. Therefore, we should focus on the distinguishable signals in the experiments with minimal number of parameters.

As the discussion above, we introduced the simplified models, which are generally considered in this thesis. The simplified models only contain small number of parameters to keep the model more testable by the collider searches than complete models such as SUSY. Moreover, simplified models are supposed to generate distinguishable signals and be tested through various analyses corresponding to different natures of the models. In particular, the vector mediators are the most straightforward assumption of the simplified models, since any gauge extensions of SM may give an extra massive vector mediator after the SSB. In this kind of simplified models, only the mediator mass, DM mass and spin (spinor, scalar, etc.), and couplings with quarks or leptons are free to select. We shall see in the next chapter that not the whole parameter spaces in previous assumption are well testable, even if the assumption itself has already been simple enough. If the simplified models are not testable, all the more complete models related to the same simplified model are hard to test. We, therefore, should perform some optimizations from the experimental side to improve the results for selected models.

1.4 Structure of the Thesis

This thesis is structured as follows.

In Chapter 2, we introduce the background of DM in detail. With the discussion of the previous researches of DM, we should point out the theoretical challenges that our model should explain, and the relevant experimental facts that our model should respect. Moreover, since there has been positive direct detection of DM, we need to argue why DM solution is very attractive in the astrophysical observations.

In Chapter 3 and Chapter 4, we discuss the simplified model containing leptophobic mediators. A leptophobic mediator helps the model avoid the strong constraints from e^+e^- colliders, while it receives constraints from direct DM detection. Unlike the previous research focusing on family-

independent assumption which exactly only shows the phenomenology of light quarks, we investigate the family-dependent case for the phenomenology of heavy quarks. Both LHC and LEP data are applied, while the optimization designed specially for our model is analyzed as well.

In Chapter 5, we turn to the simplified model containing a leptophilic mediator from $U(1)_{L_\mu-L_\tau}$ extension of the SM. We discuss not only DM-related topics from this model, but also other topics BSM, e.g. the anomalous $g_\mu - 2$. Finally, we combine the result from e^+e^- collider, pp collider, and neutrino experiments to study this model in different parameter regions.

In Chapter 6, we summarize the obstacles we meet and the weakness of the recent experiments in previous chapters. Moreover, we discuss the tools from modern computer science that can be used to optimize our results.

In Chapter 7, we summarize all the conclusions in this thesis.

Dark Matter

Dark Matter is the invisible matter in the Universe. The word "invisible" means that it has no electromagnetic interaction, and hence it cannot be detected through visible lights, radios, X-rays, γ -rays, etc. Since there are only 2 well known long distance interactions, gravitation and electromagnetic interaction, the lack of electromagnetic interaction is equivalent with "undetectable" in astronomical observations. Therefore, the evidence of the existence of DM comes from its gravitational effect in galaxies, galaxy clusters, and the universe. Nevertheless, DM may have other interactions in small scale, and can be tested through relevant scenarios. If we assume DM has only gravitation, DM cannot annihilate to any ordinary particles, and hence this may lead to DM overproduction, when we compare the real relic density and the predicted value from the estimation of DM in the early universe. On the contrary, the interaction between DM and ordinary matter can easily produce the observed relic density in wide parameter space. Therefore, the weakly interacting massive particle (WIMP) turns to one of the most attractive DM models. Obviously, if DM has interaction with ordinary matter, there are ways to capture them and to detect them. First, if DM has interactions with nucleon, it may be scattered by nuclei. The direct detection experiments [33–53] are designed for such purpose. Through the zero result so far, the direct detection leaves strong constraints on the models connecting DM to nucleon. Second, the annihilation of DM may generate ordinary particles. Therefore, the annihilation products of DM may be detectable in the cosmic rays, which can be observed by the telescopes on the earth or satellites in the space. This kind of detection is called indirect detection [54–70]. Unlike the direct detection, the indirect detection does not require that the DM has to have interactions with nucleon. Third, the cue of the annihilation of DM is not only from the cosmic rays, but also from the relic density. The annihilation rate may change the equilibrium of ordinary matter in the early universe during special periods, like nucleosynthesis, and then change the current relic density of DM. Therefore, the relic density may offer a lower limit of annihilation rate for DM models. Finally, DM that has interactions with ordinary matters can be generated in the collider. The relative old collider searches with missing energy [71–80] have already been very powerful to test DM effective models or simplified models. In the following chapter, we will apply a series of more recent LHC analyses to discuss DM related model with different final states. Although the final state DM in collider is just missing energy, which is not distinguishable from neutrinos inside collider, the massive DM and other new particles beyond standard model could strongly change the topologies of the final state objects. Therefore, through the careful event simulation and selection, the result from observed data can test the relevant DM model. The following sections will list the previous results from other researchers for

evidence, direct detection, indirect detection, relic density, and collider searches respectively.

2.1 Evidence

2.1.1 Rotation Curves of Spiral Galaxies

The spiral galaxies are classified by their arm–structure. The arm–structure is the regions of stars that extend from the center (upper figure in Fig. 2.4 from the official website of NASA ¹). In the center of the spiral galaxies, large mass centralizes here and forms a region called bulge. The velocity in rotation curves of spiral galaxies should depend on the radius through the simple Newton gravitation. If we assume the luminous mass of the galaxy is situated in the bulge of the galaxy, the velocity of rotation agrees the following rule

$$\frac{mv^2}{r} = \frac{GMm}{r^2} \Rightarrow v = \left(\frac{GM}{r}\right)^{1/2} \Rightarrow v \propto r^{-1/2}. \quad (2.1)$$

The assumption of mass distributing a uniform disk gives similar result. In the astronomical observation, however, the velocity is roughly a constant for the large radius, when it is first time measured by Vera Rubin [81]. Therefore, if our assumption works, the central mass distribution should be proportional to radius, i.e. $M \propto r$. This implies the real mass distribution is quite different with our assumption. A more detailed example is shown in the lower part of Fig. 2.4. The observed and expected curves in this example, are similar with the observed and expected velocity to radius relations in our previous discussion respectively. The obvious difference is shown clearly in the figure. Other researches [82, 83] claim the similar conclusion that the mass distribution may be quite different with the observation. This is a hint to claim that the luminous mass may be not the total mass in galaxies. Additionally, the luminous perhaps is not the dominant mass in this kind of galaxies as well. Nevertheless, there are still other explanation of the unexpected rotation curve, besides the existence of DM. The modified gravitation like *Modified Newton Dynamics* is also helpful to solve the puzzle [84]. Therefore, the rotation curve is only a hint of the DM assumption, not the strong proof to claim the existence of DM.

2.1.2 Galaxy Clusters

A galaxy cluster may contain 100 – 1000 galaxies, and its mass could be $10^{14} - 10^{15} M_{\odot}$, where M_{\odot} is the mass of sun. The galaxy cluster is the largest gravitationally bound structure in the universe, and its diameter is typically 2 – 10 Mpc (10^{23} m). Besides 100 – 1000 galaxies, the galaxy cluster has X–ray emitting gas inside, which is normally much more massive. In the optical observation, only galaxies are visible, while we can observe gas through the X–ray. Therefore, the total mass estimated from the gravitation effect can be compared with the luminous mass through the direct observation. The difference between luminous mass and total mass again implies the existence of DM.

Bullet Cluster

Bullet cluster (1E 0657-558) [86, 87] contains galaxies, gas, and perhaps invisible mass. The existence of invisible mass should be very important proof of DM. Bullet cluster is named as bullet,

¹ <https://www.nasa.gov/feature/goddard/2017/messier-101-the-pinwheel-galaxy>

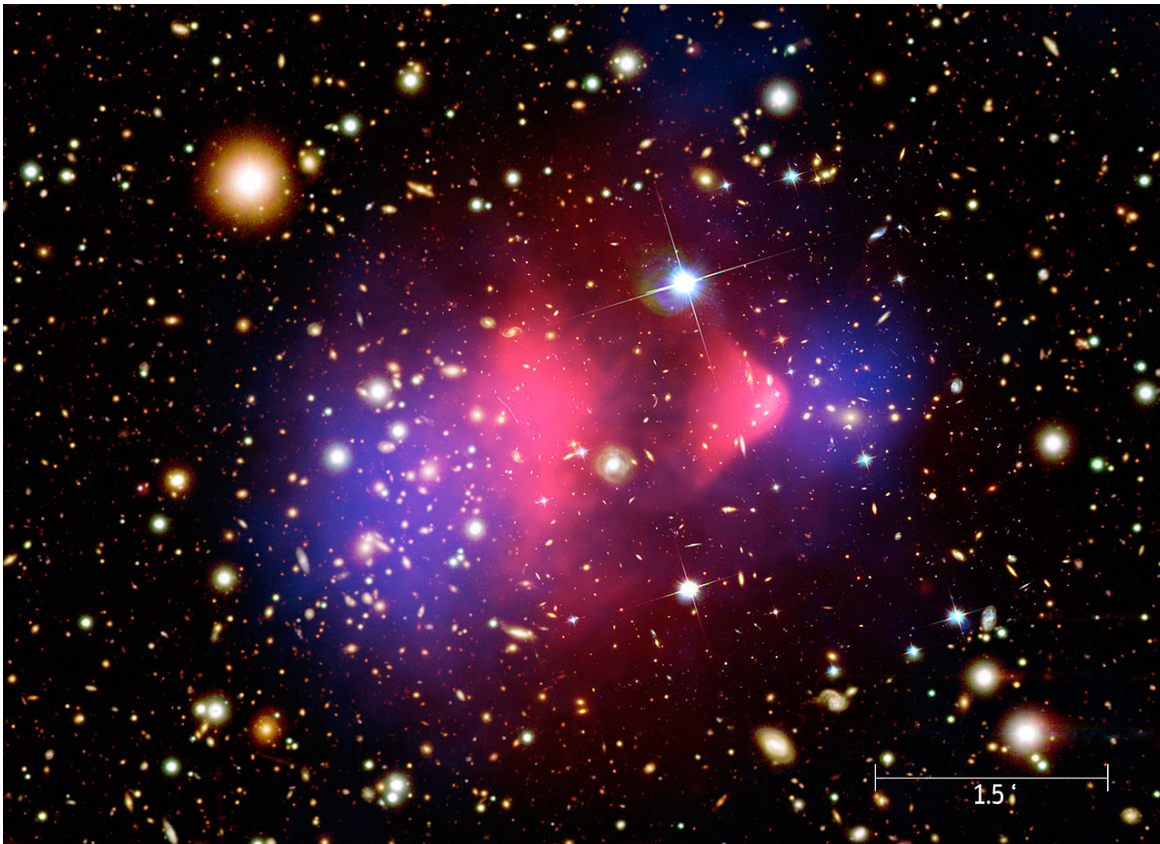


Figure 2.1: The visible lights with different colors show galaxies. The pink area is the X-ray photo. The blue area is the mass distribution from gravitational lensing. If we assume the luminous mass approximately agrees the baryonic matter shown by the X-ray photo, the luminous mass is obviously distinct from the total mass.

since it consist 2 collided components of galaxies with hot gas. The optical observation can show 2 clusters of galaxies, while the emission of X-ray can show the distribution of gas, which represents the main component of baryonic matter that forms the dominant visible mass in bullet cluster. If there is no large amount of DM, the luminous mass observed through X-ray should approximately equal to the total mass measured by gravitational lensing. The observed result is shown in figure 2.1. The figure is from the official website of Chandra X-ray Observatory from NASA². In the figure, it is clear to see that the luminous mass forms 2 separated parts like we described above. Nevertheless, the total mass indeed distributes differently with the luminous mass. Unlike the rotation curve, the difference between the luminous mass and total mass is hard to explain by modified Newton dynamics, since the total mass distribution is measured directly by gravitational lensing. Therefore, the measurement of bullet cluster is more important clue to ensure the existence of DM.

² <https://chandra.harvard.edu/photo/2006/1e0657> or <https://apod.nasa.gov/apod/ap060824.html>

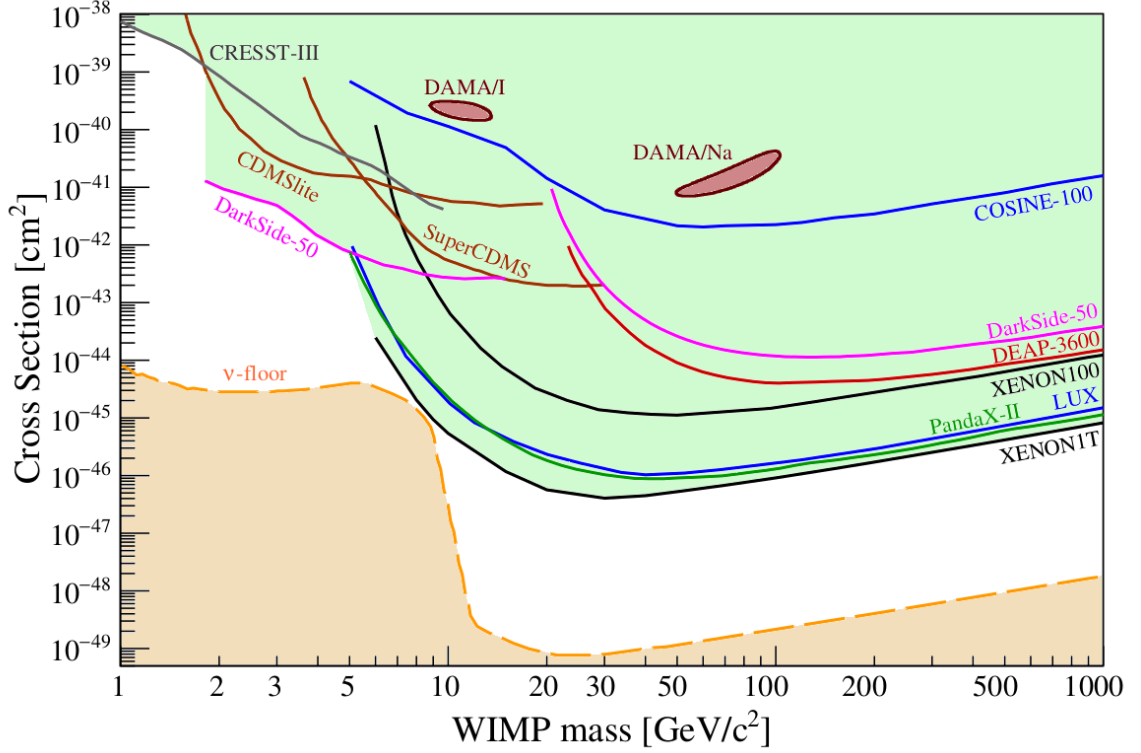


Figure 2.2: The figure is the bound of spin-independent cross sections. The lines above are the exclusion plot for 90% CL, while the dashed line is the neutrino floor from the measurement of the background in coherent $N\nu$ scattering. The bound for spin-independent interaction is on the sum of neutron and proton, e.g. C_s in A.1.

Coma Cluster

Coma Cluster (Abell 1656) is very large galaxy cluster containing over 1000 galaxies. The cluster is 99 Mpc ($\approx 3 \times 10^{24}$ m) away from earth. In 1933, Fritz Zwicky pointed that the Coma cluster moved too fast to keep the visible matter together through the gravitational effect [88]. His estimation use *Virial Theorem*, which describe the relation between the virial and the total kinetic energy,

$$\langle T \rangle = -\frac{1}{2} \sum_{k=1}^N \langle \vec{F}_k \cdot \vec{r}_k \rangle. \quad (2.2)$$

If we assume the Coma Cluster is in statistical equilibrium and the dominant force inside the cluster is gravitation. The specialized virial theorem for this system should be in the following form

$$\frac{1}{2} M \langle v^2 \rangle = \frac{1}{2} \frac{GM^2}{2} \langle r^{-1} \rangle \Rightarrow M = \frac{2 \langle v^2 \rangle}{G \langle r^{-1} \rangle}. \quad (2.3)$$

Therefore, we can calculate out the predicted mass of the galaxy cluster, which is $\approx 4.5 \times 10^{10} M_{\odot}$. The predicted luminous mass, however, is $\approx 8.5 \times 10^7 M_{\odot}$, which is estimated from the measured luminosity ($L \approx 8.5 \times 10^7 L_{\odot}$) of the cluster, since we can approximately assume that the mass is proportional to luminosity in this special case. The difference between the luminous mass and the total mass is around 2 orders of magnitude, and obviously implies the existence of large amount of invisible matter, i.e. Dark Matter.

2.1.3 Cosmic Microwave Background (CMB)

CMB is the electromagnetic radiation that filling the whole universe and known as the remnant from the early universe. It is the oldest electromagnetic radiation that can be observed by scientists in recent study, and can be traced back to the epoch of recombination. In early research through traditional optical telescope, the background of the universe is empty. Nevertheless, the sensitive enough radio telescope finally observed the non-empty background filling by electromagnetic radiations that have already decoupled from the matter, like electrons and baryons. In the early observation, CMB is almost isotropic, since the precision is not sufficient, and its temperature is approximately 2.7 K according to COBE satellite [89]. Nevertheless, in the recent map of CMB, the anisotropy is observed. The observation of the temperature of CMB depending on different directions is shown in the upper frame of figure 2.5. The different colors in the map clearly show the anisotropy of CMB. The coldest point and the hottest point in the figure takes the difference around $O(10^{-5})$ K. CMB has already been observed by different telescopes with increased precision, and the anisotropy always exist, which requires an explanation from scientist.

The distribution of DM in early universe is helpful to explain the anisotropy of CMB. To parametrize the anisotropy, we use the spherical harmonics

$$\frac{\delta T}{T} = \sum_{l=2}^{\infty} \sum_{m=-l}^{m=l} a_{lm} Y_{l,m}(\theta, \phi), \quad (2.4)$$

where a_{lm} are the coefficients. We connect the coefficients to the power spectrum, defined as $\frac{l(l+1)}{2\pi} C_l$, through $C_l = \langle |a_{lm}|^2 \rangle$. The Λ -CDM model fits the observation very good in figure 2.5 [90]. In the name Λ -CDM, Λ means the existence of cosmological constant, offering Dark Energy, which dominates the total energy of the universe, while CDM means *Cold Dark Matter*. Therefore, in Λ -CDM model, the universe contain Dark Energy, Dark Matter, and Ordinary Matter. According to the recent observation [90], the percentages of various types of energy in Λ -CDM model are 68.3% Dark Energy, 26.8% Dark Matter, and 4.9% Ordinary Matter. The ratio of different energy types and other parameters in Λ -CDM model can be fitted together through the observed data. The Λ -CDM model fitting to CMB data, not only shows the existence of DM, but also claims that the amount of DM is much larger than the Ordinary Matter.

2.2 Relic Density

The evidence of DM are all from gravitational effects in large scale, e.g. galaxy, galaxy cluster, and the universe. Given that the lack of electromagnetic interaction of DM particles, gravitation is the only long distance force related to DM. However, even if gravitation and electromagnetic interaction

are the only forces we normally considered in the recent macroscopic world, DM may have other macroscopic effect, if we assume DM has some extra microscopic interactions with ordinary matter. Although in previous section we consider DM is cold now in universe scale, there are still other models considering hot dark matter in smaller scales. In contrast, whatever the temperature of DM recently is, DM has to be quite hot in early universe like any other matters. The early universe was a hot plasma, where all the particles interacted with each other and kept a thermal equilibrium. According to the expansion of the universe, the thermal bath gradually cooled down, and a series of particles decoupled from the thermal bath. DM therefore was similar with ordinary matter in the early universe. Since DM influenced the thermal equilibrium in the early universe, it changed the matter contents in the early universe even in macroscopic scale. Moreover, the decoupled DM remains until today, leaving an observables for us the test the models built for DM.

Given the universe expansion, DM in the thermal bath should obey the Boltzmann equation

$$\frac{dn}{dt} + 3Hn + (n^2 - n_{eq}^2) \langle \sigma v \rangle = 0, \quad (2.5)$$

where n is the number density, n_{eq} is the number density of the equilibrium, H is the Hubble Constant, σ is the annihilation cross section, and v is the relative velocity of the DM particle that decay. Besides using $\langle \sigma v \rangle$ directly, we can use the annihilation rate, $\Gamma_A \equiv n \langle \sigma v \rangle$, to express the Boltzmann equation instead. If the temperature of the thermal bath is lower than the mass of DM, where $T < m_{DM}$, the generation of DM from ordinary matter ends, while the annihilation of DM continues. After the generation of DM ended in our universe, the annihilation of DM would end, when the expansion was larger than the annihilation rate, where $H > \Gamma_A$. This procedure is called ‘‘Freeze out’’, and connects the recent DM abundance in macroscopic scale, to the annihilation rate in microscopic scale. The ‘‘Freeze out’’ is shown in figure 2.6 from the book *The Early Universe* [92]. It shows the increasing σv should lower the remaining number density.

To connect the model to the observation, we need to use a observable named as relic density, or relic abundance of DM. The relic abundance of DM is defined as

$$\Omega_{DM} h^2 = \frac{\rho_{DM}}{\rho_c} h^2 = \frac{m_{DM} n_{DM} h^2}{\rho_c}, \quad (2.6)$$

where $\rho_c \equiv 3H_0^2/8\pi G \approx 2.775 \times 10^{11} h^2 M_\odot / Mpc^3$ is the critical density of the universe. According to recent observation, $\Omega_{DM} h^2 \approx 0.12$ [93]. Therefore, it sets limitations of Γ_A , when the mass of DM (m_{DM}) is set. In other words, to avoid the predicted $\Omega_{DM} h^2$ is too large, the annihilation rate should be sizable enough. The DM overproduction issue will be discussed in the following chapters for various models accordingly.

2.3 Direct Detection

Direct detection of DM focuses on the scattering between moving DM and target nuclei. The local DM density on the earth is predicted to be $\sim 0.4 \text{ GeV/cm}^3$, and the local speed of DM is estimated to be 220000 m/s [18]. The recent experiments of direct detection include CRESST [36, 40, 41], CDMSlite [35, 42], superCDMS [34, 43], Panda X-II [35, 44], and LUX [45, 94]. If we assume DM is WIMP, the first 3 experiments only sensitive enough to argue the light DM, where $m_{DM} < 5$

GeV, while the last 2 is sensitive enough to bound the larger mass region. There are also proposed or running detection, e.g. LZ [33, 45, 46, 48, 49] and XENON1T [33, 47, 50–52]. The recent run of XENON1T was from October 2016 to February 2018 [53]. There will be more data analysis released officially. Before comparing to the experimental data, we should calculate the theoretical expression first.

To calculate the cross section from scattering amplitude, we use the general formula

$$\frac{d\sigma}{dq^2} = \frac{1}{\pi v^2} \sum_i C_i F_i^2(q^2) \quad (2.7)$$

where C_i depends on square of the scattering amplitude, F^2 is the form factor, and $q = p - p'$ is momentum transfer during scattering. If the target particle can be treated as point-like, $F^2 = 1$. On the contrary, for a real target particle, the form factor should be carefully modeled. Next step is just to find different C_i for spin-dependent and spin-independent scattering respectively. To give an example, we calculate the cross section from effective Lagrangian for Majorana DM, which does not have vector couplings, i.e. $\bar{\chi}\gamma^\mu\chi = 0$, in appendix A.1 at the end of the thesis.

After calculating σ of the $N - \chi$ interaction, we can further derive the interaction rate. The interaction rate is the relevant quantity for direct search experiments, and is usually measured in events/(kg * day). We show the detailed definitions and derivations in appendix A.2.

After deriving the theoretical estimation, we can compare it with the experimental data to reach the bound for certain model. The experimental result is shown in Fig. 2.2 for spin-independent interaction and Fig. 2.3 for spin-dependent interaction [95]. The result is the upper limit of the interaction cross section and can be applied to selected models. In Fig. 2.2, there are only one figure showing the upper limit of the total cross section. In formula A.8, the contribution from proton and neutron is not distinguishable. Therefore, the upper limit is for the effect summing from both neutrons and protons. On the other hand, in Fig. 2.3, there are 2 figures showing the upper limit of the spin-dependent cross sections for χ -proton and χ -neutron respectively. In formula A.16, the contribution from proton and neutron depends on the vector sum of proton and neutron respectively. Due to the spin cancellation of the nucleon pairs, C_A is mainly from the unpaired proton or neutron. Therefore, the bound is derived from the theoretical estimation for pure proton case or pure neutron case respectively [96]. According to the theoretical derivation above, we can choose different DM models and distributions. The calculation in appendix A.1–A.2 shows examples with contact operator, and the calculating procedure can be repeated for C_i in other models and $f(v)$ in other distributions. In the following chapter, we mainly focus on the interactions from a vector mediator, instead of the contact operator.

2.4 Indirect Detection

The indirect detection use the decay product of DM. Although the recent relic density is not dense enough to annihilate to ordinary matter because of the expansion of the universe in large scale, there are still special regions where DM is dense enough. The region can be formed through massive object in small scale, e.g. the Sun near earth, to generate the annihilation products of DM. There are 3 kinds of indirect detection experiments using distinct sources, γ -ray, antimatter, and neutrinos.

First, the γ -ray observation focus on the high-density objects that can accumulate DM, e.g. Galactic

Center. For instance, Fermi–LAT³ from NASA is one of the most important instruments. It is one part of Fermi Gamma Ray Space Detector, besides the Gamma Ray Bursts Monitor (GBM). The results from Fermi–LAT help us constrain $\langle\sigma v\rangle$ from the various channels of SM products, e.g. e^+e^- , $\mu^+\mu^-$, etc. The main obstacle to achieve results is the analysis of the various sources in the background, i.e. distinguishing the DM–original source from other sources.

Second, the antimatter observations commonly detect positron and antiproton fluxes. The antiproton is measured by Fermi–LAT [59, 63–66] and AMS–02 [62], while the positron is detected by AMS [54], PAMELA [55], and AMS–02. So far, the positron measurements offer better constraints on DM related model.

Finally, the neutrino observations from IceCube [60, 67, 68] and ANTARES [61, 69, 70], help us bound the spin–dependent interactions with nuclei, which can be directly compared to the result from direct detection.

2.5 Collider Searches

The collider searches is the main topic of this thesis. In the following chapters in the Second Part and Third Part of this thesis we will consider the DM particle has interactions with various SM particles, and hence can be probed in collider searches. Since DM is only missing energy in the colliders, and we need to detect visible particles as signatures, we try to apply a large number of analyses containing the leptonic final states and hadronic final states related to our selected models from LHC or LEP data. Those detailed discussion shows not only the sensitivity of experimental data for selected models, but also the standard procedure to discuss a model related to DM through collider searches. In the previous research [32], the most general simplified model with all renormalizable terms are considered. Finally, the terms related leptons or quarks are the most testable sectors, since they reflect different final state signatures directly. Therefore, in the following chapters, the leptophobic and leptophilic mediator, which couples to quarks and leptons respectively, are analysed.

For leptophobic mediator, the assumption with universal quark couplings have already been studied [32]. Since the valence quark content of proton contains u and d quark, while the largest contribution in direct detection is from interactions with u and d quark as well, the couplings with u and d quark dominate the phenomena in general. Therefore the family–independent assumption that are commonly considered in previous researches actually shows the phenomenology of light quark couplings. On the contrary, in this thesis, we focus on the case that the mediator does not couples to u and d quarks to discuss the heavy quark phenomenology. Additionally, the previous studies using LHC data only analyse the on–shell mediator that can decay to quarks and DM particle. In our LEP based analysis, however, we analyze off–shell mediator.

For leptophilic mediator, the couplings with electron are highly constrained by the data from e^+e^- colliders, since the s–channel Feynman Diagram has very large contribution. We therefore focus on the mediator couples to μ and τ from an anomaly free $U(1)_{L_\mu-L_\tau}$ extension of SM.

We discuss the previous researches of leptophobic and leptophilic mediators and our assumption of parameters with more details in the “Overview and Previous researches” sections and “The Simplified Model” sections of Chapter 3–5 respectively.

A series of simulation tools are used in the following chapters as the common framework for collider phenomenology. First, we use FeynRules [97] to express our models into programing code. Second,

³ <https://glast.sites.stanford.edu>

we use MadGraph [98] to simulate the collider event in the parton level. Third, we use PYTHIA [99] to hadronize the parton level events. Fourth, we use DELPHES [100] to apply the parameterization based fast detector simulation to consider the detector effect for ATLAS and CMS experiments. Finally, we use CheckMATE [101] to visit the final state objects after detector simulation and calculate the advanced kinetic variables defined and used in collider researches. The details of the simulation tools will be discussed in the following chapters.

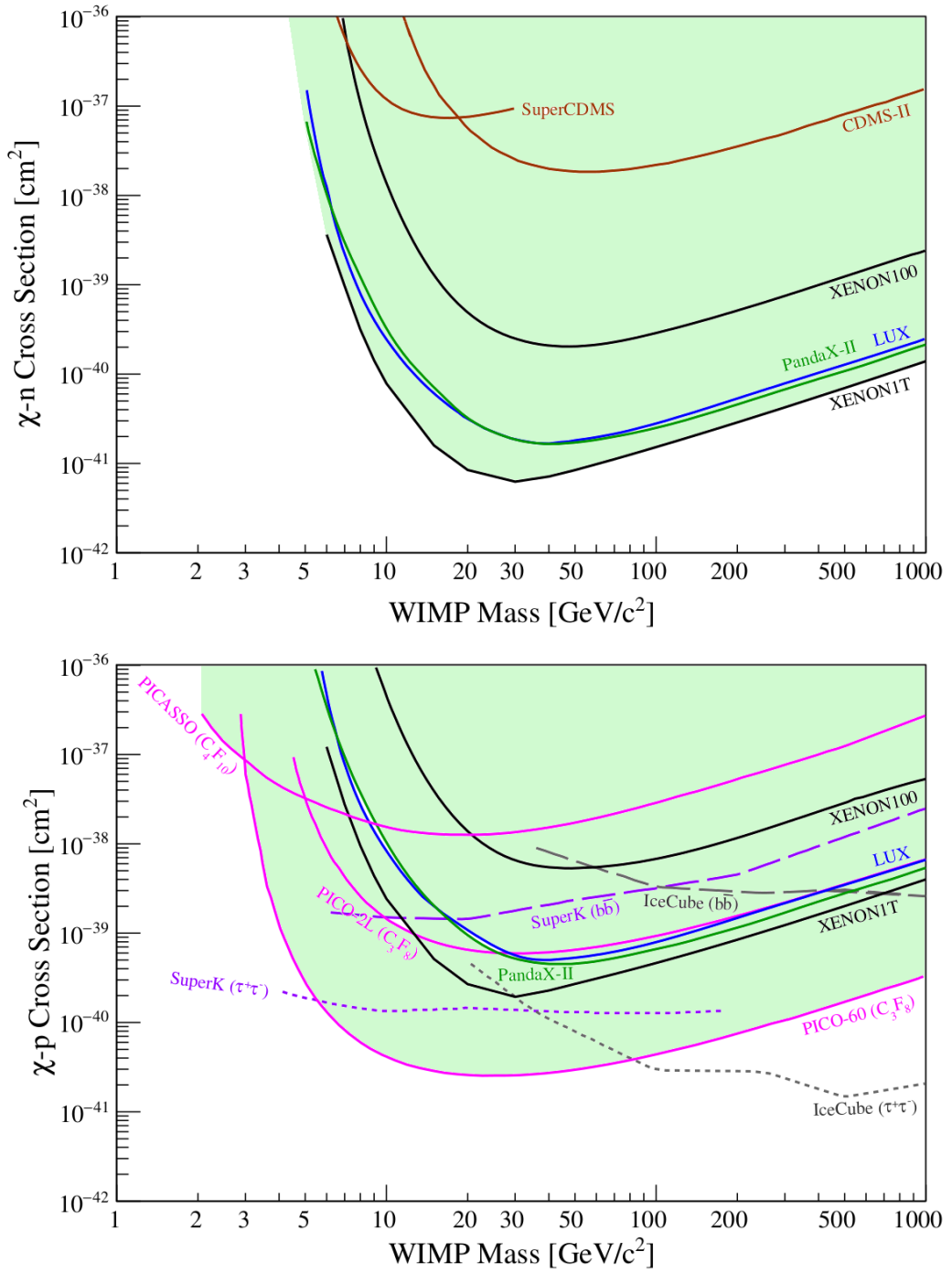


Figure 2.3: The figure is the bound of spin-dependent cross sections. The upper figure is for neutron, while the lower figure is for proton.

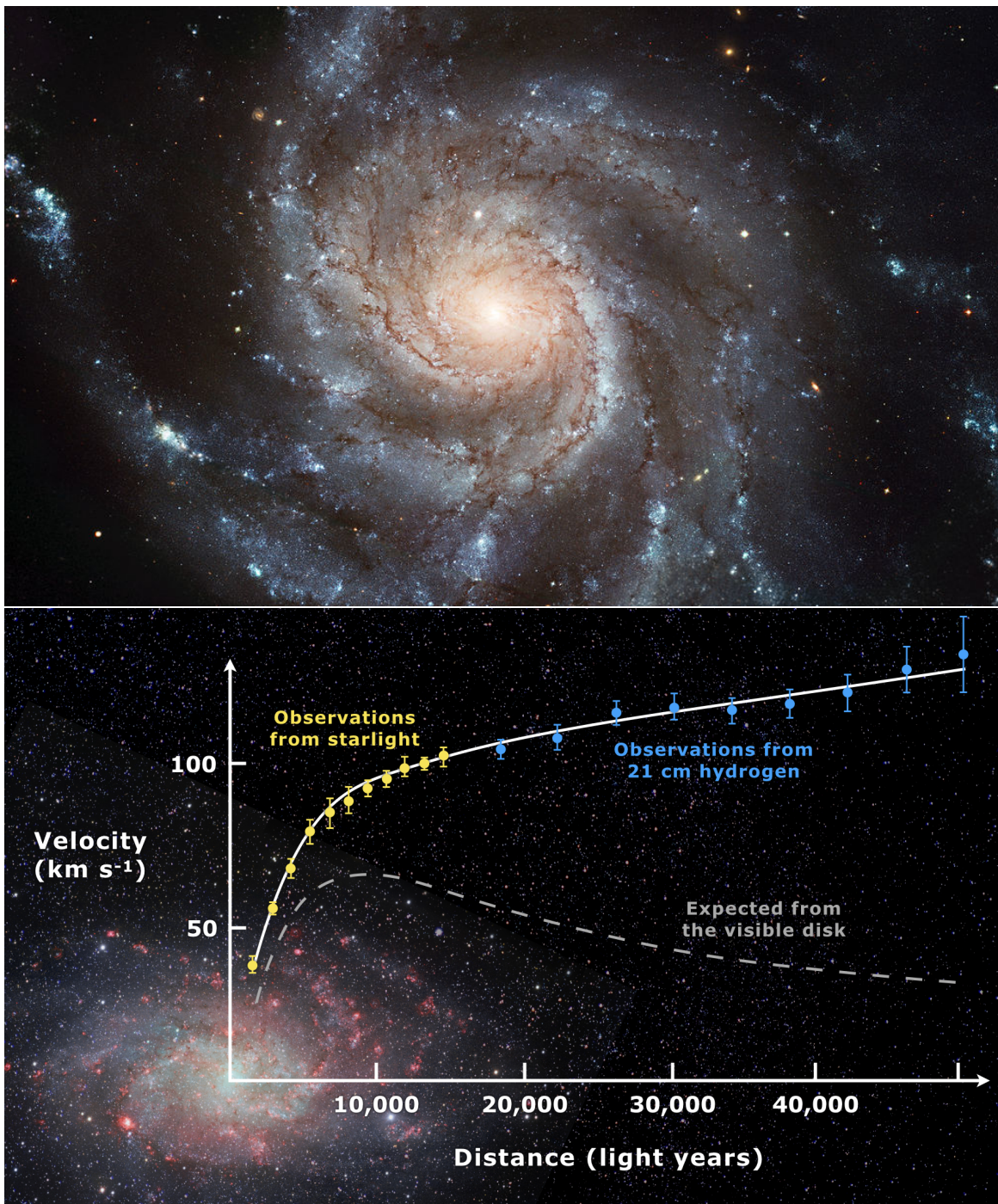


Figure 2.4: Upper figure is Messier 101, an example of spiral galaxy. It is clear to see the bulge in the center, and the spiral arm extended from the center. Lower figure is rotation curve of Messier 33 [85]. The expected curve and the observed curve are obviously distinct, especially in the large distance area.

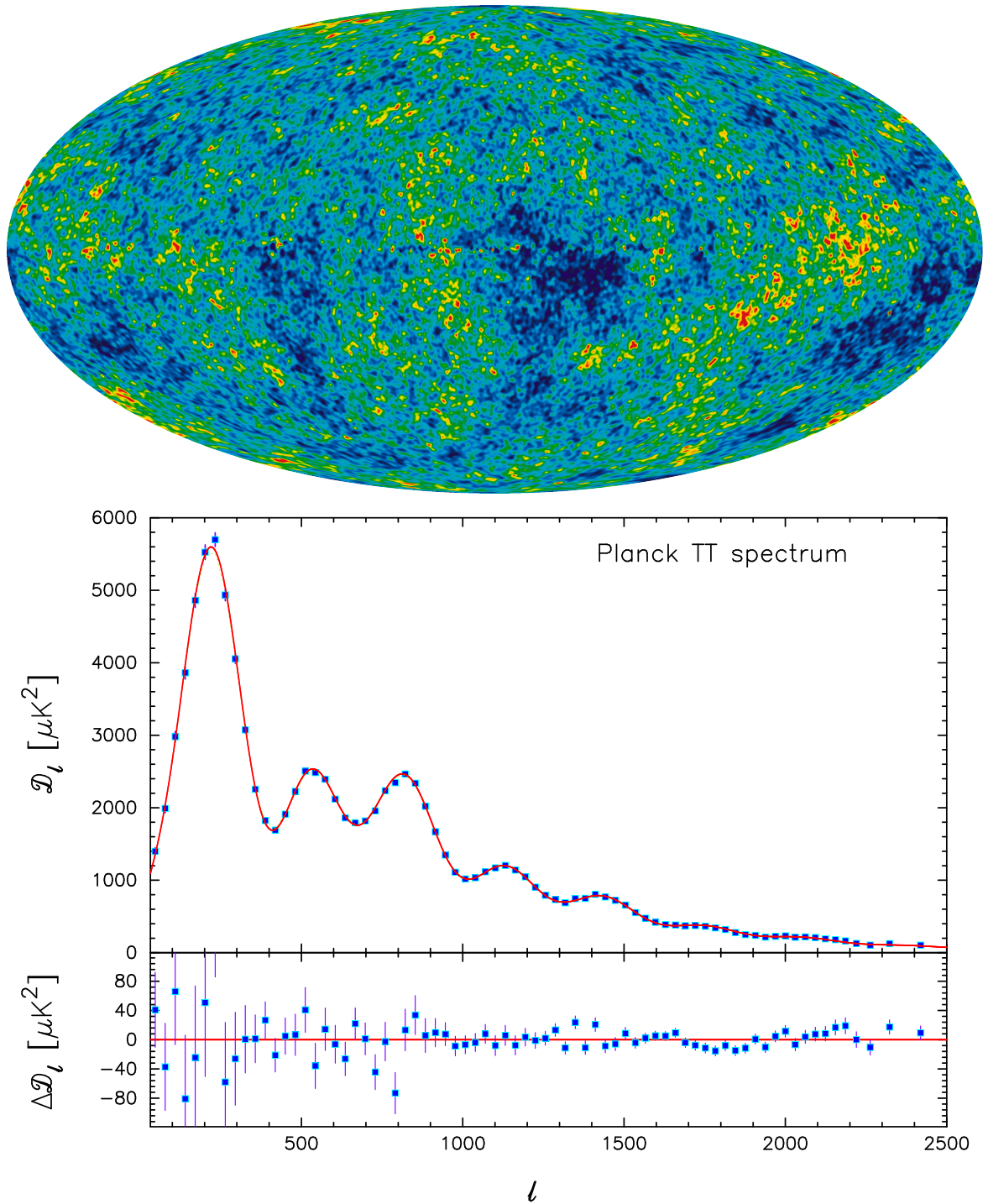


Figure 2.5: The result in the first figure is based on the data collected by Wilkinson Microwave Anisotropy Probe (WMAP) in 9 years [91]. More red means hotter, while more blue means colder in the figure. The second figure is the comparison between the best theoretical estimation from Λ -CDM model and the recent observation [90]. In the upper part of the second figure, the definition of y -axis is $D_l = l(l + 1)C_l/2\pi$, while x -axis is multipole l . The blue points are the maximum-likelihood estimates from the observed data by Planck satellite. The red line is the best fit from Λ -CDM model. Additionally, the lower part of the second figure shows the residuals.

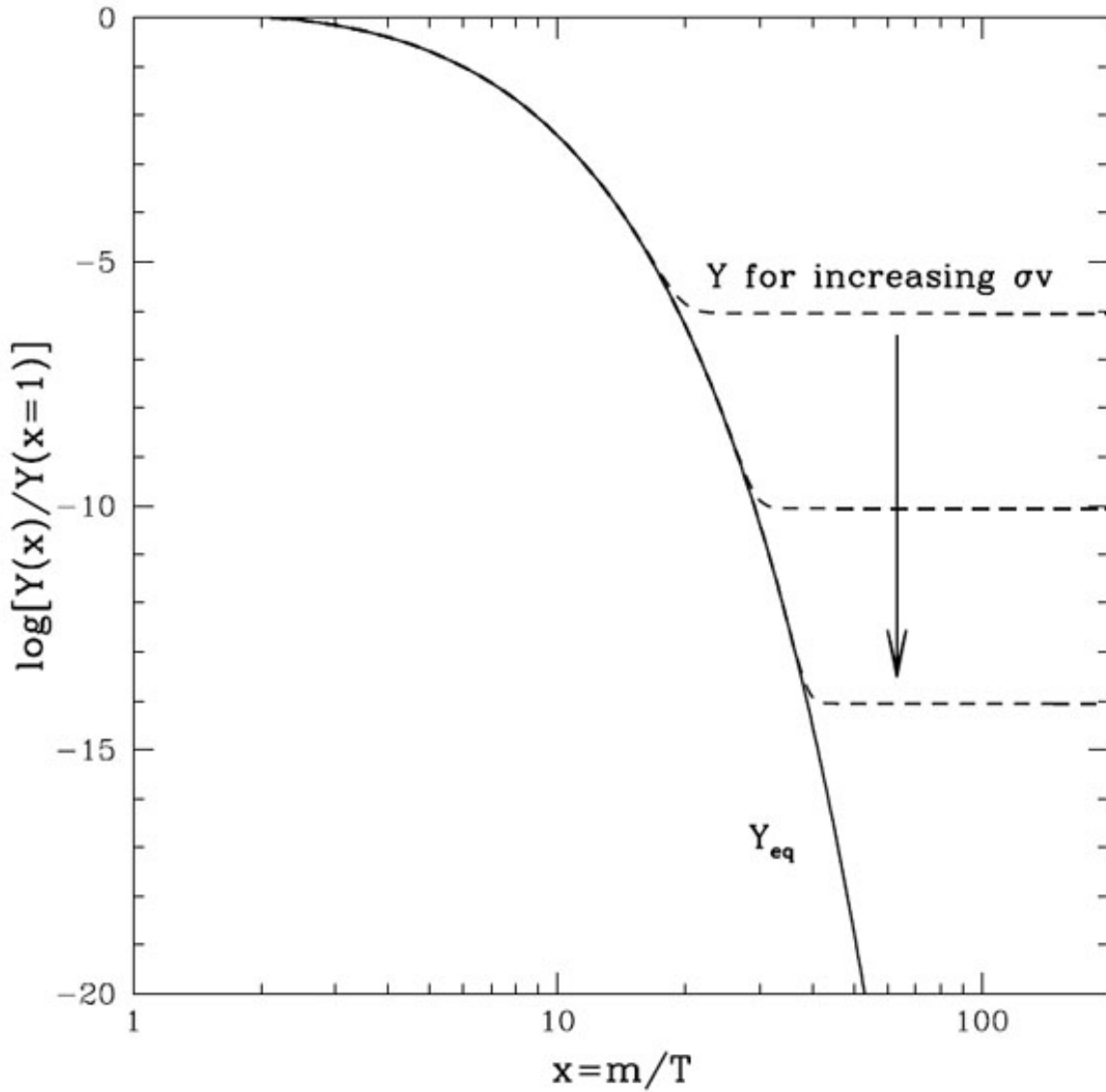


Figure 2.6: The figure shows the “Freeze out” procedure of DM. It does not use time (t) and number density (n) directly. In the figure, $x \equiv m/T$, where m is the mass of DM and T is the temperature, and $Y \equiv n/s$, where n is the number density of DM and s is the entropy. Along with the increasing time, the temperature should decrease, meaning larger x . Additionally, n and s decrease simultaneously, as the expansion of the universe. Therefore, it is better to use Y to show the constant tail.

Part II

The 2nd Part: Leptophobic Mediator

Constraints on Leptonphobic Mediator from LEP data

3.1 Overview and Previous Researches

The Standard Model (SM) of particle physics lacks an adequate candidate for dark matter [102]. Particle physics explanations of dark matter therefore typically include a “dark sector” containing (at least) one stable dark matter candidate (called DSP for Dark Sector Particle in this chapter), and at least one mediator coupling the DSP to SM particles. In principle this mediator could be the well-known Z or 125 GeV Higgs boson, but these “portal” models are by now very tightly constrained [103–105]. Here we are interested in models where the mediator is not part of the SM. Frequently it is a massive scalar or vector boson. Therefore, a simplified model approach [80, 106, 107] allows to constrain many UV complete extensions of the SM. Simplified models usually have a relatively small number of free parameters, allowing exhaustive scans of the parameter space. Models designed to describe the scattering of DSPs on ordinary matter, as in “direct search” experiments, have to specify the couplings of the mediator(s) to hadrons and to the DSP. This suffices to fix the rate of monojet (and similar) events at the LHC. Since no excess of such events has been found, LHC data have given strong constraints for mediator masses below about 1 TeV that can decay invisibly, e.g. into a pair of dark matter particles [108, 109]. Moreover, mediator masses roughly between 1 and 2.5 TeV are also constrained by searches for di-jet final states [110, 111]. Very recently this range has been extended downward by using special search strategies [112]; preliminary results using events with a hard third jet recoiling against a “fat jet” allowed CMS to extend the search range down to 50 GeV [113], for coupling strength to (light) quarks $\gtrsim 0.2$.¹

It should be noted that more complete models are often subject to additional constraints. For example, Z' models based on extending the SM gauge group with an additional $U(1)$ factor were investigated in [114–119], and supersymmetric models in [120–122]. However, many or most of these constraints are not directly related to the dark matter problem. In our purpose, we want the constraints that directly relate to dark sectors. Therefore, we assume simplified model with the least parameters related to dark sectors instead of more complete model.

Although the Large Electron Positron collider (LEP) at CERN ceased operations nearly twenty years ago, and only covered center-of-mass (cms) energies up to 209 GeV, the cleaner environment

¹ This analysis also found a slight excess of events corresponding to a mediator mass of about 115 GeV.

and the distinct energy range still offer some advantages for certain regions of parameter space. In this chapter we focus on a simplified model with a vector mediator R coupling to the DSP and quarks. We use the framework of ref.[32], which starts from the very general assumption that the new mediator couples to all different kinds of SM particles, including gauge bosons, leptons and quarks. It uses LHC data (from run 1) in order to derive stringent upper bounds on many of these couplings. These constraints are quite strong if on-shell decays of the mediator to DSPs are possible, or if the mediator has sizable couplings to leptons. We saw above that (in some cases still preliminary) constraints from LHC searches for purely hadronic final states have become quite strong, if $m_R > 50$ GeV. However, the published constraints apply to couplings to first generation quarks, which are strongly constrained by direct dark matter searches. The annihilation cross section of the DSP χ into hadronic final states can therefore still be sufficiently large for χ to be a good thermal WIMP (Weakly Interacting Massive Particle) candidate [92] in standard cosmology. In this chapter we also focus on the $\bar{\chi}\chi R$ and $\bar{q}qR$ couplings. Note that together with the masses m_R and m_χ these are the key parameters determining both the direct WIMP detection rate and (if the other couplings are small) the relic density.

There are also purely theoretical constraints on the model. Ref.[32] derived an upper bound on the couplings from the requirement that perturbation theory can be applied, since we do not know how to constrain these couplings otherwise. Moreover, as pointed out in ref.[123], if R has non-vanishing axial vector couplings to χ , unitarity imposes an upper bound on the ratio of DSP and mediator masses. We apply the same perturbativity and unitarity conditions in the part of parameter space that could have been probed by LEP experiments.

LHC data only probe configurations where the mediator is essentially on-shell. In contrast, in this chapter, which focuses on a light mediator, we consider cases where the DSP pair can only be generated through off-shell processes. We notice an enhancement of the cross section if the mediator has an axial vector coupling to b -quarks and $m_R < m_b$ because the longitudinal part of the mediator contributes a term $\propto m_b^2/m_R^2$ to the four-jet cross section. Similarly, in the presence of an axial vector coupling to the DSP the di-jet plus missing energy cross section may increase with increasing m_χ , contrary to naive expectations. However, the unitarity constraints imply that these terms cannot be arbitrarily large.

This chapter is organized as follows. In section 3.2 the Lagrangian of the simplified model is introduced, and bounds on the relevant couplings from theoretical considerations and non-collider experiments are discussed. In section 3.3 we recast searches for di-jet plus missing energy and 4-jet final states performed by the ALEPH collaboration [124, 125]. We discuss the bounds resulting from these published searches and the cut efficiencies when applied to our model. In section 3.4 we introduce a set of specially designed cuts for the di-jet plus missing energy signature that have much higher efficiency for our signal than the published searches. Although we do not include the detector simulation in the test of the background suppression, the result still shows the potential of the LEP data to improve on the bounds derived in section 3.3. Finally, section 3.5 is devoted to a summary and some conclusions.

3.2 The Simplified Model

In this section we first describe the Lagrangian of the simplified model we consider. We then discuss limits on the model parameters that follow if the DSP is assumed to be a thermal WIMP, which is subject to stringent constraints from direct dark matter search experiments. In the following two

subsections we discuss upper bounds on the couplings that result from perturbativity and unitarity constraints. In the final subsection the pre-collider bounds on the remaining free parameters are summarized and our final choice of free parameters is discussed.

3.2.1 Lagrangian and Free Parameters

As discussed in the overview, we consider a simplified model [32] where a massive spin-1 mediator connects the DSP to SM particles. The Lagrangian can then be written as

$$\mathcal{L} = \mathcal{L}_{\text{SM}} + \mathcal{L}_{\text{DSP}} + \mathcal{L}_R + \mathcal{L}_I. \quad (3.1)$$

We assume the DSP to be a spin-1/2 Dirac fermion. A Majorana fermion cannot have a vector interaction, but is otherwise basically the same as a Dirac fermion for our purposes.² The DSP part of the Lagrangian is therefore:

$$\mathcal{L}_{\text{DSP}} = \bar{\chi}(i\not{\partial} - m_\chi)\chi. \quad (3.2)$$

In MadGraph convention [98] the mediator part of the Lagrangian is:

$$\mathcal{L}_R = -\frac{1}{4}F^{\mu\nu}F_{\mu\nu} - \frac{1}{2}m_R^2 R^\mu R_\mu, \quad \text{with } F_{\mu\nu} \equiv \partial_\mu R_\nu - \partial_\nu R_\mu. \quad (3.3)$$

Finally, the interactions of the mediator with fermions are described by the Lagrangian

$$\mathcal{L}_I = \sum_q R_\mu \bar{q}\gamma^\mu (g_q^V - g_q^A \gamma^5) q + R_\mu \bar{\chi}\gamma^\mu (g_\chi^V - g_\chi^A \gamma^5) \chi. \quad (3.4)$$

The free parameters of our model are thus the mediator mass m_R , the DSP mass m_χ , and the couplings of the mediator to quarks (g_q^V, g_q^A) and to the DSP (g_χ^V, g_χ^A) . In total, there are 16 parameters. However, since this chapter uses data from e^+e^- collision up to $\sqrt{s} = 209$ GeV, top quarks cannot contribute to the final state. Therefore the couplings g_t^V and g_t^A are irrelevant, so that 14 relevant free parameters remain.

An exhaustive scan of a 14-dimensional parameter space is not feasible with our computational resource. However, as we will see in the following subsections, non-collider constraints force many of these couplings to be very small, so that we can set them to zero for our purposes.

3.2.2 Dark Matter Constraints

In the standard thermal WIMP scenario, the dark matter relic density is essentially inversely proportional to the total DSP annihilation cross section computed in the non-relativistic limit [92]. In

² A complex scalar DSP behaves similar to a Majorana DSP if $m_R > m_b, m_\chi$. However, the contribution from the exchange of longitudinal messenger particles vanishes identically in this case, i.e. there are no terms that are enhanced by $m_b m_\chi / m_R^2$.

our model the DSP can always annihilate into sufficiently light quarks, with cross section [126]:

$$\begin{aligned}
 v\sigma(\bar{\chi}\chi \rightarrow \bar{q}q) &\simeq \frac{3m_\chi^2}{2\pi(m_R^2 - 4m_\chi^2)^2} \sqrt{1 - \frac{m_q^2}{m_\chi^2}} \\
 &\cdot \left[(g_q^V)^2 (g_\chi^V)^2 \left(2 + \frac{m_q^2}{m_\chi^2}\right) + 2(g_q^A)^2 (g_\chi^V)^2 \left(1 - \frac{m_q^2}{m_\chi^2}\right) + (g_q^A)^2 (g_\chi^A)^2 \frac{m_q^2}{m_\chi^2} \frac{(4m_\chi^2 - m_R^2)^2}{m_R^4} \right].
 \end{aligned} \tag{3.5}$$

Here v is the relative velocity between χ and $\bar{\chi}$. The last term on the right-hand side (rhs) of eq.(3.5) is due to the exchange of longitudinal R -bosons. Note that it is *enhanced* $\propto m_\chi^2 m_q^2 / m_R^4$ for small mediator masses; at the same time it is *suppressed* $\propto m_q^2 / m_\chi^2$ if $m_R > 2m_\chi \gg m_q$. The numerator of this term implies that it does not have a pole at $s \simeq 4m_\chi^2 = m_R^2$. If the vectorial couplings do not vanish, this term is therefore only relevant if the exchanged mediator is quite far off-shell. Notice also that this term is proportional to the product of axial vector couplings, i.e. it is absent for a purely vectorial theory. At the same time it is the only term that survives for vanishing vector couplings, e.g. if χ is a Majorana particle.

Moreover, for $m_\chi > m_R$ a $\chi\bar{\chi}$ pair can also annihilate into two mediators, which subsequently decay to quarks. The corresponding cross section is [126]:

$$\begin{aligned}
 v\sigma(\bar{\chi}\chi \rightarrow RR) &= \frac{(m_\chi^2 - m_R^2)^{3/2}}{4\pi m_\chi (m_R^2 - 2m_\chi^2)^2} \\
 &\cdot \left\{ 8(g_\chi^A)^2 (g_\chi^V)^2 \frac{m_\chi^2}{m_R^2} + \left[(g_\chi^A)^4 - 6(g_\chi^A)^2 (g_\chi^V)^2 + (g_\chi^V)^4 \right] \right\}.
 \end{aligned} \tag{3.6}$$

The first term in the second line again gives an enhancement $\propto m_\chi^2 / m_R^2$. Note that in the limit $v \rightarrow 0$, which we applied here, the contribution $\propto (g_\chi^A)^4 / m_R^4$, which is due to the production of two longitudinal R bosons, vanishes. Moreover, the cross section (3.6) is quite strongly phase space suppressed near threshold where $m_\chi \simeq m_R$.

Since the predicted DSP relic density is inversely proportional to the total $\chi\bar{\chi}$ annihilation cross section, requiring that the predicted DSP density is not larger than the total observed dark matter density imposes a lower bound on (sums of products of) the relevant couplings if the masses are fixed. The detailed analysis of ref.[126] shows that for $m_R \leq 100$ GeV this bound is easily satisfied if all axial vector couplings are $\gtrsim 0.3$ even for vanishing vector couplings. We will see below that LEP data only allow to probe significantly smaller m_R . We confirm that for coupling strengths of interest to LEP physics, in standard cosmology the thermal DSP relic density is always much below the desired dark matter density, unless the DSP is very light (with $m_\chi < m_R$ so that $\chi\bar{\chi} \rightarrow RR$ annihilation is suppressed) and has very small couplings to light quarks (see below).

The signal in direct dark matter detection experiments depends essentially on the mass of the dark matter particle and its scattering cross section on nucleons. For the latter one usually distinguishes between spin-dependent (SD) and spin-independent (SI) contributions. The calculation procedure has already been shown in section 2.3. For our case here, the corresponding cross sections can be written as [126]:

$$\sigma_N^{\text{SD}} = a_N^2 \frac{3\mu_N^2}{\pi m_R^4}; \quad \sigma_N^{\text{SI}} = f_N^2 \frac{3\mu_N^2}{\pi m_R^4}. \quad (3.7)$$

Here $N = n, p$ and

$$\mu_N = \frac{m_\chi m_N}{m_\chi + m_N} \quad (3.8)$$

is the reduced mass of the DSP–nucleon system. The coefficients f_N appearing in σ_N^{SI} are simply given by products of couplings:

$$f_p = g_\chi^V (2g_u^V + g_d^V); \quad f_n = g_\chi^V (g_u^V + 2g_d^V), \quad (3.9)$$

where the differences are due to the different valence quark content of neutrons and protons. Note that sea quarks do not contribute, since quarks and antiquarks couple with opposite sign to R ; their contributions cancel, since here the coherent coupling to the entire nucleon (in fact, in most cases to an entire nucleus) is relevant. Finally, the coefficients a_N appearing in σ_N^{SD} are:

$$a_N = g_\chi^A \sum_{q=u,d,s} \Delta q^{(N)} g_q^A. \quad (3.10)$$

Here $\Delta q^{(N)}$ is the contribution of the spin of quark q to the total spin of nucleon N . They can be determined from polarized deep–inelastic scattering experiments. The current Particle Data Group values [127] are:

$$\begin{aligned} \Delta u^{(p)} &= \Delta d^{(n)} = 0.84 \pm 0.02; \\ \Delta u^{(n)} &= \Delta d^{(p)} = -0.43 \pm 0.02; \\ \Delta s^{(p)} &= \Delta s^{(n)} = -0.09 \pm 0.02. \end{aligned} \quad (3.11)$$

There are strong upper bounds on the spin–independent scattering cross section on the proton. For $m_\chi \gtrsim 5$ GeV the tightest constraint comes from the PandaX–II [39] experiment, whereas CRESST [36] data impose significant constraints for $m_\chi \gtrsim 0.5$ GeV. We will see below that LEP data can only probe scenarios with $m_R < 100$ GeV. These bounds require $g_{u,d}^V$ to be below 0.1, usually much below this value. Such small couplings have little influence on LEP physics, so we set $g_u^V = g_d^V = 0$.³

The upper bounds on the spin–dependent cross sections become quite weak for WIMP mass below 4 GeV, but the bound on σ_n^{SD} is still below 10^{-2} pb for $m_\chi = 5$ GeV [128]. If $m_R \leq 10$ GeV this constraint suffices to imply $g_{u,d}^A \leq 0.1$, the bound on g_s^A being somewhat weaker but still strong enough to force these couplings to be negligible for LEP physics. On the other hand, for $m_R \geq 50$ GeV $\mathcal{O}(1)$ axial vector couplings are allowed even for the light quarks if we scale the bound on the scattering cross section by the ratio of the predicted χ relic density and the total observed dark matter density. However, in that case χ does not make a good thermal dark matter candidate. In most scenarios where the predicted χ relic density in standard cosmology is at least a sizable fraction of

³ The bounds on the spin–independent cross section have been derived under the assumption of equal scattering cross section on neutrons and protons, which need not be the case in our scenario. In fact, the cross section for scattering on any one isotope can be made to vanish for a particular (negative) ratio of g_u^V/g_d^V . However, by now experiments using many different isotopes have been performed, allowing to constrain g_u^V and g_d^V separately.

the observed dark matter density the upper bound on the spin dependent cross section for $m_\chi \gtrsim 4$ GeV requires the axial vector couplings to be too small to significantly affect LEP cross section. We therefore set $g_u^A = g_d^A = g_s^A = g_c^A = 0$; we require vanishing axial vector coupling to charm quarks since strange and charm quarks reside in the same $SU(2)$ doublet.

We are then left with eight free parameters: four couplings of R to quarks, two couplings of R to the DSP, and the masses of R and the DSP.

3.2.3 Perturbativity Condition

We will use leading order perturbation theory to derive constraints on our model from published LEP data. Perturbation theory becomes unreliable when the couplings become too large. Our calculations depend on the SM electroweak couplings, which are perturbative, and on the couplings of the mediator R . We constrain the latter through the simple condition

$$\Gamma_R < m_R, \quad (3.12)$$

where Γ_R is the total decay width of R . R can decay into $q\bar{q}$ and $\chi\bar{\chi}$ pairs, with partial widths:

$$\begin{aligned} \Gamma(R \rightarrow q\bar{q}) &= \frac{m_R}{4\pi} \sqrt{1 - 4z_q} \left[(g_q^V)^2 + (g_q^A)^2 + z_q \left(2(g_q^V)^2 - 4(g_q^A)^2 \right) \right]; \\ \Gamma(R \rightarrow \chi\bar{\chi}) &= \frac{m_R}{12\pi} \sqrt{1 - 4z_\chi} \left[(g_\chi^V)^2 + (g_\chi^A)^2 + z_\chi \left(2(g_\chi^V)^2 - 4(g_\chi^A)^2 \right) \right]. \end{aligned} \quad (3.13)$$

Here $z_f \equiv m_f^2/m_R^2$. The factor of 3 in the first equation comes from the colors of quarks. Of course, these widths are nonzero only for $m_R > 2m_f$, i.e. $z_f < 0.25$. The perturbativity condition can thus be written as

$$\sum_{2m_f < m_R} N_f \sqrt{1 - 4z_f} \left[(g_f^V)^2 + (g_f^A)^2 + z_f \left(2(g_f^V)^2 - 4(g_f^A)^2 \right) \right] < 12\pi. \quad (3.14)$$

This constraint can be used for $m_R \geq 1$ GeV, so that at least decays into strange quarks are possible. For somewhat heavier mediators, which can also decay into $c\bar{c}$ and perhaps $\chi\bar{\chi}$ pairs, the constraint (3.14) becomes stronger. We will only use combinations of parameters that respect this bound.

3.2.4 Unitarity Condition

Another important kind of constraint has first been discussed in ref.[123]: unitarity limits the size of the axial vector couplings of fermions f to the mediator R . One way to see this is to consider the cross section for $f\bar{f} \rightarrow R_L R_L$, where R_L denotes a longitudinally polarized R boson. For fixed (nonzero) relative velocity between f and \bar{f} , the matrix element scales like $(g_f^A m_f/m_R)^2$. This violates unitarity, unless

$$g_f^A \frac{m_f}{m_R} \leq \sqrt{\frac{\pi}{2}}. \quad (3.15)$$

Note that this bound applies both to the DSP, $f = \chi$, and to the quarks with non-vanishing axial vector coupling, $f = q$.

Another derivation of the unitarity constraint starts from the observation that in a renormalizable theory, R must be a gauge boson. If fermion f has non-vanishing axial coupling g_f^A to R , the two-component fermions f_L and f_R must transform differently under the R gauge symmetry. This

implies that the (Dirac) mass term $m_f \overline{f_L} f_R$ is not invariant under the R gauge symmetry. Hence m_f must be due to the vacuum expectation value of some Higgs field that carries R charge. The upper bound (3.15) then follows from the upper bound on the Yukawa coupling that gives rise to m_f .

The bound (3.15) limits the size of the enhancement due to the exchange of longitudinal R -bosons with axial vector coupling to massive fermions; see the discussion of eq.(3.5) above. We will see below that similar terms also appear in our signal cross sections. Neglecting the unitarity constraint (3.15) could thus lead to overly optimistic conclusions regarding the sensitivity of collider data to our model.

3.2.5 Summary: Free Parameters of the Model

The perturbativity condition (3.14) is quite weak. The unitarity constraint (3.15) can be strong for small m_R , but only applies to the axial vector couplings, and in any case still allows non-negligible couplings. These constraints therefore do not reduce the number of free parameters, i.e. we still have the eight free parameters enumerated at the end of Sec. 3.2.2. This parameter space is still too large for a thorough exploration.

We therefore assume equal vector couplings of s , c and b quarks. Recall that we set the vector couplings of u and d quarks to zero in order to satisfy constraints from direct detection experiments. As mentioned in the Introduction, we will investigate final states with either two jets and two DSPs, or with four jets. The searches we will use to probe $q\bar{q}\chi\bar{\chi}$ production do not require any flavor tagging, so to good approximation this cross section only depends on the sum $(g_s^V)^2 + (g_c^V)^2 + (g_b^V)^2$. Results for different ratios of the vector couplings therefore can be derived by simply re-scaling the results presented below. In contrast, the best published probe of the four-jet final state requires the detection of at least two b (anti)quarks in the final state. Since $b\bar{b}b\bar{b}$ final states have a significantly higher probability of satisfying this requirements than final states with only one $b\bar{b}$ pair, g_b^V contributes with higher weight to the final cross section after cuts than g_c^V and g_s^V .

Recall that scenarios where a light R can decay into a $\chi\bar{\chi}$ pair are strongly constrained by LHC “monojet” data. We will thus assume $m_R < 2m_\chi$. In that case the (tree-level) cross section for the four-jet final state is completely independent of the couplings g_χ^V and g_χ^A . Moreover, the cross section for $q\bar{q}\chi\bar{\chi}$ production is then proportional to the product $(g_q g_\chi)^2$. It is thus sufficient to present results for a fixed ratio of the couplings of the mediator to quarks and to DSPs; results for different ratios can then be obtained by re-scaling our results presented below.

In the end we are left with four free parameters: m_R , m_χ , g_b^A and g_q^V .

3.3 Application of LEP Data

In this Section we check whether published analyses of LEP data can impose significant constraints on the parameters of our model. We focus on analyses by the ALEPH collaboration [124, 125], because they are based on well-defined, and clearly described, cuts defining final states that receive contributions from the two processes we wish to probe. We expect data from the other three LEP experiments (DELPHI, L3 and OPAL) to have similar sensitivity, so a combined analysis could lead to somewhat stronger bounds.

In our numerical analysis we use FeynRules [97] to generate a model file in UFO format [129], MadGraph [98] to simulate the e^+e^- collision, and Pythia 8.2 [99] to perform the hadronization. We

apply the cuts defining the relevant ALEPH analyses at the hadron level, neglecting detector resolution effects. In the following two Subsections we discuss two-jet plus missing energy and four-jet final states, respectively.

3.3.1 Two Jets Plus Missing Energy

We start with the topology

$$e^+ e^- \rightarrow jet + jet + \cancel{p}, \quad (3.16)$$

where \cancel{p} stands for missing energy and momentum in the final state, i.e. the invariant mass of the two-jet system is significantly smaller than the center-of-mass energy \sqrt{s} . The extra Feynman diagrams contributing to this topology in our model are shown in Fig. 3.1. As usual we neglect the Higgs exchange diagrams since the $e^+ e^- H$ coupling is tiny. Since the couplings, g_q and g_χ , appear together in Fig. 3.1, the experiment data bound the product of g_q and g_χ . Therefore, in the following section, bounds on $\sqrt{g_q g_\chi}$ are shown.

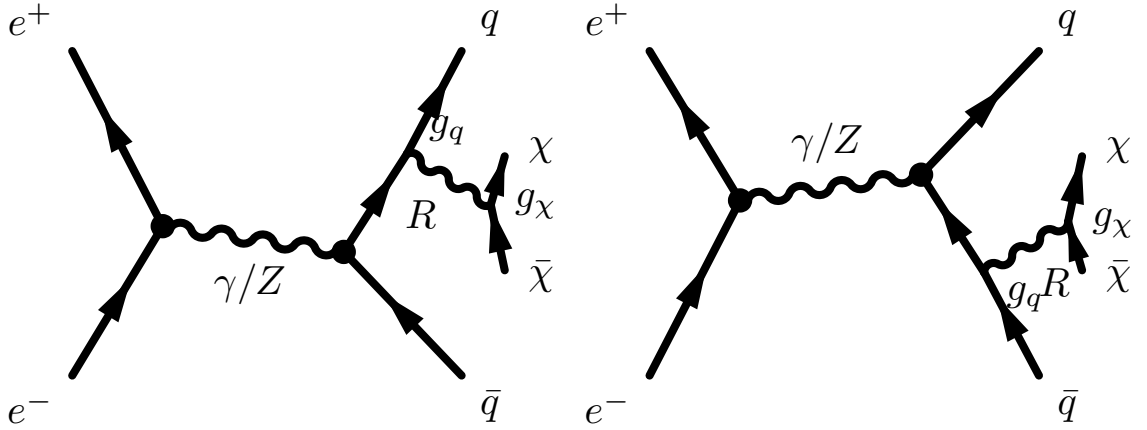


Figure 3.1: Leading order diagrams contributing to the final state (3.16) in our model. Note that the mediator R is always off-shell in the region of parameter space we are interested in.

Analysis of LEP2 Data

During the LEP2 period (data taken between 1995 and 2000, at center of mass energy $161 \text{ GeV} \leq \sqrt{s} \leq 209 \text{ GeV}$) ALEPH performed most searches for the topology (3.16) in the context of supersymmetric extensions of the SM. This includes searches for the pair production of squarks [130, 131] and neutralinos [132–136]. In addition, ALEPH searched for the production of an invisibly decaying Higgs boson produced in association with an on-shell Z boson [137–139]. Each of these searches uses dedicated cuts to suppress the SM background.

We generally find that the data taken at higher energies have better sensitivity to our model, if the event selection cuts are more or less independent of \sqrt{s} . The cross section for the four-body final state we are interested in depends quite sensitively on the available phase space. Note also that the integrated luminosity was higher at the higher energies. The total sensitivity is then essentially

determined by the data taken at higher energy. On the contrary, if the cuts strongly depend on \sqrt{s} , the cut efficiencies may vary strongly; in this case one should consider all analyses together.

The neutralino searches fall in the second category. The analyses of the data taken at $\sqrt{s} = 161$ and 172 GeV [132] use quite different cuts than the analyses of the data taken at $\sqrt{s} \geq 183$ GeV [133–136]. At these higher energies, on-shell production of two Z bosons becomes possible. The high-energy analyses impose a strong cut on the missing mass, which is designed to remove the $Z\bar{\nu}\nu$ background. Unfortunately this cut by itself excludes more than 90% of our signal, leading to a total cut efficiency of only about 2%. On the other hand, the lower energy analyses use a cut on the visible mass, not on the missing mass,¹ leading to a total cut efficiency of about 20% for our signal. The overall cross sections times luminosity at $\sqrt{s} = 161$ and 172 GeV are, however, too small. We therefore find that the analyses do not lead to significant bounds on our model.

For the invisibly decaying Higgs search, cut-based analyses were published only for data with $\sqrt{s} \leq 183$ GeV [137]. There is a published search for this channel using data taken at $\sqrt{s} = 189$ GeV [139], but it uses a Neural Network; since we cannot reproduce this analysis, we cannot use it to constrain our model. ALEPH did not publish any search for an invisibly decaying Higgs using data taken at $\sqrt{s} > 189$ GeV. When applied to our signal, the cuts used in the analyses [137, 138] at \sqrt{s} between 161 and 183 GeV have an efficiency of less than 10%. In this case the most harmful cuts are those related to the thrust and the reconstruction of the two jets. The relatively small cross sections, low integrated luminosity and insufficient cut efficiencies again imply that no meaningful constraints on our model can be derived.

We find the best sensitivity to our model when applying the cuts optimized for searches for squark pair production. Here cut-based analyses were published for the entire data set, including the highest energies. The cuts have been listed in Sec. 7 of ref.[131]²; when applied to our model, they frequently lead to an efficiency of $\geq 10\%$. This is still not ideal, but sufficient to derive some meaningful constraints on the parameters of our model.

In this chapter we focus on the part of parameter space where on-shell $R \rightarrow \chi\bar{\chi}$ decays are not allowed, i.e. $m_\chi > m_R/2$, since otherwise “monojet” searches by the LHC experiments [72, 126, 140] give much tighter constraints. In this part of parameter space our signal process is a genuine $2 \rightarrow 4$ reaction, with rather low cross section. We find that our recasting of the ALEPH squark searches does not lead to significant constraints if $m_R \gtrsim 10$ GeV. In Fig. 3.2 – 3.4 we therefore show results for $m_R = 1, 2$ and 5 GeV, respectively, focusing on scenarios with rather light DSP, $m_R/2 \leq m_\chi \leq 2m_R$. We find that the bounds on vector couplings are not as strong as those on the axial vector couplings, and

¹ Note that in general there is no simple relation between the missing and the visible mass of a given event. The visible mass is defined as $M_{\text{vis}}^2 = P_{\text{vis}}^2$, where P_{vis} denotes the sum of the 4-momenta of all “visible” particles; only neutrinos and DSPs are counted as “invisible”. The missing mass is defined by $M_{\text{miss}}^2 = (P_{\text{init}} - P_{\text{vis}})^2$, where P_{init} is the 4-momentum of the initial state. In some kinematical configurations both the visible and the missing mass are small.

² The cuts for “intermediate ΔM ” usually turned out to give the tightest constraints. The influential cuts are $N_{\text{ch}} > 11$, $M_{\text{vis}} > 15$ GeV, $p_T/\sqrt{s} > 4\%$, $E_{\text{vis}}/\sqrt{s} < 70\%$, $E_{12}/\sqrt{s} < 0.5\%$, $\cos\theta_{\text{miss}} > 0.8$, $\cos\theta_T > 0.8$, $\Phi_{\text{acop}} < 176^\circ$, $\Phi_T < 177^\circ$, $E_{\text{Wedge}}/\sqrt{s} < 12.5\%$, $\text{Thrust} < 0.94$, $p_T/E_{\text{vis}} > 12.5\%$, $E_{\text{had}}/\sqrt{s} < 55\%$, $E_{\text{NH}}/E_{\text{vis}} < 30\%$, and $E_{l1}^{30}/\sqrt{s} > 1\%$. Here N_{ch} is the number of good tracks (i.e., of charged particles); M_{vis} is the invariant mass of the visible system, E_{vis} is its energy and p_T is the absolute value of its transverse momentum, which is the same as the absolute value of the missing p_T ; θ_{miss} is the polar angle of the missing p vector; θ_T is the polar angle of the thrust axis; Φ_{acop} is the acoplanarity angle; E_{had} is the total measured energy excluding the contribution of identified charged leptons; and E_{Wedge} is the energy in a 30° azimuthal wedge around the missing transverse momentum. We also use many of these variables in the optimized cuts presented in Sec. 3.4, e.g. E_{12} , E_{NH} , E_{l1}^{30} , Φ_T , where their definition and physical significance are discussed.

do not depend strongly on m_R . Therefore, for nonzero g^A and small m_χ we set the vector couplings to zero and derive the upper bound on the axial vector coupling from the ALEPH data in Fig. 3.2 – 3.4, while we show results for $g^A = 0$ separately in Fig. 3.5. For $m_\chi \gtrsim 4$ GeV and $g^V = 0$ the resulting bound on g^A is weaker than the unitarity bound (3.15). In this case we set the axial vector coupling such that the unitarity bound is saturated, and derive the resulting upper limit on the vector coupling. This is the strongest possible constraint on the vector coupling that can be derived from our recasting of the ALEPH squark pair search. The larger sensitivity to the axial vector coupling again comes from contributions $\propto m_q m_\chi / m_R^2$ to the Feynman amplitude.

These terms dominate the cross section for $m_R = 1$ GeV (Fig. 3.2). As a result, the bound on the coupling becomes *stronger* as the DSP mass is increased. Evidently the enhanced contribution from longitudinal R exchange over–compensates the reduction of the phase space. For the entire range of m_χ shown the bound is stronger than the unitarity limit. Note that we show the bounds on $\sqrt{g_\chi^A g_b^A}$, because the unitarity limit due to m_χ is different compared to that due to m_b . Moreover, all vector couplings have been set to zero. Strictly speaking we would have to allow some coupling at least to s quarks in order to allow R to decay; however, vector couplings $\ll 1$ will not affect the bound on the axial vector coupling. On the other hand, $O(1)$ vector couplings would lead to a slightly stronger upper bound on the axial vector coupling.

The results for $m_R = 2$ GeV (Fig. 3.3) are qualitatively rather similar, but the bound on the axial vector coupling is weaker by a factor of about 1.5. As a result, for $m_\chi \geq 3.6$ GeV the upper bound on g_χ^A is actually set by the unitarity constraint (3.15). At $m_\chi = 4$ GeV a vector coupling as large as 0.89 has been turned on in order to saturate our recasting of the ALEPH bound, for axial vector coupling at the unitarity limit. This leads to a slight increase of the upper bound on the cross section, shown in the lower frame, which otherwise is very similar to the case with $m_R = 1$ GeV. Since in both cases m_R is much smaller than all other relevant energy scales in the problem, in particular much smaller than the missing energy required by the cuts, it is not surprising that the upper bound on the cross section does not depend on m_R .

On the other hand, for $m_R = 5$ GeV $\simeq m_b$ (Fig. 3.4) the enhancement due to the exchange of longitudinal R –bosons no longer suffices to over–compensate the reduced phase space when m_χ is increased. The ALEPH squark searches now permit quite large axial vector couplings even for m_χ near $m_R/2$. For $m_\chi \geq 4.5$ GeV this bound again becomes weaker than the unitarity constraint (3.15). Even if we saturate this constraint, sizable vector couplings are allowed by the ALEPH data, as shown by the dotted (blue) curve. Note that our perturbativity bound (3.14) requires $g_q^V \leq 2.5$ for $m_R = 5$ GeV. Fig. 3.3 and Fig. 3.4 show that our recasting of the ALEPH squark search limits leads to stronger upper bounds on this coupling if $m_\chi \leq 10$ GeV.

Having considered nonzero g^A , the bounds on g^V for vanishing g^A are shown in Fig. 3.5. Evidently the constraints on g^V are much weaker than those on g^A . Recall, however, that g^V is not constrained by the unitarity condition. The upper bound on g^V is therefore set by LEP2 data for $m_\chi \lesssim 30$ GeV; at even larger DSP masses, the LEP2 bound becomes weaker than the perturbativity condition (3.14). Another noticeable property is that for $m_\chi > 10$ GeV the upper bound on the vector coupling is nearly the same for our three choices of m_R , as is the bound on total cross section. This is due to the fact that the transverse R propagator becomes independent of m_R once $(2m_\chi)^2 \gg m_R^2$.

In Fig. 3.2, Fig. 3.3, and Fig. 3.4 we extended m_χ only to $m_\chi = 2m_R$. In Fig. 3.6 we show upper bounds on the couplings (upper) and on the total cross section (lower) for the same values of m_R , but for m_χ between 2 and 10 GeV. Moreover, we also compare the bounds on g^V for $g^A = 0$ (dotted

curves) to the bounds on g^V with g^A chosen to saturate its upper bound (dashed curves), which is set by the unitarity condition (3.15) once $m_\chi > 4$ GeV. In this case $g_\chi^A g_b^A \propto m_R^2/(m_\chi m_b)$, so that the contribution from longitudinal R exchange becomes largely independent of both m_χ and m_R once $(2m_\chi)^2 \gg m_R^2$. Note that the axial vector coupling also contributes to the exchange of transverse R bosons. This contribution simply scales like $(g^A)^2$, and is thus significant only for $m_R = 5$ GeV where unitarity allows relatively large axial vector couplings. This explains why the upper bound on g^V with maximal g^A is stronger for $m_R = 5$ GeV than for the smaller values of m_R . In contrast, if $g^A = 0$ the bound on g^V becomes independent of m_R once $(2m_\chi)^2 \gg m_R^2$, as we saw above. Overall Fig. 3.6 shows that the effect of g^A can be significant even if it is much smaller than g^V .

The lower frame of Fig. 3.6 again shows that the upper bound on the cross section becomes independent of m_R once $(2m_\chi)^2 \gg m_R^2$. We also see that for light R and $g^A \neq 0$, the upper bound on the cross section increases by nearly a factor of two once $m_\chi > 4$ GeV; evidently the cut efficiency becomes smaller. This coincides with the range of χ masses where the bound on the axial vector coupling is set by the unitarity constraint, so that the limit we derive from the ALEPH data can only be saturated by also including sizable vector couplings. The main observation is that the cut efficiency is much smaller if the process proceeds dominantly by vector coupling. For example, for $m_R = m_\chi = 1$ GeV, we find cut efficiencies between 1.5 and 3.5% for pure vector coupling, with couplings to b quarks yielding the highest sensitivity. In contrast, if the cross section is dominated by the axial vector coupling to b quarks the efficiency increases to 15%. This is at least partly due to the fact that the $\chi\bar{\chi}$ pair has to be in a P -wave in the R rest frame if the $\chi\bar{\chi}R$ coupling is purely axial vector, whereas a vector coupling allows S -wave contributions. The P -wave has a larger $\chi\bar{\chi}$ invariant mass, making it easier to pass cuts related to the missing mass or missing energy. The cut efficiency increases with increasing m_χ , which of course also implies larger $\chi\bar{\chi}$ invariant mass. However, even here pure vector couplings lead to lower cut efficiency. For example, for $m_\chi = 10$ GeV, i.e. at the end of the range shown in Fig. 3.6, we find a cut efficiency of just under 10% if g^A saturates the unitarity bound, with little dependence on m_R ; if $g^A = 0$, the cut efficiency is only about 7.5%.

We also find reduced cut efficiency if m_χ is only slightly above $m_R/2$. In this case configurations where the R boson is only slightly off-shell, i.e. configurations with small $\chi\bar{\chi}$ invariant mass, are even more strongly preferred dynamically than for larger values of the ratio m_χ/m_R . This again leads to a reduced efficiency for cuts related to the missing mass.

Analysis of LEP1 Data

Searches for the final state (3.16) were also performed at LEP1, the first period of operating the LEP collider (1989 to 1994), with $\sqrt{s} \simeq 91$ GeV $\simeq m_Z$ [141, 142]. These analyses searched for $H\nu\bar{\nu}$ production where H is the SM Higgs boson which is assumed to decay hadronically; this final state yielded the strongest lower bound on m_H that could be derived from a single LEP1 analysis.

Since the exchanged Z boson is now nearly on-shell, for not too large values of m_χ the total signal cross section is much larger than at LEP2. Moreover, the physics background at $\sqrt{s} \simeq m_Z$ is much smaller than at $\sqrt{s} \simeq 200$ GeV. In particular, the W^+W^- and ZZ backgrounds did not exist at LEP1. Therefore, less severe cuts were needed at LEP1, so the cut efficiency of our signal can be expected to be higher than for the LEP2 analyses. These two effects over-compensate the about three times smaller total luminosity accumulated at LEP1. At least for not too large DSP mass we therefore expect LEP1 data to lead to stronger constraints on the couplings of our model than LEP2 data.

In [141] the cuts and the number of selected events are not given in detail. We therefore cannot recast this analysis. Fortunately it is superseded by [142], where all applied cuts and the number of selected events are listed¹. Unfortunately there is some uncertainty regarding the precise jet definition that has been used. One of the cuts requires to reconstruct the final state as exactly three jets. We found that the results differ slightly for different jet algorithms. Moreover, occasionally the reconstruction of the event as three-jet event does not work; we discard such events. However, both the effect of having to discard events that cannot be described as three-jet events, and the differences between final results using different jet algorithms, are quite small, probably smaller than the effects of ignoring detector smearing, as we do. In the results presented below we use the k_T based Durham algorithm, which was the algorithm of choice for LEP2 analyses.

The results are shown in Fig. 3.7. Evidently for $m_\chi < 20$ GeV the bounds from LEP1 data are much better than those from the published analyses of LEP2 data. For larger DSP mass, however, the phase space constraints become quite severe at LEP1 energy, and hence these data quickly lose sensitivity. For pure axial vector coupling the upper bound on the coupling we derive from our recasting of the LEP1 data saturates the unitarity constraint at $m_\chi \simeq 23$ GeV, with larger m_R yielding a slightly larger range of m_χ where the experimental bound is below the unitarity limit. This can be understood as follows. The larger m_R , the larger the axial vector coupling allowed by unitarity. The contribution from longitudinal R exchange is again independent of m_R if the unitarity limit is saturated, but the contribution from the exchange of transversely polarized R bosons increases with increasing g^A , and hence becomes significant only for larger m_R . Note also that for small m_R the bound on g^A at first becomes stronger as m_χ is increased from its minimal value, which we took to be just above $m_R/2$ as before. As in Fig. 3.2 – 3.4 this is due to the exchange of longitudinal R bosons.

In contrast, for $g^A = 0$ the bounds on g^V are strongest for the smallest value of m_χ , where the R boson only needs to be slightly off-shell. The steep rise of the dotted curves towards small m_χ in the lower frame shows that the cut efficiency decreases, but this is over-compensated by the increase of the total cross section. Once $m_\chi > m_R$, the bound on g^V again becomes largely independent of m_R , and is (coincidentally) quite close to the bound on g^A for $m_R = 10$ GeV. The “experimental” upper bound on g^V becomes worse than the perturbativity constraint (3.14) once $m_\chi > 30$ GeV.

If $g^A \neq 0$ and $g^V = 0$ the cut efficiency of our signal is generally higher than 20%. For $5 \text{ GeV} < m_\chi < 10 \text{ GeV}$ the cut efficiency is even higher than 30%, and reaches the highest point of 32% for m_χ between 6 GeV and 7 GeV. For $g^V \neq 0, g^A = 0$ and relatively small $m_\chi \gtrsim m_R/2$ the cut efficiency is again less, typically around 10%, which is similar to the efficiency for the LEP2 squark pair search. However, it quickly increases for larger m_χ , reaching 35% for $m_\chi \simeq 15$ GeV. Moreover, for $m_\chi > 10$ GeV the cut efficiency is now actually higher for pure vector coupling than for pure axial vector coupling. This is opposite to the results shown in Fig. 3.6 for LEP2 energies. The LEP1 analysis mostly employs cuts on angular variables, and does not contain any explicit cut on the invisible mass or energy; recall that such cuts play a prominent role in the corresponding analysis of LEP2 data.

¹ The influential cuts are: $N_{\text{ch}} > 7$, $M_{\text{vis}} < 70$ GeV, $p_{\text{CH}}/\sqrt{s} > 0.1$, $E_{30}/E_{\text{vis}} > 60\%$, $E_{12} < 3$ GeV, $\theta_{\text{acol}} < 165^\circ$, $M_{\text{vis}} > 25$ GeV when $p_T/\sqrt{s} < 10\%$, $M_{\text{thrust}}^{1,2} > 2.5$ GeV, $\sum_{3j} \theta_{jj} < 342^\circ$, $\Phi_{\text{acop}} < 159^\circ$, and $\Theta_{\text{miss}}^{\text{iso}} > 31^\circ$. Here p_{CH} is the scalar sum of the charged particle momenta; E_{30} is the energy measured at more than 30° from the beam axis; $M_{\text{thrust}}^{1,2}$ is the invariant masses measured in both hemispheres according to the plane perpendicular to the thrust axis; and $\Theta_{\text{miss}}^{\text{iso}}$ is the largest cone around missing momentum vector containing energy less than 1 GeV. The other variables have already been defined in the LEP2 analysis described in Sec. 3.3.1.

3.3.2 Four Jet Analysis

We now turn to a discussion of the 4–jet final state. The signal again comes from the diagrams shown in Fig. 3.1, except that the (real or virtual) R –boson now decays into a $q\bar{q}$ pair rather than a $\chi\bar{\chi}$ pair. As a result, at tree–level the cross section now only depends on the couplings of R to quarks. We compute the signal by squaring the R –exchange contribution, i.e. we neglect interference between R –exchange and SM contributions. Note that the interference with the dominant (gluon exchange) SM contribution to the four quark final state is color suppressed¹; moreover, the total SM contribution to four parton final states is dominated by $q\bar{q}gg$ production, where g stands for a gluon.

There are several ALEPH analyses involving 4–jet final states. Some are optimized to detect W^+W^- or ZZ final states. These are part of the background for us; hence these analyses cannot be used to derive useful bounds on the couplings of our model. The earliest ALEPH analyses of the 4–jet final state in the LEP2 era had very low luminosity [143] or did not veto ZZ events [144], and are hence also only of limited usefulness for our purpose.

In contrast, the searches for neutral Higgs bosons, either in pairs or in association with a Z boson, investigate final states that are at least somewhat similar to ours. More importantly, they include cuts that attempt to minimize non–Higgs SM backgrounds, both from electroweak and from QCD sources. The related analyses cover the entire LEP2 energy range, from $\sqrt{s} = 133$ to 209 GeV [145–152]. The analyses of the data taken at $\sqrt{s} \leq 172$ GeV all use similar cuts, while the analyses of data taken at $\sqrt{s} \geq 183$ GeV apply another group of cuts in order to reduce W^+W^- and ZZ backgrounds. The first group of analyses turns out to be essentially useless for us, due to the rather low energy and comparatively small integrated Luminosity.

However, the data taken at $\sqrt{s} \geq 183$ GeV do allow to impose meaningful constraints on our model. Although the cuts applied in these analyses are similar, the slight changes still influence the final efficiencies. We find the highest efficiency, of about 27% with little dependence on m_R , for the cuts applied to the data taken at $\sqrt{s} = 183$ GeV [147]², where the Z pair background is still very small. At the highest energy the efficiency falls to about 21 to 22%. As a result, the strongest bound can be derived from the ALEPH analysis of the data taken at $\sqrt{s} = 183$ GeV. This is shown in Fig. 3.8.

The 183 GeV analysis performs quite well. For pure axial vector coupling (dashed curves) the final cut efficiency for our signal is actually as good as the one for the all–hadronic ZH signal for which this analysis was originally designed. This leads to quite stringent bounds, in particular for small m_R , where it is significantly stronger than that from the 2–jet plus missing energy analysis of LEP2 data described in the previous Section even for small m_χ , if we assume $g_q = g_\chi$; of course, the constraints we derive from the analysis of the four jet final state are independent of m_χ and g_χ , as long as $m_\chi > m_R/2$. However, for vanishing vector couplings our “experimental” bound on g_b^A is still

¹ Denote the final state by $q(k_1)\bar{q}(k_2)q'(k_3)\bar{q}'(k_4)$, where q' may be a different flavor from q . The gluon exchange contribution where $q'(k_3)\bar{q}'(k_4)$ results from the splitting of a virtual gluon then only interferes with the R exchange contributions where $q'(k_3)\bar{q}(k_2)$ or $q(k_1)\bar{q}'(k_4)$ originate from the decay of the R boson. Evidently this is possible only if $q' = q$, i.e. for final states with two identical $q\bar{q}$ pairs. Moreover, the interference gets a color factor of 1, compared to a factor $N_c^2 = 9$ for the squared R exchange diagram. We checked explicitly for some combinations of parameters that the interference terms change the total cross section only by a few percent.

² The influential cuts are: at least 2 b –jets, $N_{\text{ch}} > 7$, $\min(\cos \theta_{ij} + \cos \theta_{kl}) < -1.3$ ($ijkl$ label the four jets), $\min(\sum_{i=1}^4 \theta_{jj}^i) > 350^\circ$, and either $y_{34} > (2.9 - \#b - \text{jets})/9.5$ (transition from 4 to 3 jets through Durham algorithm), or $m_{12} > 78$ GeV, $m_{34} > 55$ GeV, and $y_{34} > 0.008$. Here θ_{ij} is the opening angle between jets i and j , m_{ij} is the invariant mass of the system of jets i and j ; θ_{jj}^i is any one of these six opening angles, with the sum going over the smallest four; $\#b - \text{jets}$ is the number of tagged b –jets.

slightly weaker than the one derived from the unitarity constraint (3.15) applied to the b quark, where we used $m_b(m_b) = 4.25$ GeV.

Turning on a vector coupling $g_q^V = 1$ for $q = s, c, b$ reduces the cut efficiency somewhat; this leads to increased upper bounds on the total cross section. This is presumably again due to the P -wave nature of the $q\bar{q}$ pair that originates from the “decay” of the virtual R boson via an axial vector coupling, which leads to a larger separation between these two partons, and hence better separated jets. Nevertheless the resulting upper bound on g_b^A that we derive from the 183 GeV analysis is now better than the one from the unitarity condition. This is in particular true for larger m_R ; the vector contribution depends less strongly on the mass of the mediator, since there are no terms $\propto m_b^2/m_R^2$ in this case. For small m_R the upper bound on a pure vector coupling is rather weak, but still stronger than the perturbativity limit (3.14).

The bounds on the coupling become significantly stronger once on-shell $R \rightarrow b\bar{b}$ decays become possible. This region of larger m_R is explored in Fig. 3.9. Since the unitarity bound becomes weaker for higher m_R , the final bound on the coupling is given by our recasting of the LEP2 search until $m_R \simeq 70$ GeV, where it becomes comparable to the upper bound (3.14) from perturbativity. Over most of the range of m_R shown, the curves for $g_q^V = 0$ and $g_q^V = 1$ behave similarly. Nevertheless, there are some differences for m_R around 10 to 15 GeV. For pure axial vector coupling the bound on the coupling begins to rise again just after the point where on-shell $R \rightarrow b\bar{b}$ decays are allowed. In contrast, if the vector coupling is sizable, $g_q^V = 1$, the lowest bound on the axial vector coupling is obtained for $m_R \simeq 12$ GeV. The reason is that contributions due to the exchange of longitudinal R bosons, which only comes from g^A , more strongly prefer small m_R . Hence turning on a vector coupling moves the peak of the cross section for fixed coupling to slightly larger values of m_R , where on-shell $R \rightarrow b\bar{b}$ decays are less phase space suppressed.

We also tried scenarios with pure vector coupling, setting $g_b^A = 0$ (magenta dotted lines in Fig. 3.8 and 3.9). As in case of the 2-jet plus missing energy analysis the resulting bound on the vector coupling is considerably weaker than that on g^A for $m_R < 5$ GeV. This is partly due to the absence of the term enhanced by m_b^2/m_R^2 , and partly due to the limited cut efficiencies, which are below 10% in this case. For $m_R < 2m_b$ the bound on the vector coupling does not depend much on m_R . The strongest bound appears for $m_R \gtrsim 2m_b$. It gradually weakens again for larger m_R , saturating the perturbativity condition (3.14) around $m_R = 35$ GeV. In this case the cut efficiency is smaller than in the scenarios with non-vanishing g^A , as can be seen from the larger upper bound on the total signal cross section.

We saw that in case of the two jet plus missing E_T analysis the strongest bound often comes from LEP1 data rather from LEP2 data, due to the larger signal cross section (for not too large m_χ) and smaller SM background. Unfortunately the only published ALEPH new physics searches at LEP1 using four jet final states [141, 153] are based on early data samples with very low integrated luminosity of 1.16/pb. These searches were designed for the pair production of particles with sizable coupling to the Z boson, e.g. light charged Higgs bosons, with each new particle decaying into a pair of jets. The early data set was sufficient to exclude such particles with mass nearly up to $M_Z/2$; at the time there was thus little motivation to perform new physics searches in the four jet final state using the full LEP1 data sample. Even in the absence of backgrounds the early analyses could improve on the bounds we derive from the LEP2 searches only if the cut efficiency of signal events was higher than 50%; this is even higher than the efficiency of the final states for which these searches were originally optimized. We conclude that among the published four jet analyses, the one based on data taken at $\sqrt{s} = 183$ GeV data gives the tightest constraints on our model.

3.4 Improved Analysis of LEP2 Data

In Sec. 3.3 we saw that the cuts applied in the searches for 2–jet plus missing energy searches in LEP2 analysis published by the ALEPH collaboration have limited efficiency for our signal, below 5% in some cases, which is obviously not satisfactory. In this Section we therefore propose new cuts, which have much better efficiency for our signal but still remove most SM backgrounds. We employed kinematical variables also used by ALEPH, and applied them to SM events generated with Pythia 8.2 [99]. The cuts are designed to remove all SM backgrounds that may appear for the energy level up to 208 GeV. When analyzing data taken below the Z pair threshold part of the cuts can be loosened or removed, which would increase the cut efficiency even further. As the cut efficiency of the 4–jet signature as applied to our model is already as good as that of the ZH search for which this analysis was originally optimized, we only try to redesign the selection rules for the $jj\cancel{p}$ signature.

We start by requiring at least 5 good tracks in the event; this essentially guarantees that the event contains some hadronic activity.

Most multi–hadron events produced by LEP2 were not due to e^+e^- annihilation. Rather, they were produced when both the electron and the positron emitted a space–like photon; these two photons then collided to produce a multi–hadronic final state. Since the virtuality of these photons can be of order of the electron mass, they can be considered to be quasi–real. This class of events is therefore often called two–photon (or $\gamma\gamma$) events. The first set of cuts, listed above the second double line in Table 3.1, are designed to greatly reduce this background. These cuts are adapted from the cuts against two–photon events employed in ref.[132]; we use the same kinematical variables, but change some of the cut values since we optimize our analysis for higher energies, $\sqrt{s} = 208$ GeV.

Double Jet + Missing Energy ($jj\cancel{p}$)	
Variable	Selection Rule
M_{vis}	> 4 GeV
p_T/E_{vis}	$> 20\%$
$ \cos \theta_{\text{miss}} $	< 0.95
$\Delta\Phi_T$	$< 170^\circ$
E_{NH}	$< 30\% E_{\text{vis}}$
(NH=Neutral Hadron)	$30\% \leq E_{\text{vis}} < 45\% \quad p_{T(\text{NH})} > 1.8\% \sqrt{s}$
E_{l_1}/\sqrt{s}	$< 10\%$
E_{l_2}/\sqrt{s}	$< 5\%$
$E_{l_1}^{30}/\sqrt{s}$	$> 1\%$
Durham	$M_{j_1} \leq 9M_{j_2}$ and $M_{j_2} \leq 9M_{j_1}$
2-jet j_1j_2	$M_{j_1j_2} \leq 80$ GeV or $M_{j_1j_2} \geq 100$ GeV
y_{23}	< 0.02

Table 3.1: Cuts designed to reduce the SM background to the two jet plus missing E_T signal. The cuts listed above the last horizontal double line are mostly directed against two–photon events, whereas the cuts below this double line help to remove background events containing on–shell W or Z bosons. See the text for further details.

The first of these cuts requires the invariant mass of the system consisting of all detected particles

to exceed 4 GeV. Since the probability for the emission of a nearly on-shell photon off an energetic electron or positron quickly increases with decreasing photon energy, the $\gamma\gamma$ background peaks at small values of this variable.

The second cut imposes a lower bound on the total transverse momentum of the system of visible particles. Since photons are mostly emitted with small virtuality, the $\gamma\gamma$ system typically has small total transverse momentum. It is nonzero partly due to measurement errors, and partly because the detector is not hermetic. In particular, an outgoing e^\pm can carry some transverse momentum but still escape detection. It is important to note that this cut also removes $e^+e^- \rightarrow q\bar{q}$ annihilation events (including events with additional gluon emission), since here the total visible transverse momentum is also close to zero.

The third cut vetoes events where the missing momentum vector, which is simply the opposite of the total 3-momentum of all detected particles, points nearly in the forward or backward reaction. There is no reason why the two quasi-real photons should have similar energy. If the outgoing e^\pm remain undetected, two-photon events therefore typically have a large longitudinal momentum of detected particles, i.e. the total missing momentum vector is dominated by its longitudinal component.

The fourth cut employs the transverse acoplanarity angle $\Delta\Phi_T$ defined in [131]. It removes events where the momenta in two hemispheres are nearly back-to-back. This cut is again efficient against both two-photon and $e^+e^- \rightarrow q\bar{q}$ annihilation events.

The next cut, which we again copy from ALEPH analyses, uses the energy E_{NH} carried by neutral hadrons. It can be measured by subtracting the energy associated with the tracks of charged particles from the total energy measured in the calorimeters. All events where E_{NH} is less than 30% of E_{vis} pass this cut. Events where $E_{\text{NH}} > 0.45E_{\text{vis}}$ are always removed. If E_{NH} lies between these two values, events only pass if the visible p_T not including neutral hadrons, called $p_{T\bar{\text{NH}}}$ in the Table, is at least $0.018\sqrt{s}$. The purpose of this combination of cuts is to remove events where a large fraction of the energy, or of the transverse momentum, is assigned to neutral hadrons. This can be dangerous, since the energies and momenta of neutral hadrons are least well determined experimentally of all “visible” particles (i.e., not counting neutrinos or DSPs); hence these events may contain a large amount of “fake” missing (transverse) energy, due to mismeasurement of the neutral hadrons.

The penultimate cut in this category vetoes events with energetic charged leptons (electrons or muons); l_1 is the most energetic identified charged lepton in the event. This removes two-photon events where at least one of the photons is so far off-shell that the corresponding outgoing e^\pm becomes detectable. This cut will also be effective against other backgrounds, in particular against events with leptonically decaying W bosons; these events are dangerous since they also contain a neutrino, which leads to an imbalance of the visible (transverse) momentum. Of course, events that do not contain a charged lepton also pass this cut.

The last cut against two-photon events removes events where the energy E_{12} deposited in forward or backward direction (within 12° of the beam axis) exceeds $0.05\sqrt{s}$. Note that two-photon events can have a sizable visible energy, even if the transverse momentum is typically small. This cut also removes events where one of the outgoing e^\pm hits the detector, but is not identified as a charged lepton.

The second group of cuts mostly targets events with real W or Z bosons. The first of these uses the variable $E_{l_1}^{30}$, which is the energy of particles in a 30° half-angle cone around the most energetic charged lepton (excluding the lepton itself). This cut is applied only if the event contains such a lepton. It removes events where this lepton is isolated, which is typically the case for leptons from leptonic W^\pm decays. In contrast, charged leptons produced in the decay of c or b quarks typically have a lot of hadronic activity nearby, i.e. large values of $E_{l_1}^{30}$, and thus pass this cut.

The three final cuts concern the jet system. In order to apply these cuts, the event is forced into a two-jet topology using the Durham k_T algorithm. The first cut removes events where one jet is very “slim”, i.e. has very small invariant mass. This is often the case for a jet from a hadronically decaying τ lepton. This cut thus removes events containing real $W^\pm \rightarrow \tau^\pm \nu_\tau$ decays. The second cut removes events where the di-jet invariant mass is close to M_Z ; this removes ZZ events with one Z boson decaying hadronically and the other into a neutrino pair, i.e. invisibly. The last cut removes events where the event would be reconstructed as containing three or more jets for dimensionless resolution variable $y_{23} = 0.02$. We find that this cut removes very efficiently that part of the $e\nu_e W$ background that survived the lepton cuts.

Some resulting cut efficiencies are listed in Table 3.2 to 3.4. We focus on scenarios with rather light mediator and light DSP, where the efficiency of our signal for the published missing energy searches at LEP2, discussed in the previous Section, was especially poor. We list the detailed cut efficiencies from previous sections in Appendix A.3 for comparison. In general, cut efficiencies of the best 4-jet analysis is much better than the di-jet case. Obviously, in Table 3.2 – 3.4, our new cuts highly improved the original cut efficiencies. For $m_R = 5$ GeV, Table 3.2, we show efficiencies for pure vector and pure axial vector couplings separately; for $m_R = 2$ GeV, Table 3.3, and $m_R = 1$ GeV, Table 3.4, we only show results for pure axial vector coupling, since outside the region $m_\chi \simeq m_R/2$ the cut efficiency for pure vector coupling has very little dependence on m_R .

$m_R = 5$ GeV				
m_χ/GeV	2.5	3.0	3.5	4.0
ϵ_A	18.48%	23.53%	27.54%	29.22%
ϵ_V	12.32%	15.55%	18.09%	19.83%
m_χ/GeV	4.5	5	5.5	6.0
ϵ_A	30.74%	32.21%	33.42%	33.58%
ϵ_V	21.43%	22.53%	22.97%	23.52%
m_χ/GeV	6.5	7.0	7.5	8.0
ϵ_A	34.46%	35.02%	34.76%	35.57%
ϵ_V	25.94%	25.44%	26.14%	27.25%
m_χ/GeV	8.5	9.0	9.5	10.0
ϵ_A	35.51%	35.45%	36.15%	36.25%
ϵ_V	27.29%	27.26%	28.37%	29.43%

Table 3.2: Cut Efficiencies for $m_R = 5$ GeV and $m_R/2 \leq m_\chi \leq 2m_R$. ϵ_A has been computed with pure axial vector coupling, $g_q^V = g_\chi^V = 0$, while ϵ_V is the efficiency for pure vector coupling, assumed to be the same for s, c and b quarks, while $g_\chi^A = g_q^A = 0$.

We see that the efficiency for pure vector coupling quickly increases from $m_\chi = m_R/2$ to $m_\chi \simeq m_R$, and then gradually increase to 35% for $m_\chi > 25$ GeV. These efficiencies are about three times higher than those for the published analysis discussed in the previous Section.

Turning to axial vector couplings, the cut efficiency for any combination (m_R, m_χ) is again better than the corresponding one in the published analysis described in the previous Section. For example, for $m_R = 2m_\chi$, the efficiency is more than three times larger. As in case of vector couplings, the cut efficiency quickly increases when m_χ is raised from $m_R/2$ to m_R ; it continues to increase more slowly

$m_R = 2 \text{ GeV}$				
m_χ/GeV	1.0	1.2	1.4	1.6
ϵ	21.98%	25.82%	27.59%	29.30%
m_χ/GeV	1.8	2.0	2.2	2.4
ϵ	29.25%	30.91%	31.08%	31.65%
m_χ/GeV	2.6	2.8	3.0	3.2
ϵ	32.07%	32.86%	33.36%	33.65%
m_χ/GeV	3.4	3.6	3.8	4.0
ϵ	33.25%	33.40%	34.29%	34.49%

Table 3.3: Cut Efficiencies for $m_R = 2 \text{ GeV}$ and $m_R/2 \leq m_\chi \leq 2m_R$. We have assumed pure axial vector coupling, $g_q^V = g_\chi^V = 0$.

$m_R = 1 \text{ GeV}$				
m_χ/GeV	0.5	0.6	0.7	0.8
ϵ	24.36%	27.36%	28.99%	28.57%
m_χ/GeV	0.9	1.0	1.1	1.2
ϵ	28.77%	29.49%	30.71%	30.23%
m_χ/GeV	1.3	1.4	1.5	1.6
ϵ	30.85%	30.82%	31.43%	30.22%
m_χ/GeV	1.7	1.8	1.9	2.0
ϵ	31.98%	31.19%	32.38%	31.25%

Table 3.4: Cut Efficiencies for $m_R = 1 \text{ GeV}$ and $m_R/2 \leq m_\chi \leq 2m_R$. We have assumed pure axial vector coupling, $g_q^V = g_\chi^V = 0$.

for even higher m_χ , reaching slightly more than 40% for $m_\chi > 30 \text{ GeV}$. Cut efficiencies of 30 to 40% are quite typical for many LEP searches.

The selection cuts were chosen to remove most SM backgrounds. We simulated $\gamma\gamma$ (i.e., $e^+e^- \rightarrow e^+e^-q\bar{q}$) events; events with hadronically decaying W^+W^- or ZZ pairs leading to events with four hard partons prior to showering; $Z\bar{\nu}\nu$, Zl^+l^- and $Wl\nu_l$ events where the gauge boson decays hadronically; and $e^+e^- \rightarrow q\bar{q}$ annihilation events. We include “purely hadronic” final states since they can contain heavy b or c quarks whose semileptonic decays can produce energetic neutrinos, and hence lead to significant amounts of missing energy. The $Z\bar{\nu}\nu$, Zl^+l^- and $Wl\nu_l$ events include contributions where the lepton pair comes from the decay of a (nearly) on-shell Z or W boson, but also contributions that only arise at third order in electroweak couplings. The latter diagrams do not contribute very much to the total cross sections for these final state, but populate different regions of phase space.

Our cuts remove more than 99.9% of most of these SM backgrounds. The exceptions are the $Wl\nu_l$ and $Z\bar{\nu}\nu$ final states, where 1.05% and 5.03%, respectively, of all generated events pass the cuts. MadGraph finds total cross sections of 7.34 pb and 0.33 pb, respectively, for these two final states, leading to a total SM background of about 0.1 pb. Recall that the upper bounds on the signal cross section we derived in the previous section, shown in the lower frames of Fig. 3.2–3.6, were $\geq 0.1 \text{ pb}$.

For parameter choices that saturate these earlier bounds, the new cuts would therefore lead to comparable signal and background cross sections. Since we cannot apply the new cuts to the actual data, we cannot quote the resulting bounds, even if the cut efficiencies are roughly doubled over a broad range of parameters. In order to give some idea of the expected improvement, we give some sensitivity limits, i.e. expected bounds (computed under the assumption that the observed number of events agrees exactly with the SM prediction). To this end, we use the p -value test of the “null” hypothesis (SM only) for a 95% confidence level. For $m_R = 5$ GeV with $g^V = 0$, the upper limit on g^A is improved from 1.48 to 1.39 at $m_\chi = 2.5$ GeV, and the point that LEP data is weaker than unitarity condition (3.15) moves from $m_\chi = 4.5$ GeV to 5 GeV. The sensitivity to the vector couplings increases even more. For $m_R = 5$ GeV and $m_\chi = 2.5$ GeV with $g^A = 0$, the bound of g^V is improved from 1.36 to 0.99. For $m_R = 5$ GeV and $m_\chi = 10$ GeV, the expected bound on g^V is improved from 2.15 to 1.88 with $g^A = 0$, and from 1.64 to 1.53 with non-zero g^A reaching unitarity bound. We repeat that actual bounds can only be derived by applying our cuts to real data.

Further optimization of the cuts, in order to maximize S/B or S/\sqrt{B} where S is the signal and B is the background, should be possible. For example, the (dominant) $Wl\nu_l$ background can be further reduced by slightly reducing the lower end of the excluded region of the invariant mass of the di-jet system (the penultimate cut in Table 3.1). However, such an optimization should also include detector effects, which is difficult for us to do reliably. This analysis nevertheless makes it appear likely that the bounds we derived in the previous Section, which used published analyses not optimized for this final state, can be improved significantly.

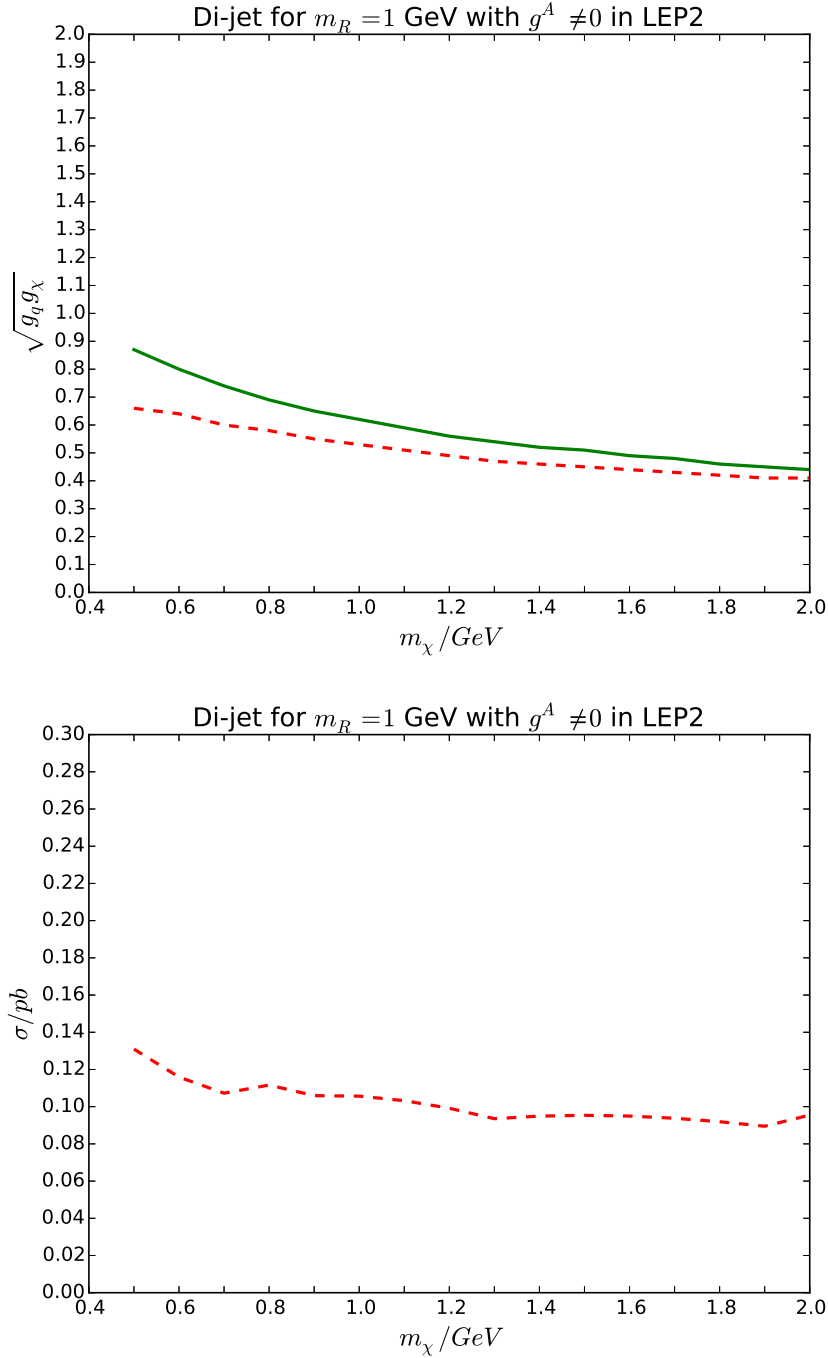


Figure 3.2: The upper frame depicts the bound on $\sqrt{g_q g_\chi}$. The solid (green) curve shows the bound on g^A from the unitarity condition (3.15). The dashed (red) curve shows the bound on g^A from the combination of the unitarity condition and our recasting of the ALEPH squark pair search limits. The lower frame shows the upper bound on the total signal cross section at $\sqrt{s} = 208$ GeV from our recasting of the ALEPH limits. In these figures the mass of the mediator $m_R = 1$ GeV. Here all vector couplings have been set to zero, i.e. $g_q = g_q^A$, $g_\chi = g_\chi^A$.

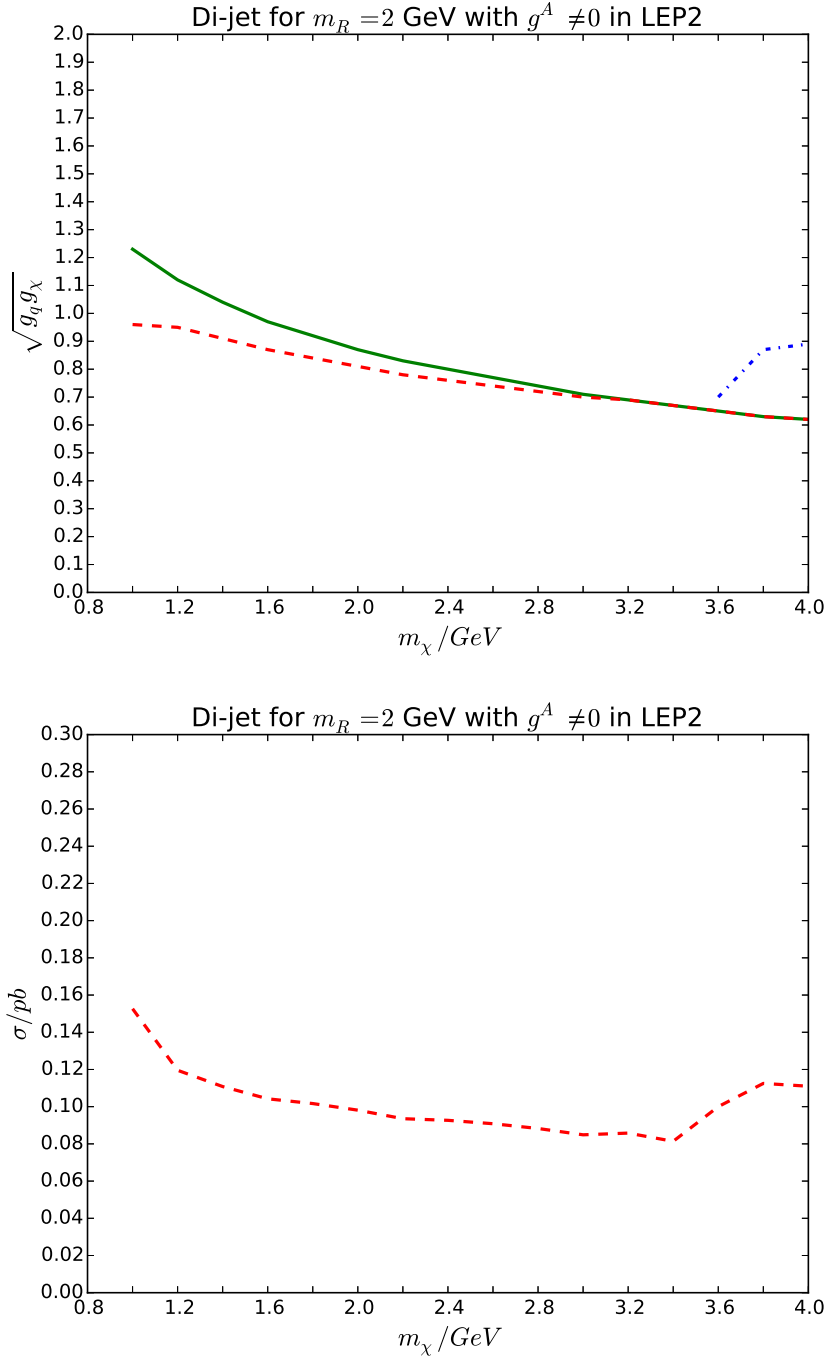


Figure 3.3: The meaning of the curves in the lower frames, and of the solid and dashed curves in the upper frames, is as in Fig. 3.2, but for mediator mass $m_R = 2$ GeV. For $m_\chi \geq 3.6$ GeV the solid and dashed curves coincide, i.e. the unitarity condition gives the stronger bound on the axial vector coupling. The dotted (blue) lines show the upper bound on the vector coupling that we derive from the ALEPH search, i.e. for these curves, $g_q g_\chi = g_q^V g_\chi^V$; the axial vector couplings were chosen such that the unitarity limit is saturated. In this mass range the upper bound on the signal cross section shown in the lower frames also uses the maximal axial vector coupling allowed by unitarity.

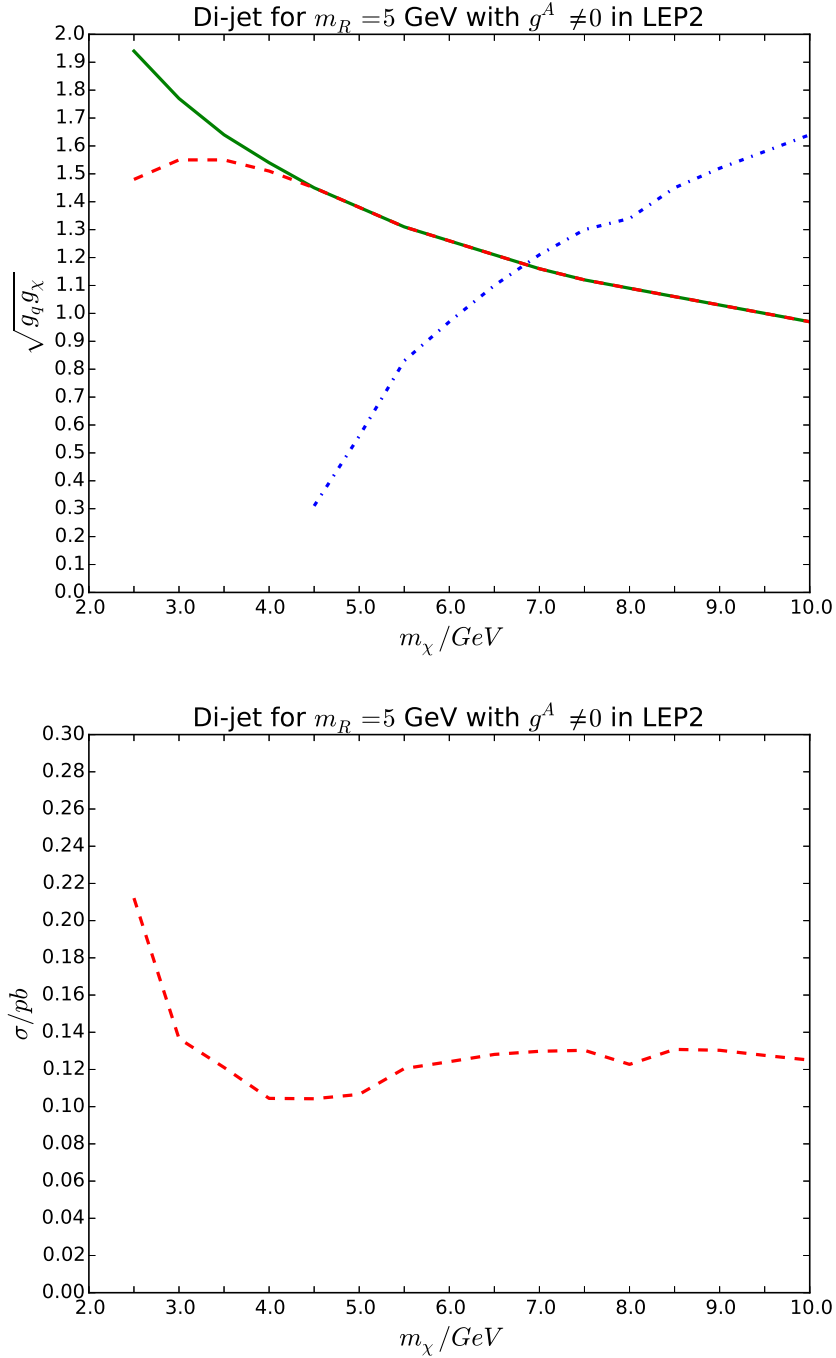


Figure 3.4: The meaning of the curves in the lower frames, and of the solid and dashed curves in the upper frames, is as in Fig. 3.2, but for mediator mass $m_R = 5$ GeV. For $m_\chi \geq 4.5$ GeV the solid and dashed curves coincide, i.e. the unitarity condition gives the stronger bound on the axial vector coupling. The dotted (blue) lines show the upper bound on the vector coupling that we derive from the ALEPH search, i.e. for these curves, $g_q g_\chi = g_q^V g_\chi^V$; the axial vector couplings were chosen such that the unitarity limit is saturated. In this mass range the upper bound on the signal cross section shown in the lower frames also uses the maximal axial vector coupling allowed by unitarity.

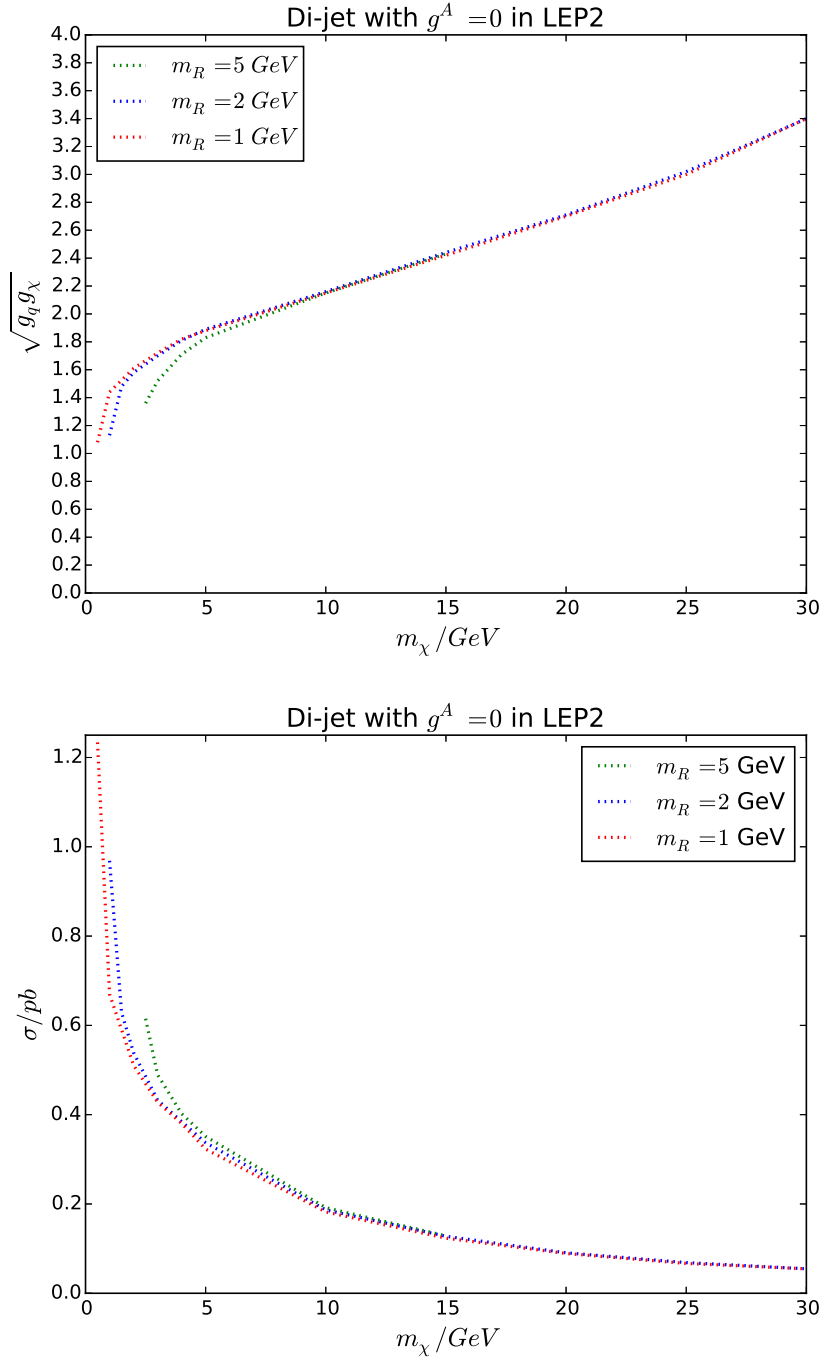


Figure 3.5: The upper frame depicts the bound on $\sqrt{g_q^V g_\chi^V}$, while the lower one shows the upper bound on the total signal cross section at $\sqrt{s} = 208 \text{ GeV}$ from our recasting of the ALEPH limits; all axial vector couplings have been set to zero. The green, blue and red curves are for $m_R = 5, 2$ and 1 GeV , respectively. For $m_\chi > 30 \text{ GeV}$ the bound on g^V is weaker than the perturbativity condition (3.14).

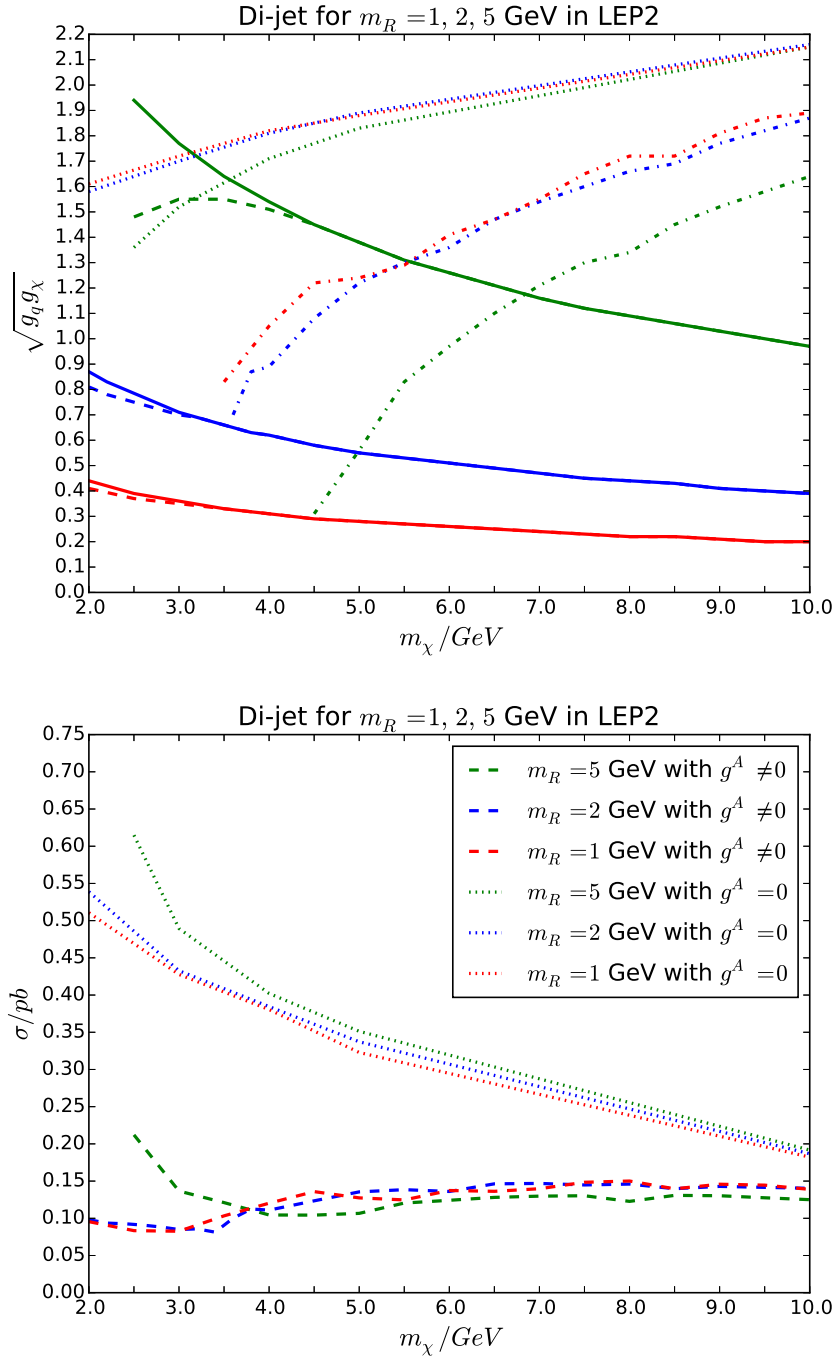


Figure 3.6: The upper frame shows upper bounds on the couplings of the mediator. The solid lines are from the unitarity condition (3.15), while the dashed lines are from our recasting of the ALEPH squark search; both sets of curves refer to axial vector couplings. If the unitarity constraint is stronger, we allow non-vanishing vector couplings; their upper bounds, derived from the ALEPH data, are shown by the dot-dashed curves. If $g^A = 0$, the unitarity condition are irrelevant, and the bounds on g^V become weaker. They are shown by the dotted curves. The green, blue and red curves are for $m_R = 5, 2$ and 1 GeV, respectively. The lower frame shows the corresponding upper bound on the total signal cross section before cuts at $\sqrt{s} = 208$ GeV.

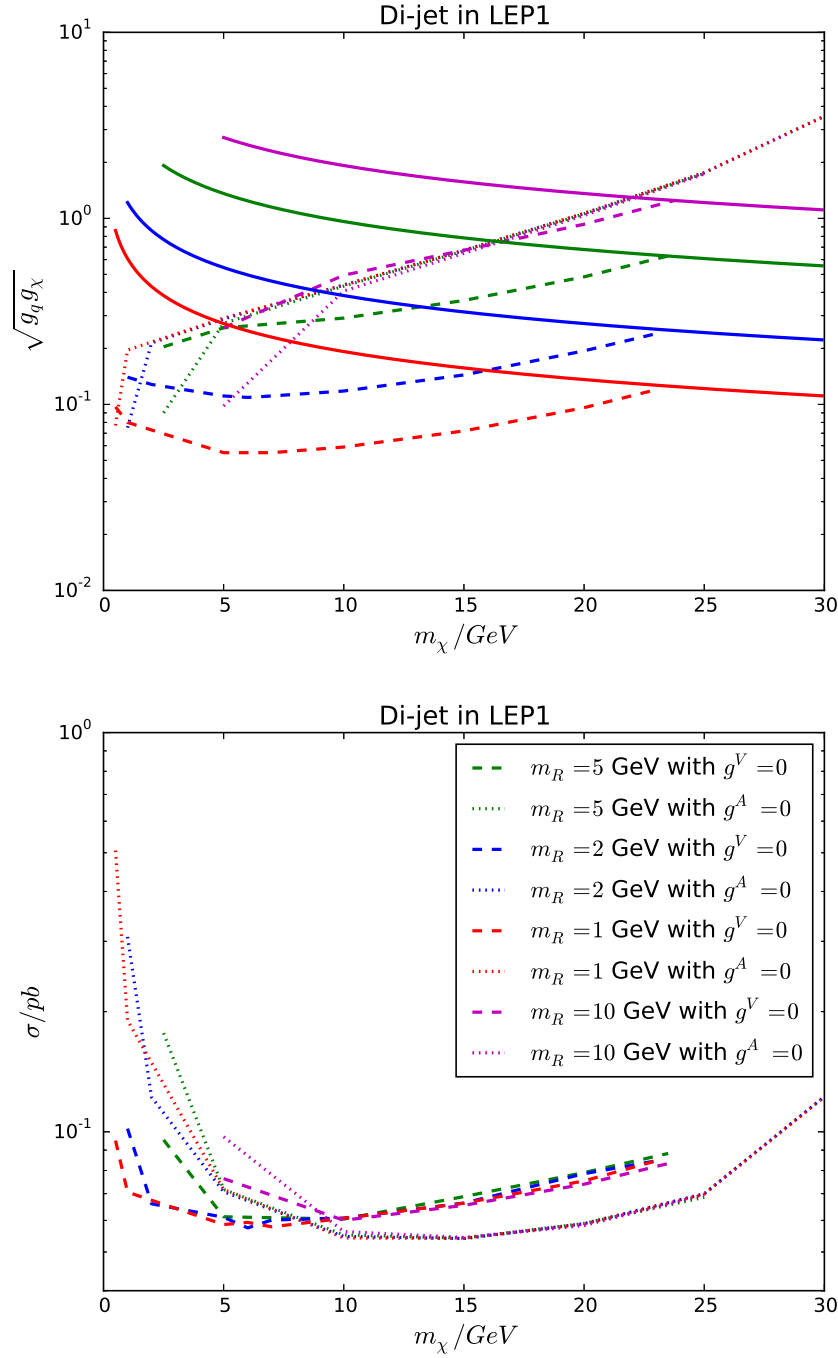


Figure 3.7: The upper frame depicts bounds on couplings of the mediator. The solid lines show the unitarity bound on the axial vector coupling. The other curves depict bounds from our recasting of the ALEPH LEP1 limits. The dotted lines are the upper limits on g^V for $g^A = 0$, while the dashed lines are the upper limits on g^A for $g^V = 0$. The purple, green, blue and red curves are for $m_R = 10, 5, 2$ and 1 GeV, respectively. For $m_\chi > 30$ GeV the bound on g^V is always weaker than the perturbativity condition (3.14). For $m_\chi > 23$ GeV the LEP1 bound on g^A is weaker than the unitarity condition (3.15), and is therefore not shown any more. The lower frame shows the upper bound on the total signal cross section at $\sqrt{s} = 91$ GeV; we use the same conventions as in the upper frame.

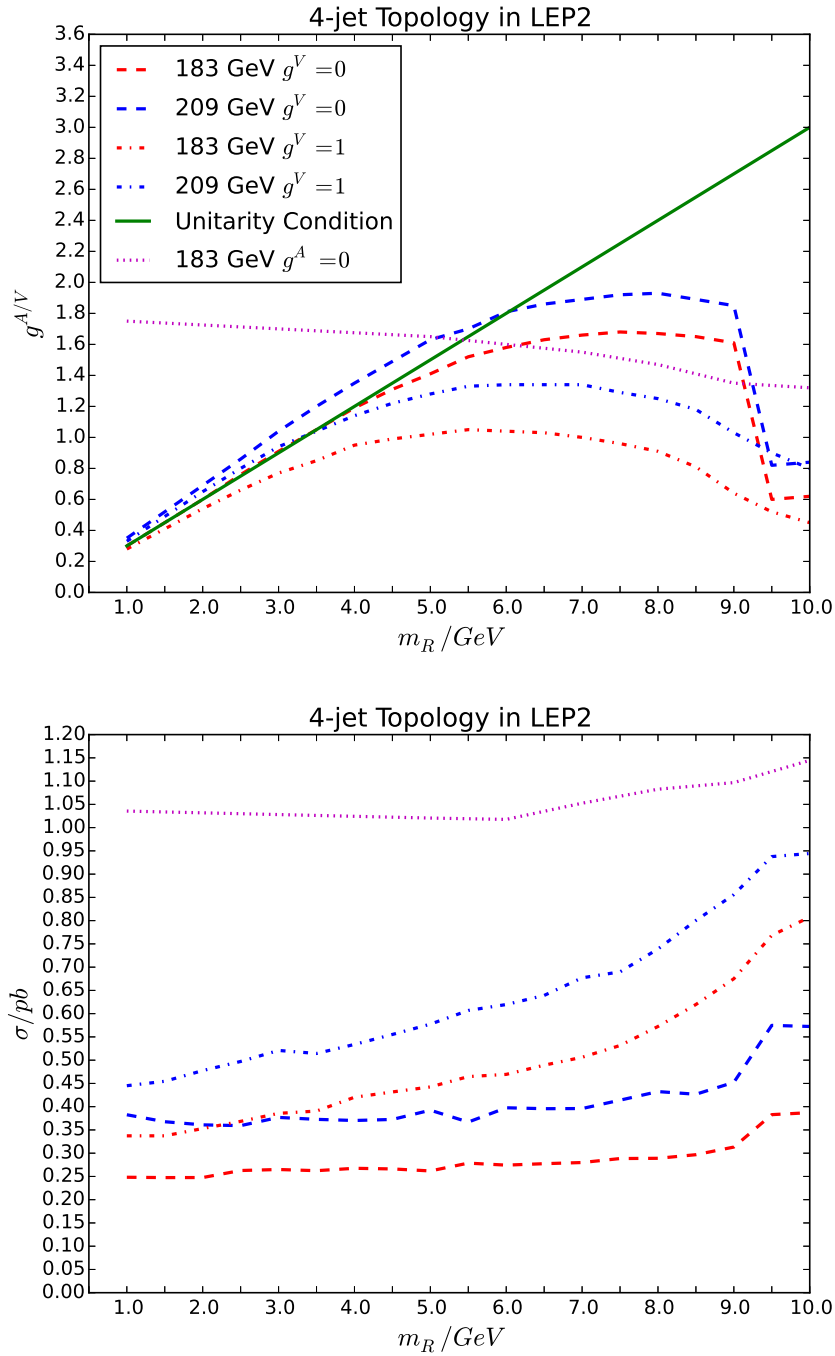


Figure 3.8: Bounds on the (axial) vector coupling to b quarks (upper) and total cross section (lower) we derive from our recasting of the ALEPH Higgs searches in the 4–jet channel. In both frames the lower (red) curves correspond to data taken at $\sqrt{s} = 183$ GeV, while the upper (blue) curves correspond to data taken at $\sqrt{s} = 209$ GeV. The dashed curves have been obtained with vanishing vector couplings, while the dot–dashed curves are for $g_q^V = 1$. The dotted magenta curves show the upper bounds for vanishing axial vector couplings. The solid (green) curve in the upper frame shows the upper bound on g_b^A from the unitarity constraint (3.15) applied to the b quark.

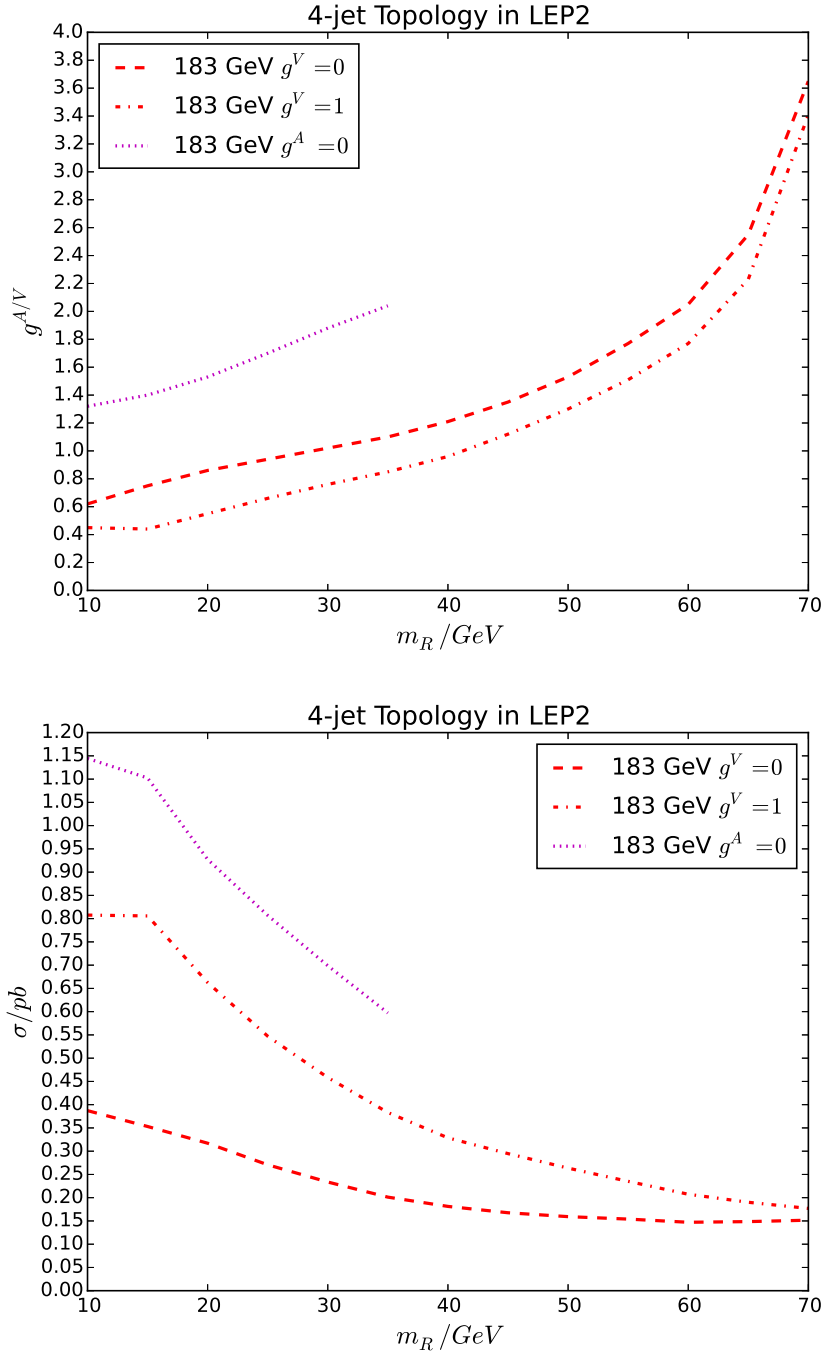


Figure 3.9: Upper bounds on the couplings (upper) and total cross section (lower) from our re-casting of an ALEPH LEP2 4-jet analysis. The notation is as in Fig. 3.8, except that we only show results for the analysis at $\sqrt{s} = 183 \text{ GeV}$ which again has the highest sensitivity. For $g^A = 0$, shown by the dotted curve, the LEP2 bound is only stronger than the perturbativity condition (3.14) if $m_R < 35 \text{ GeV}$. The unitarity bound on g_b^A becomes weaker for higher m_R , and is no longer relevant. However, for $m_R > 70 \text{ GeV}$ the perturbativity condition is stronger than our “experimental” bound, both for $g_q^V = 0$ and for $g_q^V = 1$.

3.5 Conclusions

This chapter derives constraints from published ALEPH searches, based on data taken at the LEP collider some twenty years ago, on a simplified dark matter model. The model features a fermionic dark sector particle (DSP χ) and a spin-1 mediator R which has sizable couplings to some quarks but not to leptons. A complete model may contain additional Higgs bosons to generate m_R and/or additional fermions for anomaly cancellation (see e.g. [154]), but the presence of these particles should not affect our interpretation of LEP data. This kind of simplified model has of course been analyzed previously, in particular in connection with LHC data, which impose severe constraints from “monojet” searches if $m_R > 2m_\chi$, and from searches for di-jet resonances for heavy R . We therefore focus on rather light mediators, $m_R \lesssim 70$ GeV, and always require $m_R < 2m_\chi$ so that on-shell $R \rightarrow \chi\bar{\chi}$ decays are kinematically forbidden. We also impose unitarity and perturbativity constraints on the parameters of the model.

We consider two different final states. The new physics production of two jets plus missing energy and momentum, $jj\cancel{p}$, can only proceed via off-shell R exchange; the signal is thus proportional to the square of the product of the mediator’s coupling to quarks and to the DSP. In contrast, in our model the production of 4-jet final states can occur through real or virtual R exchange, and the signal depends only on the mediator’s coupling to quarks. We used ALEPH data since this experiment published analyses of both of these final states, including complete descriptions of the applied cuts and numbers of surviving SM background events. This allowed us to recast these analyses; although we did not implement detector effects, these are likely to be less important for the signal than for the background (where they can e.g. create missing momentum).

The best bound on the $jj\cancel{p}$ final state from LEP2 data (taken at \sqrt{s} well above the Z mass) comes from squark searches. Somewhat counter-intuitively the resulting bound on the couplings becomes *stronger* for larger m_χ if R is very light and axial vector couplings dominate. This is partly because increasing m_χ increases the cut efficiency, since it increases the kinematical lower bound on the missing energy in the event; however, the main effect is the increase of the contribution from longitudinal R bosons, whose matrix element scales like $g_\chi^A g_b^A m_\chi m_b / m_R^2$. However, even though this is the most promising among several ALEPH searches for this kind of final state, the cut efficiency for our model is rather low, less than 20%. In particular, for vanishing axial vector couplings the bound on the vector coupling is worse than that from perturbativity. In Section 3.4 where therefore devised an optimized set of cuts, which according to our simulation still removes most SM backgrounds, but has significantly higher efficiency for $q\bar{q}\chi\bar{\chi}$ events in our model.

For $m_\chi \lesssim 20$ GeV the best bounds nevertheless come from LEP1 data, taken at $\sqrt{s} \simeq M_Z$, well below the W^+W^- and ZZ production thresholds. We found that an ALEPH analysis looking for $\nu\bar{\nu}H$ final states, where H is the SM Higgs boson which is assumed to decay hadronically, uses cuts that have quite a high efficiency to $q\bar{q}\chi\bar{\chi}$ events in our model. For example, for $m_R = 1$ GeV and $m_\chi \lesssim 20$ GeV it requires $\sqrt{g_b^A g_\chi^A} \leq 0.1$, see Fig. 3.7. However, LEP1 data cannot probe the region $m_\chi \gtrsim 25$ GeV for couplings that respect the unitarity and perturbativity constraints.

Turning to the four jet final state, we found that ALEPH searches for ZH production in the all-hadronic final state have quite a good cut efficiency for $q\bar{q}q'\bar{q}'$ production via real or virtual R exchange in our model. The resulting bound on the coupling of the mediator are roughly comparable to those that follow from $jj\cancel{p}$ final states at LEP2, if the DSP is light and the mediator couples with equal strength to quarks and to the DSP. This search allows to exclude new parts of parameter space

for $m_R \leq 70$ GeV. For somewhat smaller m_R we again expect LEP1 data to be considerably more sensitive, due to the larger signal cross section and reduced background. Unfortunately the only published ALEPH analysis of four jet final states at LEP1 used only about 1% of the total integrated luminosity. This was sufficient to exclude the pair production of new particles with masses up to nearly the beam energy, which was the purpose of this search, but does not allow to improve the limits we derive from LEP2 data.

In all cases we found that the Dirac structure of the couplings (vector or axial vector) affects the bounds significantly. This is partly due to enhanced contributions from longitudinal R exchange, which are proportional to axial vector couplings. Moreover, the cut efficiencies often differ, with pure axial vector couplings usually leading to higher efficiency; the exception is the di-jet plus missing energy search at LEP1, where for $m_\chi > 10$ GeV vector couplings lead to a higher cut efficiency.

In summary, we have shown that LEP data should be able to impose significant new constraints on the parameter space of dark matter models with a leptophobic spin-1 mediator, if the mass of the mediator and/or the dark matter particle are in the (tens of) GeV range and on-shell decays of the mediator into the dark matter particles are forbidden. While a published LEP1 search for di-jet plus missing energy final states already has good efficiency for our model, even the best published analysis of the same final state using LEP2 data has quite a low efficiency. Conversely, the best LEP2 analysis of four jet final states is already quite useful for our purposes, but published LEP1 searches for this final state only use a small fraction of all data. Improved analyses of LEP data therefore hold considerable promise to probe new regions of parameter space of this class of models.

Constraints on Leptophobic Mediator from LHC data

4.1 Overview and Previous Researches

Simplified models of particle dark matter often need a mediator coupling the dark matter particle χ to some particles in the Standard Model (SM). Models where the mediator couples to both quarks and leptons are strongly constrained by LHC searches for $\ell^+\ell^-$ resonances, where ℓ stands for a charged lepton [155–158]. This motivates the investigation of “leptophobic” models, where the mediator does not couple to leptons. In case of a spin-1 mediator R , universal couplings to all quarks are often assumed. If R has a sizable branching ratio into invisible final states, which is generally true if $m_R > 2m_\chi$, the allowed vector and axial vector couplings are then strongly constrained by mono-jet searches [108, 109] unless m_R is well above 1 TeV. For mediator mass between 1 and 2.5 TeV, searches for di-jet resonances [110, 111] perform even better. Additionally, the constraints from spin-dependent and spin-independent interactions in direct detection experiments imposes strong constraints on couplings to first generation quarks [32]; these bounds scale like m_R .

In Chapter 3, which applies LEP data to probe the low m_R region, we therefore switched off all couplings to first generation quarks and axial vector couplings to second generation quarks in order to avoid an excess in direct Dark Matter detection experiments. At tree level, axial vector couplings lead to spin-dependent contributions to the scattering cross section, which also receive a sizable contribution from strange quarks, whereas vector couplings lead to spin-independent contributions which only probe u and d quarks in the nucleon [159]. In our model the scattering on nuclei can therefore only proceed via loop diagrams, and should thus be strongly suppressed.¹ Moreover, the non-zero couplings to other quarks are still available to generate a sizable annihilation rate to explain the observed dark matter relic density through thermal freeze-out. By switching off couplings to first generation quarks, and hence to all valence quarks, we greatly reduce the cross sections for pp scattering processes with an R boson in the intermediate or final state. The published bounds from the LHC experiments, which assume equal couplings of R to all quarks, are therefore no longer valid.

¹ For purely vectorial interaction the effective Rgg vertex should vanish according to Furry’s theorem; one will have to add a second R exchange or a third external gluon in order to obtain a non-vanishing contribution. In case of axial vector interaction the effective Rgg vertex seems to lead to a velocity-suppressed contribution to the cross section, so the dominant contribution probably again comes from yet higher orders.

In this chapter, we want to estimate the LHC constraints on the similar model introduced in Chapter 3. We showed in Chapter 3 that LEP data impose strong constraints only for $m_R < 10$ GeV, and become entirely insensitive for $m_R > 70$ GeV. Here we therefore focus on scenarios with $m_R \geq 10$ GeV. The relevant searches we exploit are similar to those that constrain scenarios with flavor–universal couplings of R : mono–jet + \cancel{E}_T searches, di–jet + \cancel{E}_T searches and di–jet resonance searches. By switching off couplings to light quarks, we increase the branching ratio for $R \rightarrow b\bar{b}$ or $t\bar{t}$ decays. Since in background events most jets originate from light quarks or gluons, b or t tagging can increase the signal to background ratio even for flavor–universal couplings of R , and should be even more helpful in our case.

This chapter is organized as follows. In Sec. 4.2, we briefly describe the Lagrangian of the simplified model containing a leptophobic mediator, which does not couple to first generation quarks. The application to the relevant LHC data is discussed in Sec. 4.3. The LEP result and the tightest unitarity condition from top quark are compared to the LHC exclusion limits we estimate. Finally, Sec. 4.4 contains our summary and conclusions.

4.2 The Simplified Model

4.2.1 Lagrangian and Free Parameters

In the previous chapter, we have already introduced the Lagrangian of the leptophobic mediator without couplings with the first generation quarks. In this chapter, we want to discuss a similar model. Nevertheless, in Chapter 3 we set $g_t^A = g_t^V = 0$ for LEP research, since the total energy of LEP is too limited to probe the top quark. In this chapter, as turing to LHC data, we therefore assume $g_t^V = g_b^V$, $g_t^A = g_b^A$, $g_c^V = g_s^V$, $g_c^A = g_s^A = 0$, and $g_{u,d}^A = g_{u,d}^V = 0$.

This leaves us with seven free parameters: $g_{s,c}^V$, $g_{b,t}^V$, $g_{b,t}^A$, g_χ^A , g_χ^V , m_R and m_χ . However, since R does not couple to leptons, signals involving missing transverse energy \cancel{E}_T require a pair of DSPs in the final state. Since SM Z boson couple to all quarks, final states with an R boson replaced by an invisible decaying Z boson will always contribute to (and indeed often dominate) the background to these signals. Clearly the signal can only compete with this background from on–shell Z bosons if on–shell $R \rightarrow \chi\bar{\chi}$ decays are possible. The relevant quantity is then the branching ratio for these decays, rather than the couplings g_χ^V and g_χ^A separately. Moreover, the DSP mass m_χ also affects the signal only through this branching ratio. This observation implies that replacing the Dirac DSP χ by a complex scalar ϕ is trivial, since again only the branching ratio for $R \rightarrow \phi\bar{\phi}$ decays is relevant in that model.

Turning to quark couplings, we assume all non–vanishing couplings to be equal. In case of axial vector couplings, this can again be motivated by $SU(2)$ invariance. This would still allow different, non–vanishing second and third generation vector couplings, but we set them equal for simplicity. Note that the case $g_s^V = g_c^V = 0$ would give very similar results as the scenario with non–vanishing axial vector couplings. The reason is that contributions to the relevant matrix elements from g_q^V and g_q^A differ only by terms of the order m_q/Q , where Q is the energy scale of the process. Since the parton distribution function for top quarks is still very small at the energies we are interested in, and top tagging turns out to be quite inefficient, the relevant quark is the b quark, and $m_b/Q \ll 1$ for all cases of interest to us. The main difference between vector and axial vector couplings is therefore that in the former case couplings to second generation quarks are included, while these couplings vanish in

the latter case.

Finally we are therefore left with four relevant free parameters: $g_q^V, g_q^A, \text{Br}(R \rightarrow \chi\bar{\chi})$ and m_R . Since the parton distribution functions for second generation quarks in the proton are significantly larger than those for third generation (basically, b) quarks, for fixed size of the non-vanishing couplings we expect much smaller total cross sections for the case $g_q^V = 0, g_q^A \equiv g_q$ than for the case $g_q^A = 0, g_q^V \equiv g_q$. On the other hand, scenarios with $g^V = 0$ should have higher efficiency for b tagging, which is required in some searches.

4.2.2 Perturbativity and Unitarity Conditions

The perturbativity and unitarity conditions are introduced in formula 3.12, 3.14, and 3.15 from Chapter 3. However, due to the assumption of universal axial vector couplings to b and t quarks, now the strongest constraint always comes from the much heavier top, and becomes quite strong for light mediator:

$$g_q^A \leq \sqrt{\frac{\pi}{2}} \frac{m_R}{m_t} = \frac{m_R}{137.59 \text{ GeV}}. \quad (4.1)$$

For example, for $m_R = 10 \text{ GeV}$, g^A should be smaller than 0.08. In contrast, for $m_R > 275 \text{ GeV}$ the unitarity constraint becomes weaker than the perturbativity condition.

4.3 Application to LHC Data

In this section, we recast various LHC searches to constrain the model introduced in section 4.2, including a mono-jet + \cancel{E}_T search [108], multi-jet + \cancel{E}_T searches [160–162], a multi-jet + \cancel{E}_T searches with t tag [163], a multi-jet + \cancel{E}_T search with double b tag [164], and di-jet resonance searches with final state b -jets [165] or t -jets [166].

In order to simulate the events and recast the analysis, we use FeynRules [97] to encode the model and generate an UFO file [129] for the simulator, MadGraph [98] to generate the parton level events, PYTHIA 8 [99] for QCD showering and hadronization, DELPHES [100] to simulate the ATLAS and CMS detectors, and CheckMATE [101, 167] to reconstruct and b -tag jets, to calculate kinematic variables, and to apply cuts. We note that the toolkit CheckMATE uses a number of additional tools for phenomenology research [168–178].

Let us first discuss final states involving missing E_T . These are often categorized as “mono-jet + \cancel{E}_T ” and “multi-jet + \cancel{E}_T ” final states. However, the “mono-jet” searches also allow the presence of at least one additional jet. On the other hand, “multi-jet” searches do indeed require at least two jets in the final state. These signals thus overlap, but are not identical to each other.

As remarked in section 4.2, missing E_T in signal events always comes from invisibly decaying mediators, $R \rightarrow \chi\bar{\chi}$. Since multi-jet searches require at least two jets in the final state, we use MadGraph to generate parton-level events with a $\chi\bar{\chi}$ pair plus one or two partons (quarks or gluons) in the final state. The former process only gets contributions from the left diagram in fig. 4.1 plus its crossed versions, including the contribution from $gq \rightarrow Rq$. Note that R has to couple to the initial quark line in this case. We use parton distribution functions (PDFs) with five massless flavors; the mass of the corresponding quarks should be set to 0 in order to avoid the inconsistency with massless evolution equations (DGLAP equations). The b -quark PDF is nonzero, but it is still considerably smaller than those of first generation quarks. The contribution from this diagram, which is formally

of leading order in α_S , is therefore quite small, especially for scenarios with $g_q^V = 0$ where R only couples to third generation quarks.

If we allow the final state to contain two partons in addition to the DSPs, there are contributions with only light quarks or gluons in the initial state; an example is shown in the middle of fig. 4.1, but there are several others. These diagrams are higher order in α_S , but they receive contributions from initial states with much larger PDFs than those contributing to the first diagram. It is thus not clear a priori which of these contributions will be dominant for a given set of cuts.

There is one additional complication. At the parton level, events with one and two partons in the final state are clearly distinct. However, once we include QCD showering, which is handled automatically by PYTHIA, the distinction becomes less clear. In particular, a single parton event with an additional gluon from showering can no longer be distinguished from a certain two parton event without additional gluon. Naively adding contributions with one and two partons in the final state before showering can therefore lead to double counting. Similarly, if one of the final-state quarks shown in the middle diagram of fig. 4.1 has small p_T , the diagram can be approximated by $g \rightarrow q\bar{q}$ splitting followed by $gq \rightarrow Rq$ production. This contribution is already contained in the crossed version of the left diagram of fig. 4.1, via the scale-dependent PDF of q , so simply adding these diagrams again leads to double counting. MadGraph avoids both kinds of double counting by using the ‘‘MLM matching’’ algorithm [179]. Of course, showering can add more than one additional parton; indeed, we find significant rates for final states with up to four jets (having transverse energy $E_T \geq 35$ GeV each).

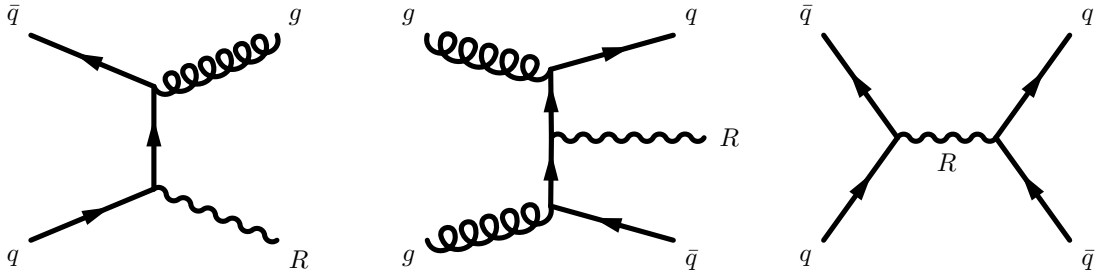


Figure 4.1: Examples of Feynman diagrams contributing to mono-jet + \cancel{E}_T (left), di-jet + \cancel{E}_T (center) and di-jet resonance (right) final states; in the former two cases it is assumed that the mediator R decays into two dark sector particles, which escape detection, whereas in the latter case R is assumed to decay into a quark antiquark pair. The diagram to the right is unique (with different initial states contributing), and the one on the left is unique up to crossing; however, many additional diagrams, with different combinations of partons in the initial and final states and different propagators, contribute to R +di-jet production.

Searches for final states leading to large missing E_T are typical cut-and-count analyses, where the final state is defined by cuts on the type and number of final state objects (in particular, leptons and jets with or without b -tag) and on kinematic quantities (in particular, the transverse momenta or energies of the jets and the missing E_T). The experiments themselves designed these cuts, and estimated the expected number of surviving SM background events. The comparison with the actually observed number of events after cuts then allows to derive upper bounds on the number of possible signal events. We pass our simulated signal events through CheckMATE, which applies the same cuts (including detector resolution effects), and compares the results with the upper bounds obtained by the experiments.

The second kind of search we consider are searches for di-jet resonances. The leading-order signal diagram is shown on the right in fig. 4.1. In this case the final state contains no partons besides the mediator R ; for $g_q^V = 0$, only $b\bar{b}$ initial states contribute, whereas for non-vanishing vector couplings also $s\bar{s}$ and $c\bar{c}$ initial states contribute. Of course, the left and middle diagrams shown in fig. 4.1 also contribute to this signal if R decays into a $q\bar{q}$ pair. However, in this case one has to add two powers of α_S in order to access initial states including only light quarks or gluons. Moreover, if all final state transverse momenta are small, which maximizes the cross section, the contribution from the middle diagram is actually already included in the right diagram, via double $g \rightarrow q\bar{q}$ splitting. The left and middle diagrams should therefore only be included in inclusive R production when a full NLO or even NNLO calculation is performed, which is beyond the scope of this chapter.

Note also that resonance searches are not cut-and-count analyses. The analyses still use a set of basic acceptance cuts, in this case on the (pseudo-)rapidities and transverse momenta of the two leading jets. The bound on resonance production is then obtained by fitting a smooth function to the di-jet invariance mass distribution, which is assumed to be dominated by backgrounds, and computing the limit on a possible additional contribution peaked at a certain value (basically, the mass of the resonance). The current version of CheckMATE does not include comparison with this kind of searches. However, CheckMATE does allow to estimate the efficiency with which our signal events pass the acceptance cuts. This allows to derive the constraints from resonance searches on our model, as follows.

The most sensitive di-jet resonance search we found is that of ref. [165], which requires a double b -tag in the final state. This paper presents the resulting upper bounds for a couple of models. One of them is quite similar to ours, but assumes universal couplings to all quarks; this leads to a greatly enhanced resonance production cross section, and a somewhat reduced branching ratio into $b\bar{b}$ pairs, compared to our model. The paper also gives the cut efficiency for the model with universal couplings. We, therefore, recast their cuts and compare the cut efficiencies of their model and our models in order to estimate the bound for our model through the following rescaling:

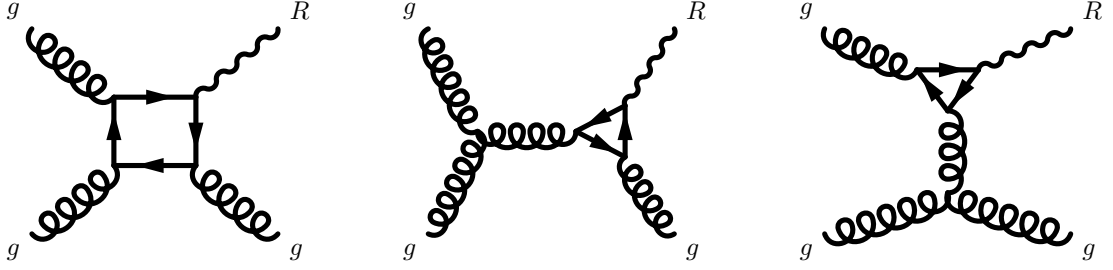
$$\sigma_{\max, \text{ours}} = \sigma_{\max, \text{exp}} \cdot \frac{\epsilon_{\text{exp}}}{\epsilon_{\text{ours}}}. \quad (4.2)$$

Here $\sigma_{\max, \text{ours}}$ is the largest allowed cross section for our model, $\sigma_{\max, \text{exp}}$ is the largest allowed cross section in the original experimental analysis, ϵ_{exp} is the selection efficiency of the model in the paper, and ϵ_{ours} is the selection efficiency of our model.

Finally, we cannot easily reproduce the top tagging required in the di-top resonance search [166]. However, even if we assume 100% efficiency for the di-top tag, the resulting bound is much weaker than our recast of [165] described in the previous paragraphs. We therefore do not show this bound in our summary plot.

The results of our analyses are summarized in fig. 4.3. The thin solid lines in the top-left corner show the bounds we derived in Chapter 3 from analyses of older ALEPH searches for four jet final states at the e^+e^- collider LEP; note that these bounds are valid for $m_R < 2m_\chi$. The solid straight line is the unitarity bound (4.1) applied to the top mass; recall that it applies only to axial vector couplings. (Since top quarks could not be produced at the LEP collider, in Chapter 3 we only considered the unitarity constraints involving m_b and m_χ .)

The other results shown in fig. 4.3 are new. The dashed curves show the bounds on the square of the coupling of R to quarks times the branching ratio for invisible R decays which we derived from the


 Figure 4.2: Loop diagrams contributing to R +jet production from gluon fusion.

most sensitive jet(s) plus missing E_T searches, for pure axial vector couplings (red, upper curve) and pure vector couplings (green, lower curve); the lower frame shows the corresponding bounds on the signal cross section, defined as the total cross section for the on-shell production of a mediator R times the invisible branching ratio of R . It is important to note that these constraints are only significant in our model if on-shell $R \rightarrow \chi\bar{\chi}$ decays are allowed, i.e. they constrain a region of parameter space that is complementary to that analyzed in Chapter 3.

The dot-dashed curves in the upper frame show the bounds on the square of the coupling of R to quarks times the branching ratio for $R \rightarrow q\bar{q}$ decays that result from searches for di-jet resonances, again separately for pure axial vector couplings (purple, upper curve) and pure vector couplings (blue, lower curve). The relevant analysis by the ATLAS collaboration [165] is sensitive only to $m_R \geq 600$ GeV.

The difference between the constraints on vector and axial vector couplings is almost entirely due to the additional coupling to s and c quarks that we allow only for the former, as discussed in Sec. 4.2.1. In particular, we see that the constraint from the $b\bar{b}$ resonance search is much stronger for the model with vector couplings.

In the upper frame of Fig. 4.3 the curves depicting the bounds from searches for final states containing \cancel{E}_T evidently lie below the ones showing bounds from di-jet resonance searches, except for the scenario with pure vector coupling at $m_R \simeq 2$ TeV. However, this is somewhat misleading, since the dashed curves show bounds on $g_q^2 \cdot \text{Br}(R \rightarrow \chi\bar{\chi})$, while the dot-dashed curves shows bounds on $g_q^2 \cdot [1 - \text{Br}(R \rightarrow \chi\bar{\chi})]$. For $m_R \geq 1$ TeV the two sets of constraints on the coupling are actually comparable if $\text{Br}(R \rightarrow \chi\bar{\chi}) \simeq 0.3$ (0.1), for pure vector (axial vector) coupling; for even smaller invisible branching ratio of R , the $b\bar{b}$ resonance search imposes the stronger constraint in this large m_R region. We note that for $m_R^2 \gg m_t^2$ and $g_\chi = g_q$, i.e. equal coupling of the mediator to the DSP and to heavy quarks, the invisible branching ratio of R is below 1/7 (1/13) for pure axial vector (vector) coupling, the difference being due to the different number of accessible $q\bar{q}$ final states.

Within the missing E_T searches the best bound on g_q^V for $m_R < 1.4$ TeV is from ref.[164], a double b tagged multi-jet + \cancel{E}_T analysis, while ref.[160], a general multi-jet + \cancel{E}_T analysis, is the most sensitive one for $m_R \geq 1.4$ TeV; this change of the most sensitive analysis explains the structure in the dark green curves at that m_R , which is most visible in the lower frame. In contrast, the strongest bound on g_q^A is always from ref.[164] with double b tag, which also determines the bound on the vector coupling for $m_R < 1.4$ TeV. This explains why the bound on the coupling is actually very similar in both cases: the required double b tag means that the contribution from partonic events containing only s or c quarks, which only exists in the case of vector coupling, has very small efficiency, since the b

tag requirement can only be satisfied through mistagging, or through additional b quarks produced in hard showering. As a result the bound on the *total* cross section, shown in the lower frame, is much weaker for pure vector coupling, since the coupling to s and c quarks greatly increases the total cross section while contributing little to the most sensitive signal.

We also consider multi-jet analyses specially designed for final states containing two top quarks [161, 163]. However, the top-tag in [163] is not easy to recast directly. We therefore, assume 100% efficiency to reach the most ideal bound. Unfortunately, even this ideal bound on g^2 is 10 times weaker than that from the analysis which only requires a double b -tag. One reason is that both $b\bar{b}$ and $t\bar{t}$ final states may lead to b -tagged jets, while the selection rules specially designed for top jets exclude the $b\bar{b}$ final state. Moreover, for our assumption of equal couplings the cross section for $t\bar{t}R$ production is considerably smaller than that for $b\bar{b}R$ production.

As noted above, we also derived constraints on our model from mono-jet searches. The most sensitive analysis has been published in [108], and does not require any flavor tagging. The resulting constraint on the vector coupling is only slightly weaker than that shown in Fig. 4.3, while the constraint on the axial vector coupling is not competitive. Since no flavor tagging is required, the large contribution from s or c quarks in the initial and final states has similar efficiency as contributions with b quarks, and greatly strengthens the limit on the vector coupling.

Before concluding this section, we comment on loop processes that allow gg initial states to contribute to our signals. The relevant Feynman diagrams are shown in Fig. 4.2. They involve two additional QCD vertices relative to the leading-order R +jet production channels, i.e. they are formally NNLO. Nevertheless the large gluon flux in the proton might lead to sizable contributions. We again use FeynRules and Madgraph to simulate these events at the parton level.

Note that the tree-level contributions we discussed so far are only sensitive to the absolute value of the couplings of the mediator to quarks. In contrast, in the loop diagrams all quark flavors contribute coherently, so the relative signs between different $Rq\bar{q}$ couplings are important.

Let us first consider pure vector couplings. Here our simplified model as written is well-behaved also at QCD one-loop level. We find that the loop contributions of Fig. 4.2 only contribute at most 2% of the leading-order mono-jet signal if all g_q^V are set equal; this contribution is reduced by another factor of 5 if we instead take $g_{s/b}^V = -g_{c/t}^V$. In particular, there is no enhancement for small m_R ; instead, the cross section after cuts approaches a constant once $m_R \ll p_{T,\text{cut}}$. Recall also that in this case there are tree-level contributions involving the strange quark content of the proton, which is much larger than that of b quarks (although still considerably smaller than that of gluons). We can thus always safely neglect these loop contributions for non-zero vector couplings.

In contrast, in case of non-vanishing axial vector couplings our model with equal couplings of the mediator to all heavy quarks leads to a ggR anomaly, i.e. this version of our simplified model is not well-behaved at the 1-loop level. We therefore took $g_b^A = -g_t^A$ in order to cancel this anomaly.

Moreover, the loop amplitude now receives a contribution that scales $\propto 1/m_R$. As a result, for $m_R = 10$ GeV the loop contribution to the mono-jet cross section exceeds the tree-level contribution by about a factor of 20. We find that nevertheless the best bound still comes from the final state with two b -jets and missing E_T . Recall that here gg initial states are accessible already at tree-level. Since in the loop diagrams the external gluon has to be virtual, so that it can split into a $b\bar{b}$ pair, the loop contribution is still NNLO relative to this tree-level contribution. Nevertheless the $1/m_R$ enhancement, which is associated with heavy (i.e. top) quark loops, means that including the loop diagram with $g_b^A = -g_t^A$ would tighten the upper limit on the squared coupling shown in Fig. 4.3 at

$m_R = 10$ by about 40%. For $m_R = 50$ GeV, however, the loop contribution only doubles the total mono-jet signal, and the final bound on the squared coupling from the di- b final state is improved by about 3%.

It should be clear that setting $g_b^A = -g_t^A$ is only one solution to cancel the anomaly. Another possibility is to introduce a very heavy quark Q satisfying $g_Q^A = -2g_b^A = -2g_t^A$. This would lead to even larger loop contributions for small m_R ; however, the unitarity bound (4.1) would then also have to be applied to m_Q , and might even supersede the LHC constraint.

In sum, we conclude that for axial vector couplings loop corrections involving two-gluon initial states might moderately strengthen the LHC constraint for $m_R < 50$ GeV, the exact result depending on the UV completion of the model. Note also that this source of loop corrections adds incoherently to the signal, i.e. it cannot weaken the bounds presented in Fig. 4.3. We therefore believe that this Figure, which is independent of the UV completion, is a better representation of the LHC constraints on our model.

4.4 Conclusions

In this chapter, we discuss a model containing a Dirac fermion χ as dark matter candidate as well as a spin-1 mediator R . We assume that R has vanishing couplings to first generation quarks and vanishing axial vector coupling to second generation quarks, thereby easily satisfying constraints from direct dark matter searches. By assuming vanishing couplings to leptons the otherwise most sensitive LHC searches, based on analyses of $\ell^+\ell^-$ final states where ℓ stands for a charged lepton, are evaded as well. Due to the vanishing couplings to light quarks, and hence to all valence quarks in the proton, the R production rate at the LHC is considerably smaller than for the more commonly considered scenarios with (essentially) universal couplings to all quarks.

Nevertheless LHC data impose quite strong constraints on the model if the branching ratio for invisible R decays is sizable, which requires $m_R > 2m_\chi$. The best LHC bound then always comes from searches for final states containing jets plus missing E_T . Our CheckMATE-based recast of these analyses leads to an upper bound on the product of the squared coupling and the invisible branching ratio of R of 10^{-3} for $m_R \leq 200$ GeV. This weakens to 0.01 (1) for $m_R = 600$ GeV (2 TeV), see Fig. 4.3. Searches for invisibly decaying mediators have traditionally been framed as “mono-jet” searches (which allow additional jets in the final state, as mentioned above), and have been interpreted assuming equal (vector or axial vector) couplings to all quarks [108, 109]. For pure axial vector couplings these bounds are actually weaker than ours if $m_R \leq 600$ GeV. Since the signal need only contain a single hard jet, and no b -tagging is used, one needs a very strong cut on the missing E_T to suppress the background; for $m_R \lesssim 1$ TeV this leads to a much worse cut efficiency than the most sensitive analysis we use, which requires two tagged b -jets plus missing E_T . For $m_R \lesssim 600$ GeV this search may thus also impose tighter bounds on the model with universal couplings. Nevertheless the bound on g_q^2 times the invisible branching ratio from mono-jet searches in the model with universal coupling becomes significantly stronger than ours for larger m_R , by about one order of magnitude for $m_R = 1.5$ TeV.

For $m_R \geq 0.6$ TeV roughly comparable bounds on the product of the squared coupling and the branching ratio of R into $q\bar{q}$ quarks can be derived from an ATLAS search for $b\bar{b}$ resonances. Searches for generic di-jet or $t\bar{t}$ resonances yield much weaker constraints on our model. Generic di-jet resonance searches at the 13 TeV LHC become sensitive only at a resonance mass above 1.5 TeV or so. The resulting bounds on mediators with unsuppressed couplings to valence quarks are quite strong.

For example, for $m_R = 1.5$ TeV the ATLAS analysis [111] gives a bound on the squared universal coupling to quarks in a leptophobic model that is about two orders of magnitude stronger than our bound from $b\bar{b}$ resonant searches in the model with vector couplings, which in turn is a factor of about 3 stronger than the analogous bound in the model with axial vector couplings.

We thus see that both in the missing E_T and in the resonance searches switching off the couplings to first generation quarks greatly weakens the limits on the couplings for $m_R > 1$ TeV, less so for smaller mediator masses.

Since the energy scale of these reactions (e.g. the missing E_T , or m_R in the resonance searches) is much larger than the masses of the relevant quarks, the matrix elements for vector and axial vector couplings are almost the same. Unless $m_R \gg m_\chi$ for equal coupling strengths the branching ratio for invisible $R \rightarrow \chi\bar{\chi}$ decays will be larger for pure vector coupling than for pure axial vector coupling; however, this effect is absorbed by interpreting the relevant constraints as upper bounds on the product of the squared coupling times the invisible branching ratio, as we did in the above discussion.

LHC searches lose sensitivity to our model if $m_R > 2$ TeV, or if $m_R < 0.6$ TeV and $m_R < 2m_\chi$. Probing significantly higher values of m_R would require higher center-of-mass energies; since all relevant searches are background-limited, increasing the luminosity will increase the reach only slowly. If on-shell $R \rightarrow \chi\bar{\chi}$ decays are not possible, missing E_T searches at the LHC are essentially hopeless in our model. The reason is that in this case a signal which is of second order in the couplings of the mediator has to compete with SM signals that are first order in electroweak couplings, in particular the production of Z and W bosons which decay into neutrinos.¹ For $m_R < 70$ GeV the old LEP experiments have some sensitivity, but the resulting bound is not very strong in Chapter 3. Straightforward di-jet resonance searches at the LHC are not possible for m_R much below 0.6 TeV, since the trigger rate would be too high. One might consider previous hadron colliders, in particular the Tevatron. However, these earlier colliders were $p\bar{p}$ colliders, where the $b\bar{b}$ background includes contributions where both initial-state quarks are valence quarks; recall that in our model the signal does not receive contributions from such initial states.

A probably more promising approach is to consider final states containing an additional hard “tagging jet” besides the mediator R . Both ATLAS [180] and CMS [181] have presented bounds on rather light di-jet resonances using this trick, which is also employed in the “mono-jet” searches. Unfortunately these searches are currently not easy to recast, since they use “fat jet” substructure techniques. In any case, in order to gain sensitivity to our model this technique would probably have to be combined with b -tagging, which proved crucial for deriving useful constraints from di-jet resonance searches at $m_R > 600$ GeV. An analysis of this kind should be able to probe deep into the parameter space with $m_R < 600$ GeV and $m_R < 2m_\chi$.

¹ In case of universal couplings to all quarks the “mono-jet” analyses [108, 109] do exclude a small region of parameter space with $m_R/2 < m_\chi \lesssim 200$ GeV for a vector mediator, but not for an axial vector mediator.

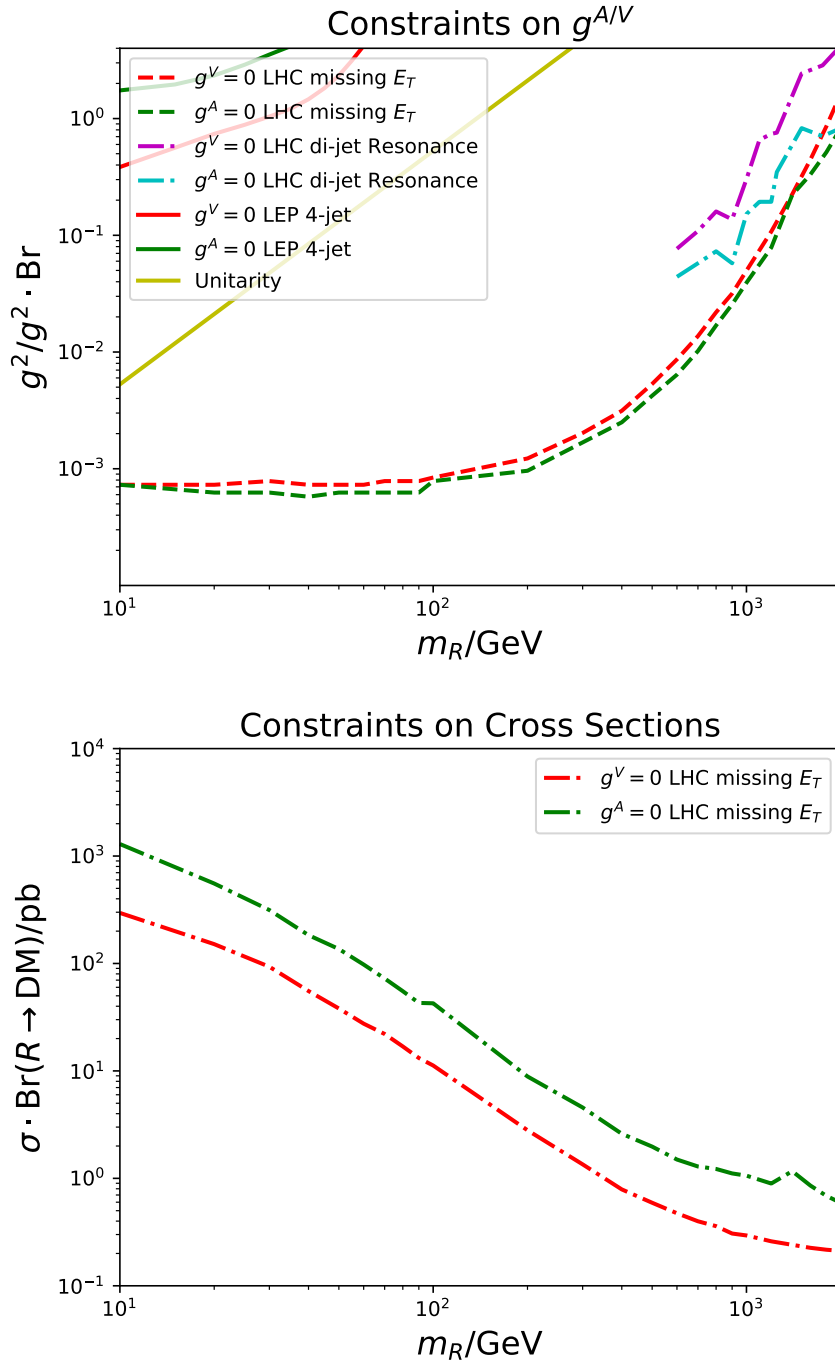


Figure 4.3: The upper frame shows the bound on the squared coupling of the mediator to quarks times the relevant branching ratio of the mediator that we derive by recasting various LHC bounds (dashed and dot-dashed curves). The lower solid curve shows the unitarity bound (4.1) on the axial vector coupling, and the thin solid lines in the top-left corner show constraints from recast LEP constraints in Chapter 3 based on analyses by the ALEPH collaboration. For $g^A = 0$ only vector couplings g_q^V are allowed with $q = s, c, b, t$, while for $g^V = 0$ only axial vector couplings g_q^A are allowed with $q = b, t$. LHC missing E_T results are from the combination of mono-jet and multi-jet analyses. The lower frame shows the upper bound on the total cross sections from the missing E_T analyses.

Part III

The 3rd Part: Leptophilic Mediator

Constraints on Leptophilic Mediator from LHC data

5.1 Overview and Previous Researches

In the previous chapters of Part II, we discuss the leptophobic mediator, which relates to final state without hard leptons. Another kind of signatures at collider is final states with hard leptons. Unlike the parton level process with only quarks in the final state, which hardly have very energetic leptons finally after hadronization, the final state τ may decay hadronically to form a jet that can be tagged as τ_h besides leptons. Additionally, the soft jets after jet reconstruction in the final state is relatively energetic compared to soft leptons, and hence is hard to be excluded by simple cuts as well. Therefore, the leptonic final state is not quite simpler than the quark case. The hadronization, jet reconstruction and tagging are still challenging and significant. We use the signatures with hard leptons to analyze the leptophilic mediator in this chapter.

There are several reasons for considering the extension of the gauge group of the Standard Model (SM) by another Abelian $U(1)$ factor. It is usually assumed that the new gauge boson couples universally to all three generations of quarks, in order to avoid constraints from flavor-changing neutral currents. If we further insist that the gauge group should be anomaly-free within the SM matter content (possibly extended by right-handed neutrinos, but without other exotic chiral fermions), there are only four different possibilities. These can be written as $B - L$ [182], as well as the purely leptonic $L_e - L_\mu$, $L_\mu - L_\tau$, and $L_e - L_\tau$ [183]; of course, linear combinations of these four groups are also possible. In the $U(1)_{B-L}$ model, which does require right-handed neutrinos, the new gauge boson couples to both quarks and (charged) leptons. This model is therefore tightly constrained by searches for di-lepton resonances at hadron colliders, in particular at the LHC [156, 158]; if the coupling of the new $U(1)$ is comparable to that of the $U(1)_Y$ of the SM, these searches exclude Z' masses below several TeV.¹

In the other three models the cancellations of anomalies occur between different generations without the requirements of extra fermions [183]. LEP data strongly constrain the $L_e - L_\mu$ and $L_e - L_\tau$ models. While we are not aware of dedicated analyses of LEP data in the framework of these models, for $m_{Z'} > 300$ GeV or so the Z' propagator at LEP energies ($\sqrt{s} \leq 209$ GeV) can be approximated by a constant, in which case limits on contact interactions apply. In particular, ALEPH data on

¹ See ref.[184] for a very recent assessment on current constraints on the $B - L$ model.

$e^+e^- \rightarrow \mu^+\mu^-$ [185] imply $m_{Z'}/g_{e\mu} > 1.1$ TeV for the $L_e - L_\mu$ model, whereas OPAL data on $e^+e^- \rightarrow \tau^+\tau^-$ [186] lead to the bound $m_{Z'}/g_{e\tau} > 0.94$ TeV for the $L_e - L_\tau$ model. For smaller Z' masses, where propagator effects become important, the bound will be even stronger.

In contrast, the $L_\mu - L_\tau$ model does not predict any new interaction for the electron. Its gauge boson can therefore only be produced through higher-order processes in e^+e^- collisions, by emission off a charged or neutral lepton of the second or third generation. These final states can also be produced at the LHC [187], which has accumulated a far larger number of di-muon and di-tau events than LEP did. In this chapter we therefore focus on LHC data. Note also that the $U(1)_{L_\mu - L_\tau}$ model can accommodate successful neutrino masses even with the simplest Higgs sector [188, 189], and can be extended to contain a dark matter particle that is charged under the new symmetry but easily satisfies the stringent direct search constraints [190, 191]. In principle, this model could also explain the difference between SM prediction and measurement of the anomalous magnetic moment of the muon ($a_\mu - 2$); however, bounds on $\nu_\mu N \rightarrow \nu_\mu \mu^+ \mu^- N$ “trident” production [192], where N stands for some nucleus, exclude this possibility for $m_{Z'} > 0.5$ GeV.

The other existing constraint in the Z' mass range relevant for searches at the LHC comes from analyses of Z decays into four charged leptons [193]. In particular, ref.[194] is a CMS analysis constraining this model using $Z \rightarrow 4\mu$ decays. This search is obviously only sensitive to relatively light Z' , $m_{Z'} < m_Z$. LHC prospects for this model have been discussed previously [195–197], with ref. [197] focussing on the case $m_{Z'} \leq m_Z/2$; however, these papers did not attempt to use actual LHC data to constrain the model.

In contrast, we consider a comprehensive set of LHC analyses for final states with two, three or four charged leptons in the final state, where a lepton l for us means a muon or a hadronically decaying τ . Final states with fewer than four charged leptons are also required to contain some missing transverse momentum $E_{\cancel{T}}$. In particular, final states with only two charged leptons plus $E_{\cancel{T}}$ are sensitive to Z' decays into dark matter particles, which also reduce the branching ratios for Z' decays into μ or τ pairs. $\tau \rightarrow \mu$ decays contribute to muonic final states, if typically with reduced efficiency since the muon produced in τ decays is obviously softer than the parent τ . In principle, $\tau \rightarrow e$ decays can also populate final states with electrons. However, the small branching ratio (about 18%) and again reduced efficiency imply that final states with electrons will not be as sensitive as those only containing muons or hadronically decaying τ leptons. We use the CheckMATE framework [101, 167]. Only a few of the analyses we applied had already been included in CheckMATE. We included a total of 281 new signal regions defined in 28 different papers.² We find that the specialized Z' search [194] based on 4μ final states is indeed most sensitive for $10 \text{ GeV} \leq m_{Z'} \leq 60 \text{ GeV}$; for larger masses, analyses of final states containing only three charged leptons are more sensitive.

The full $SU(3)_c \times SU(2)_L \times U(1)_Y \times U(1)_{L_\mu - L_\tau}$ model introduced in [190, 191] contains not only the new mediator and DM particle, but also an extra Higgs boson to break the new $U(1)$ as well as SM singlet right-handed neutrinos for a see-saw generation of realistic neutrino masses. The extra Higgs boson plays a significant role in the dark matter phenomenology, but it can contribute to the final states we consider only if its mixing angle with the $SU(2)$ doublet Higgs boson responsible for electroweak symmetry breaking is relatively large. We ignore this possible source of additional signal events. The main free parameters are thus the mass of the Z' and the strength of its coupling to μ and

² Most of the experimental papers we used also include signal regions containing electrons. We did not consider those, for the reasons explained above. By current policy an analysis can become part of the official CheckMATE release only if *all* of the signal regions defined in this analysis are encoded. Our “private” version of CheckMATE is available upon request.

τ leptons; the branching ratio for Z' decays into dark matter particles also plays a (lesser) role.

The remainder of this chapter is organized as follows. In Sec. 5.2, we briefly describe the parts of the $U(1)_{L_\mu-L_\tau}$ model [190, 191] that are relevant for the LHC searches we consider. The application to LHC data is discussed in Sec. 3, both for vanishing and non-vanishing branching ratio for Z' decays into dark matter particles. Finally, Sec. 5.4 contains our summary and conclusions.

5.2 The Simplified Model

The $SU(3)_c \times SU(2)_L \times U(1)_Y \times U(1)_{L_\mu-L_\tau}$ model contains a new gauge boson Z' for the local $U(1)_{L_\mu-L_\tau}$ symmetry; the corresponding field strength tensor is $Z'_{\mu\nu} \equiv \partial_\mu Z'_\nu - \partial_\nu Z'_\mu$. As usual, we write its interaction with other particles using the covariant derivative instead of the normal partial derivative, i.e. $\partial_\mu \rightarrow D_\mu = \partial_\mu - ig_{\mu\tau} q Z'_\mu$, where $g_{\mu\tau}$ is the new gauge coupling and q is the $L_\mu - L_\tau$ charge of the particle in question. The model also contains a complex scalar ϕ_{DM} , which is singlet under the gauge group of the SM but carries $L_\mu - L_\tau$ charge q_{DM} . The kinetic term of the new gauge boson is written with strength tensor $\mathcal{L}_{Z'} = -\frac{1}{4} Z'_{\mu\nu} Z'^{\mu\nu}$, while the kinetic term of DM particle is $(D^\mu \phi)^* D_\mu \phi$. If we need a massive gauge boson for $U(1)_{L_\mu-L_\tau}$, the original gauge field should eat a Goldstone boson through Higgs mechanism. Therefore, a new Higgs field with non-zero $U(1)_{L_\mu-L_\tau}$ charge should be added to the new model. If we assume the new Higgs field named as ϕ_H and the SM Higgs field named as ϕ_h , the additional terms related to ϕ_H are

$$\mathcal{L}_H = (D_\mu \phi_H)^* (D^\mu \phi_H) - V(\phi_h, \phi_H), \quad (5.1)$$

$$V(\phi_h, \phi_H) \equiv \mu_H^2 \phi_H^* \phi_H + \lambda_H (\phi_H^* \phi_H)^2 + \lambda_{hH} (\phi_h^\dagger \phi_h) (\phi_H^* \phi_H). \quad (5.2)$$

In the expression, $D_\mu = \partial_\mu - ig_{\mu\tau} Z'_\mu$, we assume the new Higgs field has the same charge with muon. Because of the existence of λ_{hH} , the mass matrix of 2 neutral Higgs particle is not diagonal, and hence they mix with each other to form the mass eigenstates h_1 and h_2 , where the mass of h_1 should equal to SM Higgs in experiments. Therefore, the DM particle may acquire mass from both sides. Normally, we can assume either spinor or scalar DM, and in this chapter, unlikely previous chapters, we consider complex scalar DM in the following sections. The spinor DM couples to Higgs bosons only through Yukawa terms. On the other hand, the scalar DM may have more flexible couplings. In the most general case, the Lagrangian for DM field is

$$\begin{aligned} \mathcal{L}_{DM} = & (D_\mu \phi_{DM})^* (D^\mu \phi_{DM}) - \mu_{DM}^2 \phi_{DM}^* \phi_{DM} - \lambda_{DM} (\phi_{DM}^* \phi_{DM})^2 \\ & - \lambda_{Dh} (\phi_{DM}^* \phi_{DM}) (\phi_h^\dagger \phi_h) - \lambda_{DH} (\phi_{DM}^* \phi_{DM}) (\phi_H^* \phi_H), \quad D_\mu = \partial_\mu - iq_{\mu\tau} g_{\mu\tau} Z'_\mu. \end{aligned} \quad (5.3)$$

Therefore, after the symmetry spontaneous breaking ($SU(2)_L \times U(1)_Y \times U(1)_{L_\mu-L_\tau}$ to $U(1)_{EM}$), the expressions of ϕ_h and ϕ_H in the unitary gauge are

$$\phi_h = \begin{pmatrix} 0 \\ \frac{v+H}{\sqrt{2}} \end{pmatrix}, \quad \phi_H = \frac{v_{\mu\tau} + H_{\mu\tau}}{\sqrt{2}}. \quad (5.4)$$

Therefore, the DM particle acquire its mass equaling to

$$m_{DM}^2 = \mu_{DM}^2 + \frac{1}{2}(v\lambda_{Dh} + v_{\mu\tau}\lambda_{DH}), \quad (5.5)$$

where $v/\sqrt{2}$ is the vacuum expectation value (vev) of SM Higgs field and $v_{\mu\tau}/\sqrt{2}$ is the vev of the new Higgs field.

To consider massive neutrinos, the model should contains extra right-handed neutrinos, which are heavy enough to suppress the mass of left-handed neutrinos. $U(1)_{L_\mu-L_\tau}$ model allows the related terms in type-I seesaw mechanism, and hence can explain the phenomena in neutrino oscillation and trident experiments [192, 198, 199]. The seesaw mechanism requires Majorana mass term. However, only N_e does not carry the $U(1)_{L_\mu-L_\tau}$ charge, and hence the Majorana mass term $\bar{N}_\mu^c N_\mu$ and $\bar{N}_\tau^c N_\tau$ are forbidden. Therefore, the full Lagrangian of the right-handed neutrinos containing both Majorana mass terms and Yukawa terms are

$$\mathcal{L}_N = \sum_{i=e,\mu,\tau} \left(\frac{i}{2} \bar{N}_i \not{D} N_i - (y_i \bar{L}_i \tilde{\phi}_h N_i + h.c.) \right) - \frac{1}{2} \begin{pmatrix} \bar{N}_e^c & \bar{N}_\mu^c & \bar{N}_\tau^c \end{pmatrix} \begin{pmatrix} M_{ee} & h_{e\mu} \phi_H^* & h_{e\tau} \phi_H \\ h_{e\mu} \phi_H^* & 0 & M_{\mu\tau} \\ h_{e\tau} \phi_H & M_{\mu\tau} & 0 \end{pmatrix} \begin{pmatrix} N_e \\ N_\mu \\ N_\tau \end{pmatrix}, \quad (5.6)$$

where $\tilde{\phi}_h = i\sigma_2 \phi_h^*$. After symmetry spontaneous breaking, the mass matrix of the neutrinos takes the form

$$M_\nu = \begin{pmatrix} 0 & M_D \\ M_D^\top & M_R \end{pmatrix}, \quad M_D = \begin{pmatrix} y_e \frac{v}{\sqrt{2}} & 0 & 0 \\ 0 & y_\mu \frac{v}{\sqrt{2}} & 0 \\ 0 & 0 & y_\tau \frac{v}{\sqrt{2}} \end{pmatrix}, \quad M_R = \begin{pmatrix} M_{ee} & h_{e\mu} \frac{v_{\mu\tau}}{\sqrt{2}} & h_{e\tau} \frac{v_{\mu\tau}}{\sqrt{2}} \\ h_{e\mu} \frac{v_{\mu\tau}}{\sqrt{2}} & 0 & M_{\mu\tau} e^{i\xi} \\ h_{e\tau} \frac{v_{\mu\tau}}{\sqrt{2}} & M_{\mu\tau} e^{i\xi} & 0 \end{pmatrix} \quad (5.7)$$

After the diagonalization of the mass matrix, the mass eigenstates of the neutrino are established and the tuning of the parameters ($y_e, y_\mu, y_\tau, v_{\mu\tau}, \xi, M_{\mu\tau}, M_{ee}, h_{e\mu},$ and $h_{e\tau}$), may explain the related experiments.

In sum, the final full Lagrangian of the model is

$$\mathcal{L} = \mathcal{L}_{SM} + \mathcal{L}_N + \mathcal{L}_{DM} + \mathcal{L}_H + \mathcal{L}_{Z'}. \quad (5.8)$$

Nevertheless, not every sector is testable through LHC experiments. First, the neutrinos are not detectable at collider and are treated as missing energy. Therefore, the final observables only depend on the sum of all flavors of neutrinos. Because of the unitarity of the mixing matrix, the distinction of the variables in the mixing matrix is hardly detectable from LHC experiments. Moreover, the right-handed neutrinos are predicted to be very heavy which are hard to generate at modern colliders. Thus, \mathcal{L}_N terms are not testable through LHC data. Second, non-collider data should be much more sensitive than the LHC data for λ_{Dh} and λ_{DH} , since the h_2 Higgs boson is supposed to be heavy and final state DM may decrease the total cross section in collider experiments. In contrast, the process, $\phi_{DM}^* \phi_{DM} \rightarrow h_2 \rightarrow b\bar{b}$, connecting the extra h_2 to SM particles, significantly contributes to the data from relic density and indirect detection [200]. Therefore, the strongest bound of such parameters should be from non-collider data. Third, λ_{DM} only relates to next leading order experiments through loop diagrams in LHC searches. Finally, the mixing of ϕ_h and ϕ_H is very small to prevent the mass

eigenstate h_1 from disagreeing the SM Higgs, and hence the effect can only be tested on higher order tree diagrams with 6 or 8 lepton final states. In sum, the extra part from the complete Lagrangian that is the most relevant sector for DM topic from LHC data is thus given by

$$\begin{aligned} \mathcal{L}_{\text{new}} = & (D_\mu \phi_{\text{DM}})^* D^\mu \phi_{\text{DM}} - m_{\text{DM}}^2 \phi_{\text{DM}}^* \phi_{\text{DM}} - \frac{1}{4} \mathcal{Z}'_{\mu\nu} \mathcal{Z}'^{\mu\nu} + \frac{1}{2} m_{Z'}^2 Z'^\mu Z'_\mu \\ & + g_{\mu\tau} (\bar{\mu} \mathcal{Z}'^\mu + \bar{\nu}_\mu \mathcal{Z}'^\mu \nu_\mu - \bar{\tau} \mathcal{Z}'^\mu \tau - \bar{\nu}_\tau \mathcal{Z}'^\mu \nu_\tau). \end{aligned} \quad (5.9)$$

The LHC signals we consider originate from the production and decay of (nearly) on-shell Z' bosons. At leading order the Z' can only decay into second or third generation leptons, and possibly into DM particles. The corresponding partial widths are given by

$$\Gamma(Z' \rightarrow l^+ l^-) = \frac{g_{\mu\tau}^2 m_{Z'}}{12\pi} \sqrt{1 - 4z_l} (1 + 2z_l), \quad \text{for } l = \mu, \tau; \quad (5.10)$$

$$\Gamma(Z' \rightarrow \phi_{\text{DM}} \phi_{\text{DM}}^*) = \frac{q_{\text{DM}}^2 g_{\mu\tau}^2 m_{Z'}}{48\pi} (1 - 4z_{\text{DM}})^{3/2}, \quad (5.11)$$

where $z_X \equiv m_X^2/m_{Z'}^2$. The partial width for Z' decays into one flavor (μ or τ) of neutrino is half of that given in eq.(5.10), since only the left-handed neutrinos are light enough to contribute. In our analysis we only consider scenarios where the total Z' width is smaller than $m_{Z'}$, since otherwise perturbation theory is not reliable. This is the same perturbativity condition compared to 3.12, even if we change the model. This translates into the condition

$$q_{\text{DM}}^2 (1 - 4z_{\text{DM}})^{3/2} + 4 \sum_{l=\mu, \tau} \sqrt{1 - 4z_l} (1 + 2z_l) + 4 < 48\pi/g_{\mu\tau}^2. \quad (5.12)$$

This bound is always satisfied for $g_{\mu\tau} \leq 3$ and $q_{\text{DM}} \leq 2$.

5.3 Application to LHC Data

At tree-level the only SM particles our Z' boson couples to are leptons of the second and third generation. These can be pair-produced via neutral or charged current Drell-Yan processes. The leading-order Z' production processes are based on these Drell-Yan reactions, with a Z' boson being emitted off the lepton line, see Fig. 5.1.

If the primary Drell-Yan process produces an $l^+ l^-$ pair (left diagram), $Z' \rightarrow l'^+ l'^-$ decays lead to final states containing four charged leptons, where flavor l' may be the same or different from l (with $l, l' \in \{\mu, \tau\}$). Invisible Z' decays, into neutrinos or DM particles, lead to final states with an opposite-sign same-flavor charged lepton pair plus missing E_T .

If the primary Drell-Yan reaction produces a $\nu_l \bar{\nu}_l$ pair (middle diagram), Z' decays into charged leptons again lead to $l^+ l^- E_T$ final states. For this production process invisible Z' decays do not result in a detectable final state.¹

¹ If a hard parton is emitted off the initial state this process would contribute to monojet production; however, it would merely be a higher-order correction to monojet production in the SM, and would thus certainly not lead to a detectable signal.

Finally, if the primary Drell–Yan reaction produces a $l^- \bar{\nu}_l$ pair or its charge conjugate (right diagram), Z' decays into charged leptons leads to final states of the type $l^\pm l'^+ l'^- E_T$, where the l and l' may again be the same or different flavors. In this case invisible Z' decays lead to final states with a single charged lepton plus missing E_T . This can be considered a higher–order correction to the SM charged–current Drell–Yan reaction, and will certainly have a far worse sensitivity than the $3l + E_T$ final state.

Of course, experimentally a μ and a τ look very different. In fact, primary muons and muons from tau decays cannot be distinguished reliably; we will just add these contributions. For reasons described in the Introduction, we do not consider final states containing electrons, which might be produced in tau decays. However, we do consider final states including hadronically decaying tau leptons, which we denote by τ_h .

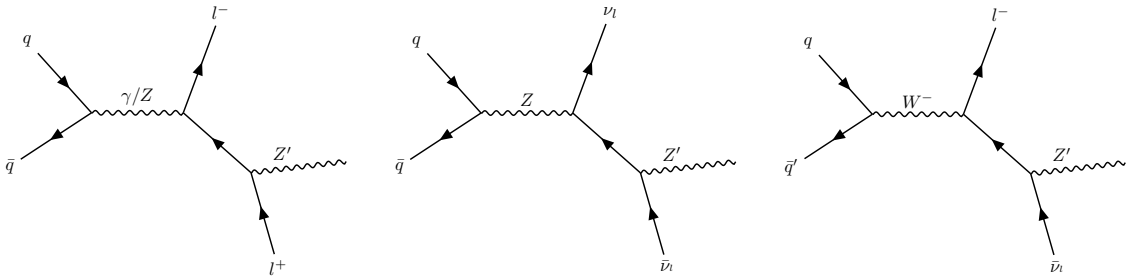


Figure 5.1: Examples of Feynman diagrams for $pp \rightarrow Z' l^+ l^-$ (left), $pp \rightarrow Z' \nu_l \bar{\nu}_l$ (center) and $pp \rightarrow Z' l \nu_l$ (right). For the left diagram, both visible (leptonic) and invisible Z' decays (into neutrinos or DM particles) contribute to signal processes, but for the central and right diagram only Z' decays into a charged lepton pair were considered. The Z' boson can also be emitted off the other lepton, and W^+ exchange diagrams also contribute. In the event generation the Z' is allowed to be off–shell.

Altogether, we thus consider the following distinct final states: 3μ , 4μ , $m\mu + n\tau_h$ ($m + n > 2$, $n \neq 0$), $2\tau_h + E_T$, $\mu\tau_h + E_T$, and $2\mu + E_T$. The corresponding LHC analyses we recast are summarized in Table 5.1. To that end we used the CheckMATE 2 framework [101], which in turn uses Delphes 3 [100] to simulate the CMS [201] and ATLAS [202] detectors. It should be noted that CheckMATE also uses several other public tools [100, 168–178]. As mentioned in the Introduction, we encoded a total of 281 new signal regions; we also used a few searches for superparticles in multi–lepton final states which had already been included in CheckMATE.

List of Analyses	Center–of–mass energy		
	7 TeV	8 TeV	13 TeV
Topologies			
$2\mu + E_T$	[203, 204]	[203, 205–207]	[158, 208–217]
$(2\tau_h \text{ or } \mu\tau_h) + E_T$			[157, 218–220]
$3\mu \text{ or } 4\mu$		[221]	[194, 212, 213, 216, 217, 222–228]
$m\mu + n\tau_h$ ($m + n > 2$, $n \neq 0$)		[229]	[212, 223, 227, 228]

Table 5.1: All analyses used in this chapter for leptophilic mediator.

In order to simulate the signal, we used `FeynRules` [97] to produce a model file output in UFO format [129]. Parton-level events were generated by `MadGraph` [98]. Specifically, we defined charged leptons (meaning μ^- and τ^-) and invisible particles (μ and τ neutrinos or antineutrinos as well as DM particles). The $2l$ signal events were generated by specifying `MadGraph` events containing a charged lepton–antilepton pair plus two missing particles; for the $3l$ signal, `MadGraph` generated events with three charged leptons and one missing particle; and the $4l$ signal started from `MadGraph`–generated events with two pairs of charged leptons. In all cases only diagrams containing one Z' propagator (i.e. two new couplings) were generated.

This means that the Z' boson is allowed to be off-shell, but interference between Z' and Z or photon exchange is not included. These interference terms formally vanish in the narrow width approximation, i.e. for $\Gamma_{Z'} \rightarrow 0$. These terms are therefore expected to be more important for larger coupling $g_{\mu\tau}$, which in turn are allowed for larger $m_{Z'}$, as discussed quantitatively below. However, we found that even for the largest coupling we consider, which respects the perturbativity constraint (5.12), the interference contribution to the cross section after cuts is at most 6% of the squared Z' exchange contribution. This is considerably less than the effect of typical QCD NLO corrections, which we also ignore. Note also that in the high mass region ($m_{Z'} > 100$ GeV), where the upper limit of $g_{\mu\tau}$ is sizable and considered offering noticeable interference contribution, we found the interference terms to be positive, so ignoring them is conservative.

These `MadGraph` events were passed on to `Pythia 8.2` [99] for parton showering and hadronization, and then to `CheckMATE 2` [101] which applies the selection cuts defined by the designated search regions and decides whether the given model is excluded by these searches or not.

We performed separate comparisons to $2l$, $3l$ and $4l$ searches; we remind the reader that l here means a muon or a hadronically decaying τ lepton. Some of the analyses we apply used data taken at $\sqrt{s} = 7$ or 8 TeV, which required separate event generation. However, at the end the analyses of data taken at $\sqrt{s} = 13$ TeV, many of which were published quite recently, always proved more constraining. Moreover, we find that replacing a muon in the final state by a hadronically decaying τ always reduces the sensitivity. The branching ratio for hadronic τ decays is about 65%, but the τ –tagging efficiency is well below the efficiency of identifying a muon, and QCD jets are much more likely to be misidentified as a hadronically decaying τ than as a muon. Nevertheless τ leptons do contribute to the final sensitivity, through $\tau \rightarrow \mu$ decays.

In the following we will present constraints on the $L_\mu - L_\tau$ gauge boson in two different scenarios. We begin with scenarios where the Z' boson does not decay into dark matter particles, either because $q_{\text{DM}} = 0$ or because $m_{\text{DM}} > m_{Z'}/2$. The strengths of all signals we consider can then be computed uniquely in terms of only two parameters: the mass $m_{Z'}$ and the coupling $g_{\mu\tau}$. We generate at least 20,000 events for each combination of Z' mass and coupling; if the total error in the most relevant signal region is dominated by Monte Carlo statistics, we generate additional events. Since the signal rates to good approximation scale like $g_{\mu\tau}^2$, we typically only need to try three to four values of the coupling in order to determine its upper bound for a given value of $m_{Z'}$.

In the upper frame of Fig. 5.2 we show upper bounds on $g_{\mu\tau}$ that have been derived in this manner as functions of $m_{Z'}$. The figure shows separate bounds from analyses of final states with two (green dot-dashed curve), three (red dashed curve) and four (dark blue solid curve) charged leptons. The lower frame shows the upper bounds on the corresponding total cross sections, which include the branching ratios for Z' decays but count each τ as a charged leptons, irrespective of its decay. The curves terminate in the region of large Z' mass when the perturbativity limit (5.12) is reached. The curves aren't always smooth. The reason is that `CheckMATE` uses the signal region with the best *expected*

sensitivity to set the bounds. This avoids “look elsewhere” effects, but can lead to discontinuities when the relevant signal region changes. Finally, we do not show bounds from $2l$ final states for $m_{Z'} < 10$ GeV since the cut efficiency becomes very poor there, i.e. we would need to generate a very large number of events in order to derive reliable results; we did not do that since the resulting bound will surely again be worse than that from $3l$ and $4l$ analyses.

The upper frame also shows the value of $g_{\mu\tau}$ where the full theory prediction, including Z' exchange, reproduces the measured value of $g_\mu - 2$. The brown solid line corresponds to the central value, whereas the darker and lighter shaded regions allow to reproduce $g_\mu - 2$ up to 1 and 2 standard deviations, respectively. Here we use

$$\Delta a_\mu = a_\mu^{exp} - a_\mu^{th} = (29.0 \pm 9.0) \times 10^{-10}$$

from [26], which is also used in the non-collider studies [190, 191] we discussed previously.

Finally, the lower dot-dashed line in the upper frame summarizes non-LHC bounds. For $m_{Z'} > 4$ GeV the results from non-LHC data come from our interpretation of the CCFR measurement of the cross section for “trident” production [230]. We used the CL_S method to set the 95% c.l. limit, which is also employed by CheckMATE. The resulting bound on $g_{\mu\tau}$ is $\sim 20\%$ weaker than that derived by taking the central value of the CCFR cross section plus 1.64 times the CCFR error as upper bound on the cross section, which seems to have been done in [192]; note that the cross section measured by CCFR is somewhat below the SM prediction.² For $m_{Z'} < 4$ GeV the best non-LHC bound comes from 4μ searches by the BaBar collaboration [232]. We show a smoothed-out version of the actual bound, which fluctuates rapidly by $\sim \pm 30\%$ around this line. In [233] it was shown that bounds from tests of lepton universality are always weaker than that from the neutrino trident experiments in the parameter region we focus on ($m_{Z'} \leq 500$ GeV). We therefore do not show these constraints in Fig. 5.2.

As mentioned above, there is only one published analysis of LHC data that specifically searches for the $L_\mu - L_\tau$ gauge boson [194]; it covers the mass range $5 \text{ GeV} < m_{Z'} < 70 \text{ GeV}$ using $Z \rightarrow 4\mu$ decays in the CMS detector. Our CheckMATE based recast of this analysis leads to a similar, but slightly weaker constraint on $g_{\mu\tau}$ for given $m_{Z'}$; this difference presumably results from inaccuracies of the fast Delphes 3 simulation of the CMS detector, as compared to the full simulation based on Geant 4 [234] employed by the CMS collaboration. For Z' masses between 10 and 60 GeV, this search provides the strongest bound of all LHC searches.

However, outside this mass range the tightest LHC constraint comes from other searches. In particular, for $m_{Z'} < 10$ GeV the 4μ search in [228], which includes softer muons, is comparable to or sometimes stronger than [194]. On the other hand, for $m_{Z'} > 60$ GeV the best LHC bound comes from searches for 3μ final states, the most important ones being [222] and, for $m_{Z'} > 100$ GeV, [228]. Another analysis [212] uses the same selection rules as [228] with different categorization, and thus gives similar results. The main reason for the good performance of the 3μ searches is that the cross section for the charged current Drell-Yan process is larger by a factor of 2.5 to 3 than that for the corresponding neutral current process leading to a charged lepton pair; this relative ordering is not affected much by the Z' boson emitted off the leptons line (see Fig. 5.1) [187]. Moreover, the cut efficiency for the most sensitive 3μ analysis turns out to be a little better.

On the other hand, Fig. 5.2 also shows that the LHC bounds are stronger than existing constraints

² The CHARM-II collaboration also measured this cross section, with a different neutrino beam, and found a result somewhat larger than, but compatible with, the SM prediction [231]. Naively averaging the two measurements of σ_{exp}/σ_{SM} leads to a very similar bound on $g_{\mu\tau}$ when using the CL_S method.

only in the mass range covered by the dedicated search [194]. Note also that the upper bounds on the signal cross sections flatten out, or even slightly increase, at large Z' masses (lower frame). This is a sure sign that the cuts were not optimized for the $L_\mu - L_\tau$ model. For example, the upper bound derived from 3μ final states in [228] increases at large $m_{Z'}$ largely because of a transverse mass cut, which loses efficiency.

So far we have assumed that DM particles cannot be produced in on-shell Z' decays. If we allow $Z' \rightarrow \phi_{\text{DM}}\phi_{\text{DM}}^*$ decays the branching ratio for $Z' \rightarrow l^+l^-$ decays will be reduced, leading to reduced $3l$ and $4l$ signals. However, since we consider a scalar DM particle, even for $q_{\text{DM}} = \pm 2$ the branching ratio for Z' decays into DM particles does not exceed 25%. This would reduce the upper bounds on $g_{\mu\tau}$ derived from these channels by a factor of at most $\sqrt{12}/4 \simeq 0.86$.

The situation for the $2l$ channel is different. The contribution from the left Feynman diagram in Fig. 5.1 to this final state increases with increasing branching ratio for invisible Z' decays, while that from the middle diagram decreases. Since for $|q_{\text{DM}}| \leq 2$ the branching ratio for invisible Z' decays is never more than 50%, one might expect the former effect to be dominant; however, the two diagrams have both different total cross sections and different cut efficiencies, making a numerical analysis necessary.

Some results are shown in Fig. 5.3, for $g_{\mu\tau} = 1$ and $q_{\text{DM}} = 1$ (upper) and 2 (lower). The green regions are excluded by our recast of analyses of 2μ final states; the corresponding exclusion limits in the absence of $Z' \rightarrow \text{DM}$ decays are given by the horizontal black lines. The fact that the green regions extend beyond the upper horizontal line shows that allowing $Z' \rightarrow \phi_{\text{DM}}\phi_{\text{DM}}^*$ decays increases the sensitivity of this final state somewhat, the effect being slightly bigger for $q_{\text{DM}} = 2$. The strongest bounds are from three different analyses of data taken at $\sqrt{s} = 13$ TeV [211, 213, 215], and their cut efficiencies are indeed quite different for $pp \rightarrow Z' \nu_l \bar{\nu}_l$ and $pp \rightarrow Z' l \bar{l}$ processes. However, this entire region of parameter space is still excluded by analyses of final states with three or four muons. Therefore LHC data are not sensitive to the production of dark matter particles in this model.

So far we have considered a complex scalar as dark matter candidate. However, in on-shell Z' decays the spin of invisible particles cannot be determined; the only quantity relevant for LHC analyses is the invisible branching ratio of the Z' boson. For example, we could just as well consider a Dirac fermion χ as dark matter candidate. The relevant partial width would then be given by

$$\Gamma(Z' \rightarrow \bar{\chi}\chi) = \frac{m_{Z'}'}{12\pi} \sqrt{1 - 4z_{\text{DM}}^2} (g_V^2 + g_A^2 + 2z_{\text{DM}}(g_V^2 - 2g_A^2)), \quad (5.13)$$

where the g_A is the axial vector coupling, g_V is the vector coupling, and $z_{\text{DM}} = m_\chi^2/m_{Z'}^2$. For $g_V = 0$ and $g_A = g_{\mu\tau}$, this partial width is the same as that for scalar DM for $q_{\text{DM}} = 2$ shown in the lower frame of Fig. 5.3. On the other hand, for $g_A = 0$ and $g_V = g_{\mu\tau}$, eq.(5.13) predicts a somewhat larger partial width for sizable mass of the DM particle. However, the branching ratio for Z' decays into dark matter still remains below 25%, and the constraints from $2\mu + \cancel{E}_T$ searches remain far weaker than those from analyses of final states with 3 or 4 muons.

5.4 Conclusions

In this chapter, we recast a large number of LHC analyses, summarized in Table 5.1, from both the CMS and ATLAS collaborations in the CheckMATE framework in order to constrain the $U(1)_{L_\mu - L_\tau}$

extension of the SM. Here we focus on the new Z' gauge boson predicted by this model, whose mass and coupling are the main free parameters relevant for LHC physics. We find that recently published analyses of data taken at $\sqrt{s} = 13$ TeV always have higher sensitivity than LHC data taken at lower energies. These data exclude Z' masses up to 550 GeV for perturbative couplings. We analyzed final states containing two, three or four charged leptons, where a charged lepton is here defined as a muon or a hadronically decaying τ lepton. Final states with only two charged leptons in principle would have the highest sensitivity to Z' decays into invisible dark matter particles, but this final state is always much less sensitive than the $3l$ and $4l$ final states. Moreover, replacing a muon by a hadronically decaying τ lepton always reduced the sensitivity. The final LHC limit is therefore set by 4μ final states for $5 \text{ GeV} < m_{Z'} < 60 \text{ GeV}$, and by 3μ final states otherwise. However, except for $10 \text{ GeV} < m_{Z'} < 60 \text{ GeV}$ LHC data are still no more sensitive to this model than data taken at much lower energies, in particular analyses of $\nu_\mu N \rightarrow \mu^+ \mu^- N$ “trident” production by the CCFR collaboration [230].

Only one analysis we use [194], which looks for $Z \rightarrow 4\mu$ decays, has been designed specifically for this Z' boson. It is thus very likely that the sensitivity could be enhanced, in particular for larger Z' masses, by optimizing the cuts, in particular in 3μ final states which have a larger cross section before cuts. A further increase of sensitivity might be possible by statistically combining final states with muons and with hadronically decaying τ leptons, since the relative normalization of these channels can be predicted unambiguously in this model; for example, for $m_{Z'} \geq 10 \text{ GeV}$, where lepton mass effects are negligible, the branching ratios for Z' decays into $\mu^+ \mu^-$ and $\tau^+ \tau^-$ are essentially the same.

In this chapter we focused on the production of the new Z' gauge boson. The model also contains a new Higgs boson, which may decay via two real or virtual Z' bosons into up to four charged leptons. Both the decay of the 125 GeV Higgs boson into two of the new Higgs bosons, and the emission of the new Higgs boson off a Z' boson in one of the diagrams of Fig. 5.1, can therefore lead to spectacular final states with up to eight charged leptons. Unfortunately, there are too many diagrams from the SM containing eight lepton final state. Thus, the calculation speed is too slow to work out through the calculating power of our computer. We therefore calculate the cross section of 6-lepton final state from the SM instead. The cross section is very tiny and hence negligible even for 6-lepton final state ($\sim 2.3 \times 10^{-7}$ pb with some preset cuts), while the 8-lepton final state is supposed to have smaller cross section. On the other hand, from our model, the 8-lepton final state has larger cross section even compared to 6-lepton case from the SM. Therefore, if the signal from our model is sizable enough³ in some parameter spaces, those spaces should be excluded directly, since it is much larger than the SM estimation. Nevertheless, given that the complexity of the parameters in the Higgs sector are not as simple as those in DM sector, topics relevant to the Higgs sector should be carefully discussed in the future work.

³ “sizable enough” for detection in collider experiments means that at least 3 events can be measured through the detector in recent total integrated luminosity.

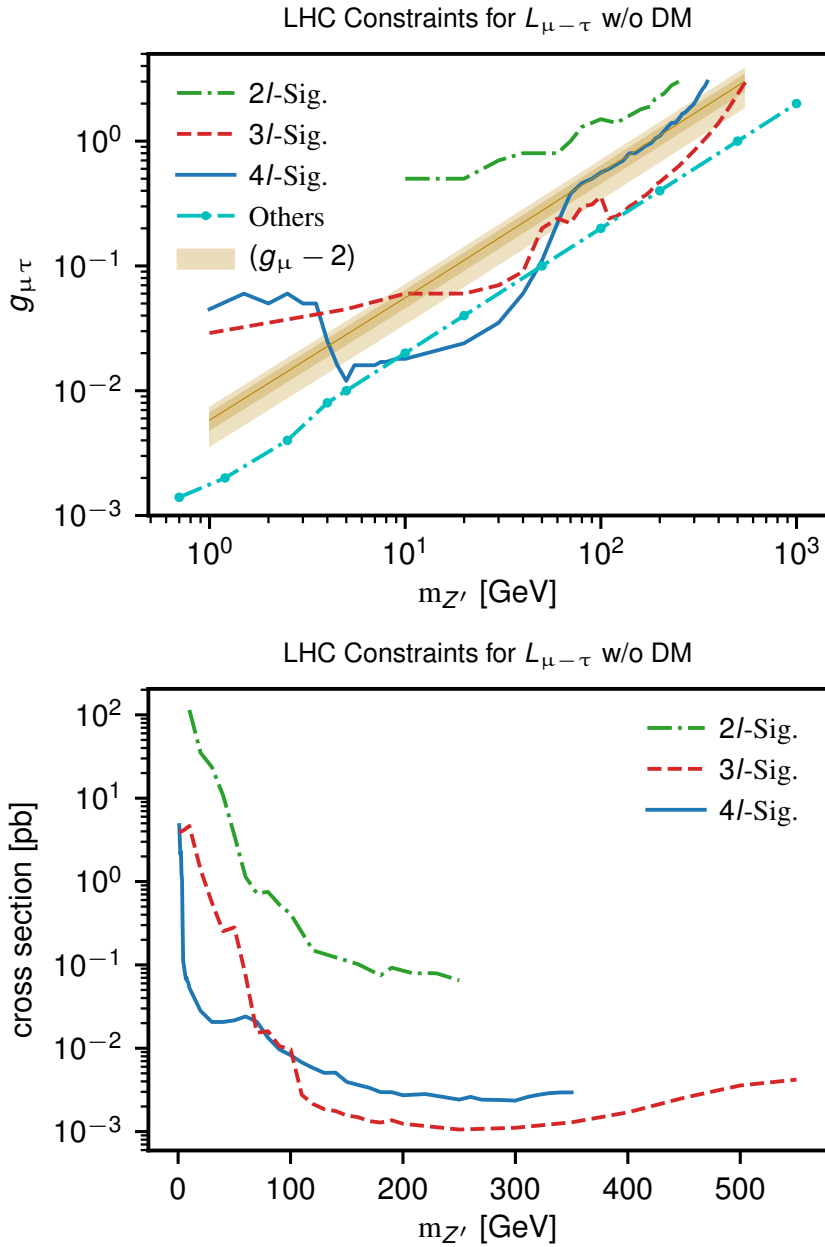


Figure 5.2: The upper limit on the new coupling $g_{\mu\tau}$ (upper) and the corresponding cross section before cuts (lower). The upper frame also shows the value of the coupling indicated by the measurement of the anomalous magnetic moment of the muon (shaded area), as well as a summary of existing constraints (lower dot-dashed curve); see the text for further details.

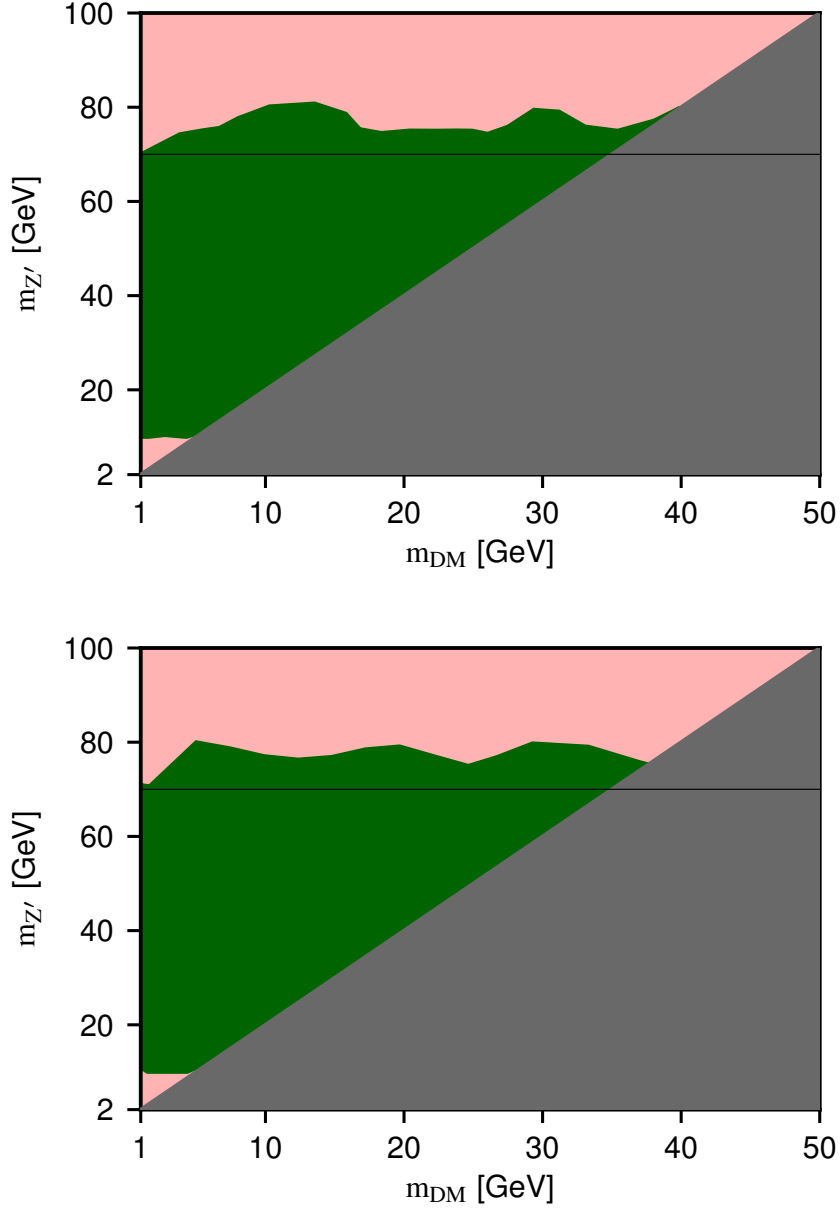


Figure 5.3: The effect of Z' decays into dark matter particles on the constraint from $2l$ final states, for $g_{\mu\tau} = 1$ and $q_{DM} = 1$ (upper) and 2 (lower). In the gray region below the diagonal these decays are kinematically forbidden, i.e. the result of Fig. 5.2 holds. The green region is excluded by analyses of 2μ final states at $\sqrt{s} = 13$ TeV; in the absence of $Z' \rightarrow DM$ decays these analyses exclude the region between the horizontal lines. The pink region is excluded by analyses of 4μ final states, which are only mildly affected by $Z' \rightarrow DM$ decays; this includes the entire green region.

Application on Machine Learning Based Classifiers

In the previous Chapter, we see that although we applied all the released LHC analyses with multi-lepton final states, the bound from LHC data is still in general weaker than the result from non-LHC experiments. Nevertheless, in the special parameter region, $m_{Z'}$ from 10 GeV to 60 GeV, the LHC constraints are the strongest compared to other experiments. As we mentioned in the previous chapter, the CMS paper that designs cuts specially for $U(1)_{L_\mu-L_\tau}$ extension of SM. Therefore, the redesign of the selection rules could be helpful to improve the final bounds from the LHC data. Additionally, from the result in previous chapter, the $3l$ signal in general should be better than $4l$ and $2l$ due to the larger total cross section. Therefore, we begin from the optimization of $3l$ signal.

In this chapter of Part III, we want to discuss the improvement of LHC constraints for $U(1)_{L_\mu-L_\tau}$ model. There are several ways to do the optimization for certain model. First is to design dedicated cuts like what we do in Chapter 3. However, the LHC background is much more complex than the LEP case. The reduction of QCD background is quite non-trivial. Therefore, to design cuts that can reduce the QCD background and boost the signal to background ratio after the cuts is not very easy in general. Therefore, repeating our work for LEP analysis is challenging. Moreover, unlike the LEP case, which has no specially designed analysis for our model, the CMS collaboration has already designed cuts for $U(1)_{L_\mu-L_\tau}$, and hence if their cuts only work from 10 GeV to 60 GeV, it is hard to easily extend the conclusion for larger parameter space. Fortunately, besides the cut-based analysis, there are still other ways to reduce the background and to boost the signal to background ratio. From 20 years ago, Neural Network has already been used to tag a jet as b -jet. Now a toolkit called *The Toolkit for Multivariate Data Analysis* (TMVA¹) is developed to apply more specialized Machine Learning algorithms on collider related topics. Additionally, the development of GPU and CPU highly increases the efficiency of Machine Learning. Thus, it offers us a series of competitive classifiers to distinguish Signal and background. Moreover, the tree-based algorithms, like Boosted Decision Tree can offer the information of the feature importance of various parameters we select to describe the simulated signatures. Therefore, we try to apply Support Vector Machine, Random Forest, AdaBoost, XGBoost, Neural Network, etc. to classify the signal and background. We implement XGBoost through the standard XGBoost Python package², while we implement other algorithms through the

¹ <https://root.cern.ch/tmva>

² <https://xgboost.ai>

combination of Scikit-learn³, Keras⁴ and Tensorflow⁵.

Developing classifier is a well known topic in Computer Science. A lot of researches focus on this topic to solve a series of puzzles and to benchmark various algorithms on certain challenges. Obviously, it should be better than the cut based classification on the efficiency side. However, the cut based analysis helps us understand the physical aspects clearly. For instance, the missing energy cut directly reflects the mass of invisibly decaying mediator. It is very convenient to connect the experimental data and the theoretical settings inside Lagrangian through the selection rules. Therefore, we try to combine the results from different machine learning algorithms through votes from various classifier for the stronger bounds, while we use the feature importance information from XGBoost to point out the most important features that reflects the physical properties. We select all the variables designed for $3l$ analysis in Chapter 5. Since the experimentalists in ATLAS and CMS are more professional than us to design the selection rules, they have already develop a series of variables related to multi-lepton topology in LHC. We calculate out all the variables and use them as the input vector for Machine Learning classifiers. According to the feature importance we get from XGBoost, we are able to drop the the useless feature to decrease the calculating complexity and to increase the size of the data set from the simulation to improve the result. Finally, we simulate 1000000 signal events for a single mass point of $m_{Z'}$, e.g. 1000000 for $m_{Z'} = 100$ GeV, while the number of SM events simulated by us is equal to the total number of signal events for all the mass points to keep the 1 : 1 ratio between signal and background before the preselection and training procedure.

To test our classifier, we use “test data set” that contains the signal to background ratio roughly equaling to the cross section ratio between our model and SM. Through the application of the same preselection before training and trained model on the regenerated and unbiased test data set, we get the remaining events, which are the events tagged as “Signal” by our classifier, and then we can use the signal from our model and the background from SM after our selection to estimate the new bound for a 95% confidential level, similar to the case in Chapter 3 Section 3.4. Our recent results are shown in Fig. 6.1 and Fig. 6.2 for feature importance and improved bound respectively. In the figure of feature importance, we use CheckMATE to calculate all the features⁶. Those 2 kinds of transverse masses are defined as internal functions, and hence can be visited directly from CheckMATE. Obviously, the most important feature is the invariant mass of the di-muon pair that minimize the value of $|m_Z - m_{\mu^+\mu^-}|$. Therefore, when the value is extremely near to the Z mass, it loses its efficiency. From Fig. 6.2, it is clear to see unusual behavior between 90 GeV and 100 GeV, which agreeing our estimation from the feature importance. Therefore, the feature importance is indeed helpful to achieve the physical information.

In Fig. 6.2, there are 2 different figures from 2 kinds of preselection respectively. In the first one, we apply $\cancel{p}_T > 100$ GeV cut before training the classifier. In the second one, we only apply $\cancel{p}_T > 10$ GeV cut before training the classifier. The results show that the weaker cut is much better than the stronger cut. The reason of this result is that the Machine Learning classifier is in general much better than the cut based methods. Nevertheless, if we use $\cancel{p}_T > 1$ GeV, the result is again much worse than $\cancel{p}_T > 10$ GeV. The reason is that the necessary cut from our physical perspectives helps us remove the anomalies and outlier in the data. Furthermore, if we do not apply any cut, there could be a large number of useless events that highly decrease the speed of training. Therefore, some weak and

³ <https://scikit-learn.org>

⁴ <https://keras.io>

⁵ <https://www.tensorflow.org>

⁶ https://checkmate.hepforge.org/documentation/group__kinematics.html

physical cuts are still necessary.

The recent result we get through Machine Learning has already been the best compared to all other analyses. Even if we can not compare the bound from real data with the estimated bound directly, it still implies the potential of the Machine Learning algorithms. The latter steps in the Machine Learning approach could be the analysis of $2l$ -signal and $4l$ -signal to consider the DM related sector. Moreover, we can try to use kernel function to construct some new features that have physical meaning or to remove most of the unnecessary features. In sum, the Machine Learning tools are very helpful on our collider analysis for DM related models.

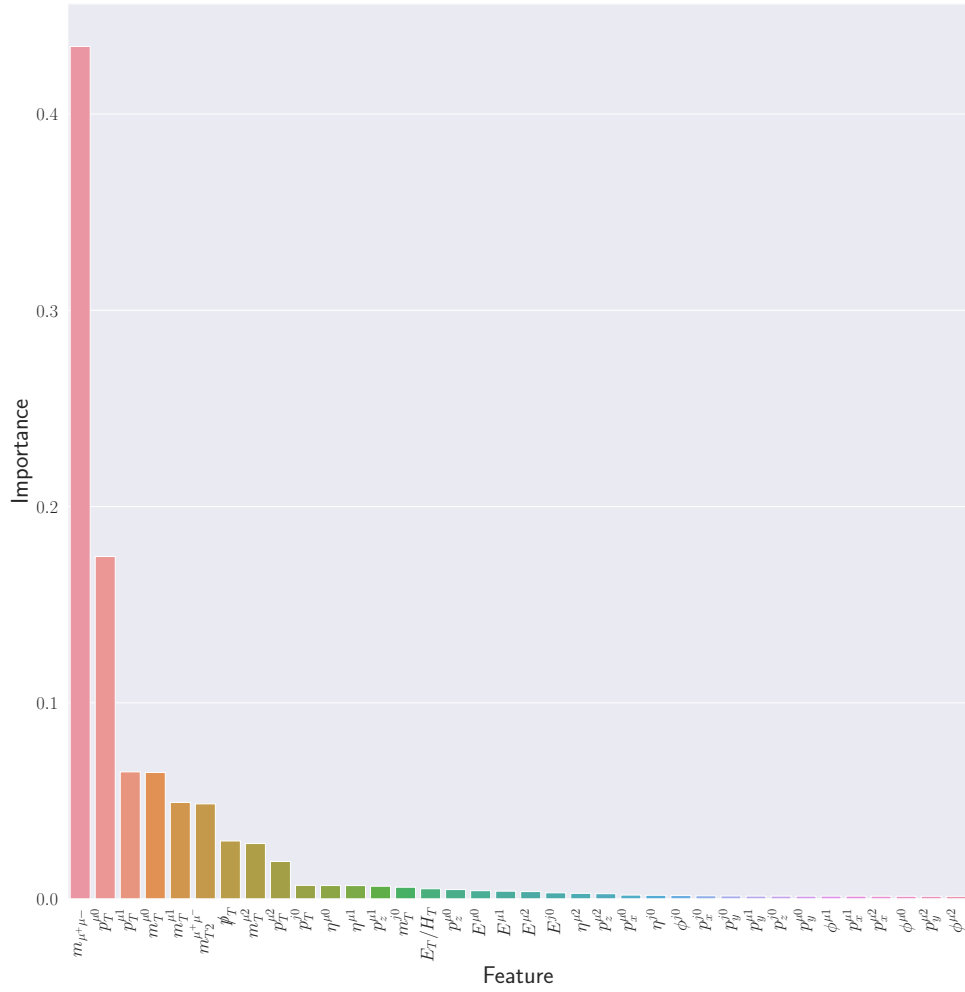


Figure 6.1: The figure shows the feature importance from XGBoost. The x -axis is the variables with leading importance we use in our Machine Learning. Larger importance means more important variables. E , p_x , p_y , p_z , and p_T are the 4-momenta and transverse momentum of the final state leptons and the most energetic jet, while the number 0 – 2 means the position in the energetic series. η and ϕ are the angular position of final state objects. Missing p_T is the missing transverse momentum. m_T and m_{T2} are 2 kinds of transverse mass, H_T is the scalar sum of jet transverse momenta, and $m_{\mu^+\mu^-}$ is the invariant mass of the di-muon pair that minimize the value of $|m_Z - m_{\mu^+\mu^-}|$.

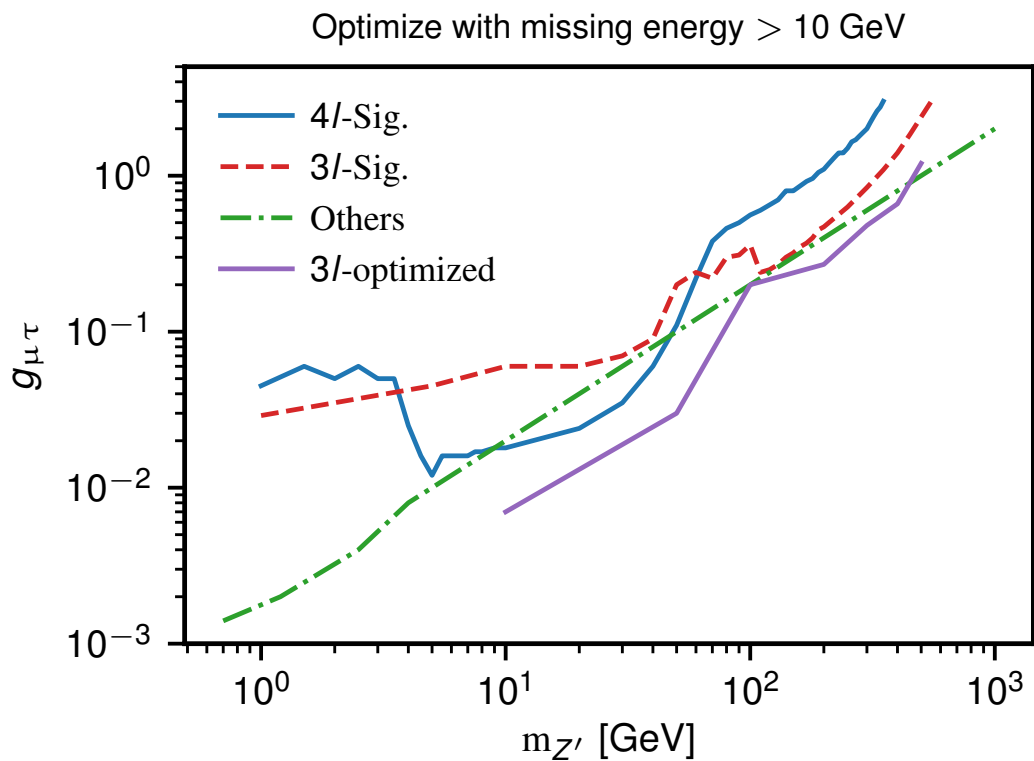
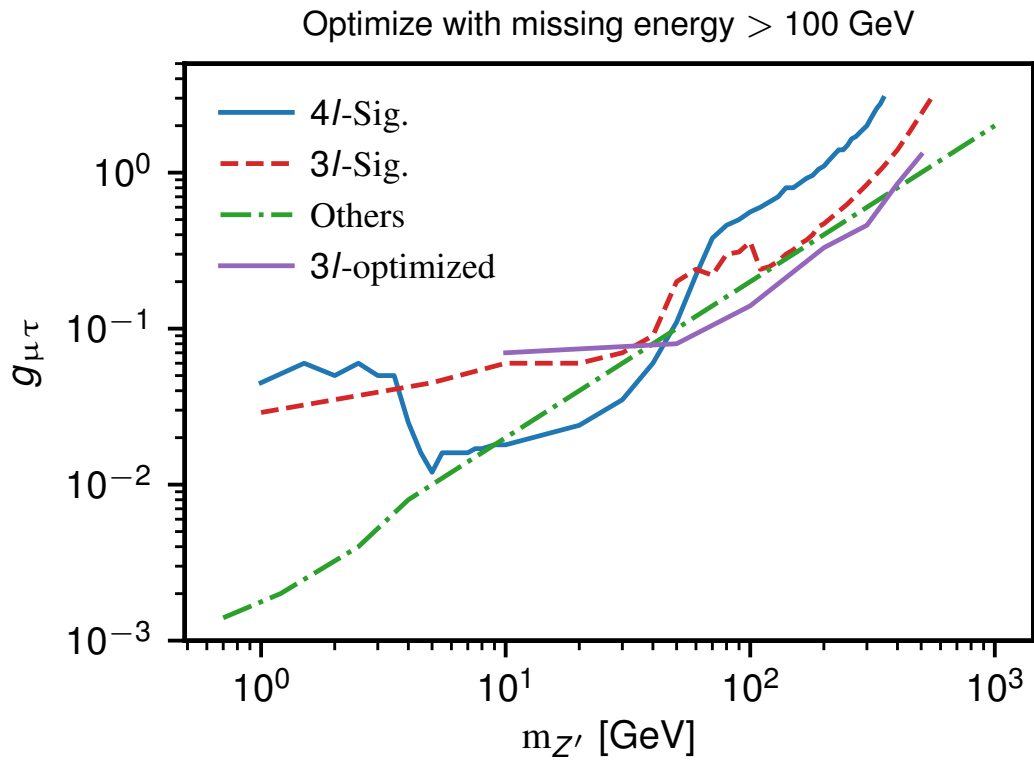


Figure 6.2: The figure shows the optimized bound from 3l-signal. The upper figure drops all the signal and background data with $\cancel{p}_T > 100$ GeV before training, while the lower figure drops data with $\cancel{p}_T > 10$ GeV.

Part IV

The 4th Part: Summary, Bibliography and Appendix

Summary

In this thesis, we overview the experiments, observations, and simplified models of DM. DM is an attractive and important topic of BSM physics. The hint of its existence appears in various scales in galaxies, galaxy clusters, and the Universe. Although there are other candidate theories for certain observation puzzles, it is difficult for those alternative candidates to explain all the unexpected observations through one simple hypothesis. Moreover, the distinction between luminous mass and total mass in bullet clusters is not easy to work out through other models besides DM such as modified Newton gravitation. Additionally, DM model is very simple, since only mass distribution is needed in the macroscopic scale. In sum, the observation in astronomy implies that DM is a very competitive model to solve all the observational puzzles altogether. The microscopic detail of DM, however, is not straightforward to study. Since the lack of electromagnetic interaction, which is the foundation of the most of detection strategies, the properties and origins of DM require more advanced searches. The direct detection, indirect detection, and collider searches are the recent experiments that we can use to discuss the theoretical models. They offer chances to test the interactions between DM and the quarks, leptons, or other sectors in the SM. After the overview of all experiments and observation, we focus on the collider searches in this thesis.

A theoretical model with a large number of parameters is hardly testable through experimental data. Therefore, we build simplified models with a limited number of parameters in this thesis to make our models testable. The simplified models contain an extra mediator that offers the connection between the SM and DM particles. Whatever the mediator couples to, the couplings of new interactions, mediator mass, and DM mass always appear as the new parameters. Through our application of LHC and LEP data, we find that the assumption with only mediator mass and interaction couplings are well constrained by our tests. In contrast, if we introduce more parameters related to DM, the constraints are not good enough in general. On the one hand, we try to consider other methods of event selection, such as the Machine Learning based classifiers. On the other hand, the result proves our understanding of simplified models, i.e. a large number of parameters may make the model untestable. For a more complete model, which contains more sectors like an extra Higgs sector and flavor mixing, more signatures should be considered together, while the constraints from their simplified model should be analyzed as hints for the complete models. Additionally, the simplified models are useful for building a connection between the experimental events in the detector and the theoretical models as well. Some selected kinetic parameters are sensitive enough to distinguish signal from the SM background. It helps us understand the properties of the theoretical assumptions. Even if we use the

Machine Learning classifier instead of the cut based analysis, the feature importance also offers the information concerning the most remarkable variables.

In this thesis, we recast a very large number of collider searches from LHC and LEP. The first kind of mediator we carefully discussed is the leptophobic mediator that couples to heavy quarks.

From LEP, we apply data taken at the e^+e^- collider LEP in the 1990's at center-of-mass energy up to 209 GeV. We assume that the dark sector particle (DSP) is a spin-1/2 fermion χ . This scenario is well studied in the context of LHC searches for mediator mass from 100 GeV to several TeV. Emission of the mediator off a quark or antiquark at LEP gives rise to di-jet plus missing energy and 4-jet signatures, which we use to limit the relevant couplings. We focus on scenarios with $2m_\chi > m_R$, which are poorly constrained by LHC data. We recast published searches by the ALEPH collaboration. For $m_\chi \lesssim 20$ GeV the best bounds result from an analysis at $\sqrt{s} \simeq M_Z$ of di-jet plus missing energy events. For heavier DSP but $m_R \lesssim 70$ GeV meaningful bounds can be derived from a four jet analysis at $\sqrt{s} = 183$ GeV. Unfortunately published searches using four jet final states at $\sqrt{s} \simeq M_Z$ use only a small fraction of the total data sample. Moreover, all published searches for di-jet plus missing energy final states at $\sqrt{s} \geq 130$ GeV have poor efficiency for our model; we therefore design new cuts that combine good background rejection with higher efficiency. Re-analyzing the higher energy data using our new cuts, and an analysis of the complete four jet data sample taken at $\sqrt{s} \simeq M_Z$, can explore new regions of parameter space.

From LHC, we recast ATLAS and CMS searches for final states containing one or more jet(s) + \cancel{E}_T , with or without b tags, as well as searches for di-jet resonances with b or t tagging. We find that LHC constraints on the axial vector couplings of the mediator are always stronger than the unitarity bound, which scales like m_R/m_t . If R has a sizable invisible branching ratio, the strongest LHC bound on both vector couplings and axial vector coupling comes from a di-jet + \cancel{E}_T search with or without double b tag. These bounds are quite strong for $m_R < 1$ TeV, even though we have switched off all couplings to valence quarks. Searches for a di-jet resonance with double b tag lead to comparable bounds with the previous results even if $R \rightarrow \chi\bar{\chi}$ decays are allowed; these are the only sensitive LHC searches if the invisible branching ratio of R is very small or zero.

In sum, the off-shell case can only be probed by LEP data in the low mass region. The LEP data loses sensitivity from mediator mass $\gtrsim 70$ GeV. On the other hand, the LHC data is sensitive enough for mediator mass < 1 TeV. Nevertheless, the LHC data cannot probe DM decaying from off-shell mediator. From our result, the off-shell case is quite different with the on-shell case, especially for low mediator mass values. The transverse part of the propagator of the mediator is the main contribution in the on-shell case. However, in the off-shell case, the longitudinal part of the propagator of the mediator is competitive, especially for a very light mediator mass, 2 GeV, 1 GeV, or even lighter.

The second kind of mediator we carefully discussed is the extension of the SM by an anomaly-free $U(1)_{L_\mu-L_\tau}$ gauge group; this model contains a new gauge boson (Z') and a scalar dark matter particle (ϕ_{DM}). We recast a large number of LHC analyses of multi-lepton final states by the ATLAS and CMS collaborations. We find that for $10 \text{ GeV} < m_{Z'} < 60 \text{ GeV}$ the strongest constraint comes from a dedicated Z' search in the 4μ final state by the CMS collaboration; for larger Z' masses, searches for final states with three leptons plus missing E_T are more sensitive. Searches for final states with two leptons and missing E_T , which are sensitive to Z' decays into dark matter particles, can only probe regions of parameter space that are excluded by searches in the 3 and 4 lepton channels. The combination of LHC data excludes values of Z' mass and coupling constant that can explain the deficit in $g_\mu - 2$ for $4 \text{ GeV} \leq m_{Z'} \leq 500 \text{ GeV}$. However, for much of this range the LHC bound is weaker than the bound that can be derived from searches for “trident” events in neutrino-nucleus scattering

Since we find that the result from the LHC analyses is weaker than non-LHC experiments in most of parameter region, except $10 \text{ GeV} < m_{Z'} < 60 \text{ GeV}$, we therefore apply Machine Learning classifiers to improve the estimated results for $3l$ -signal, since the cross section of $3l$ -signal is the largest and hence is supposed to be the best. If the cut in our pre-selection is not too strong, the estimated result is indeed better than all other bounds from real experiments. The Machine Learning based analysis could be a good alternative to solve similar problems in the future instead of the cut based analysis. It not only gives bounds for selective models, but also offers the information to help us select the most important features. The combination of the simplified model that decrease the number of free variables and the data driven analysis from Machine Learning algorithms helps us discover the testable models related to Dark Matter or other models beyond the Standard Model.

Bibliography

- [1] M. Drees and Z. Zhang, *Constraints on Mediator Coupled to Heavy Quarks from LHC Data*, *Physics Letters B* **797** (2019) 134832, arXiv: 1903.00496 [hep-ph] (cit. on p. vii).
- [2] M. Drees, M. Shi, and Z. Zhang, *Constraints on $U(1)_{L_\mu-L_\tau}$ from LHC Data*, *Phys. Lett.* **B791** (2019) 130, arXiv: 1811.12446 [hep-ph] (cit. on p. vii).
- [3] M. Drees and Z. Zhang, *Constraints on a Light Leptophobic Mediator from LEP Data*, *JHEP* **08** (2018) 194, arXiv: 1805.02780 [hep-ph] (cit. on p. vii).
- [4] G. Aad et al., *Observation of a new particle in the search for the Standard Model Higgs boson with the ATLAS detector at the LHC*, *Phys. Lett.* **B716** (2012) 1, arXiv: 1207.7214 [hep-ex] (cit. on p. 3).
- [5] S. Chatrchyan et al., *Observation of a New Boson at a Mass of 125 GeV with the CMS Experiment at the LHC*, *Phys. Lett.* **B716** (2012) 30, arXiv: 1207.7235 [hep-ex] (cit. on p. 3).
- [6] W. J. Marciano and H. Pagels, *Quantum Chromodynamics: A Review*, *Phys. Rept.* **36** (1978) 137 (cit. on p. 3).
- [7] S. L. Glashow, *Partial Symmetries of Weak Interactions*, *Nucl. Phys.* **22** (1961) 579 (cit. on p. 4).
- [8] S. M. Bilenky and J. Hosek, *GLASHOW-WEINBERG-SALAM THEORY OF ELECTROWEAK INTERACTIONS AND THE NEUTRAL CURRENTS*, *Phys. Rept.* **90** (1982) 73 (cit. on p. 4).
- [9] G. Aad et al., *Combined search for the Standard Model Higgs boson using up to 4.9 fb^{-1} of pp collision data at $\sqrt{s} = 7 \text{ TeV}$ with the ATLAS detector at the LHC*, *Phys. Lett.* **B710** (2012) 49, arXiv: 1202.1408 [hep-ex] (cit. on p. 4).
- [10] S. Chatrchyan et al., *Combined results of searches for the standard model Higgs boson in pp collisions...*, *Phys. Lett.* **B710** (2013) 26, arXiv: 1202.1488 [hep-ex] (cit. on p. 4).
- [11] R. J. Crewther et al., *Chiral Estimate of the Electric Dipole Moment of the Neutron in Quantum Chromodynamics*, *Phys. Lett.* **88B** (1979) 123, [Erratum: *Phys. Lett.* 91B,487(1980)] (cit. on p. 4).
- [12] C. A. Baker et al., *An Improved experimental limit on the electric dipole moment of the neutron*, *Phys. Rev. Lett.* **97** (2006) 131801, arXiv: hep-ex/0602020 [hep-ex] (cit. on p. 4).
- [13] Y. Fukuda et al., *Evidence for oscillation of atmospheric neutrinos*, *Phys. Rev. Lett.* **81** (1998) 1562, arXiv: hep-ex/9807003 [hep-ex] (cit. on p. 4).

- [14] Q. R. Ahmad et al., *Direct evidence for neutrino flavor transformation from neutral current interactions in the Sudbury Neutrino Observatory*, *Phys. Rev. Lett.* **89** (2002) 011301, arXiv: [nucl-ex/0204008 \[nucl-ex\]](#) (cit. on p. 4).
- [15] P. F. de Salas et al., *Status of neutrino oscillations 2018: 3σ hint for normal mass ordering and improved CP sensitivity*, *Phys. Lett.* **B782** (2018) 633, arXiv: [1708.01186 \[hep-ph\]](#) (cit. on pp. 4, 5).
- [16] S. Deser, *Infinities in quantum gravities*, *Annalen Phys.* **9** (2000) 299, arXiv: [gr-qc/9911073 \[gr-qc\]](#) (cit. on p. 4).
- [17] H. P. Nilles, *Supersymmetry, Supergravity and Particle Physics*, *Phys. Rept.* **110** (1984) 1 (cit. on p. 5).
- [18] M. Tanabashi et al., *Review of Particle Physics*, *Phys. Rev.* **D98** (2018) 030001 (cit. on pp. 5, 16).
- [19] R. Aaij et al., *Search for lepton-universality violation in $B^+ \rightarrow K^+ \ell^+ \ell^-$ decays*, *Phys. Rev. Lett.* **122** (2019) 191801, arXiv: [1903.09252 \[hep-ex\]](#) (cit. on p. 5).
- [20] M. Smith, *Tests of lepton universality with semi-tauonic b-quark decays*, *J. Phys. Conf. Ser.* **1137** (2019) 012017 (cit. on p. 5).
- [21] O. Leroy, *Tests of lepton universality with semitauonic b-quark decays*, *PoS ICHEP2018* (2018) 126 (cit. on p. 5).
- [22] K. De Bruyn, *Tests of Lepton Universality at LHCb*, *Nucl. Part. Phys. Proc.* **287-288** (2017) 177 (cit. on p. 5).
- [23] R. Aaij et al., *Test of lepton universality with $B^0 \rightarrow K^{*0} \ell^+ \ell^-$ decays*, *JHEP* **08** (2017) 055, arXiv: [1705.05802 \[hep-ex\]](#) (cit. on p. 5).
- [24] R. Aaij et al., *Test of lepton universality using $B^+ \rightarrow K^+ \ell^+ \ell^-$ decays*, *Phys. Rev. Lett.* **113** (2014) 151601, arXiv: [1406.6482 \[hep-ex\]](#) (cit. on p. 5).
- [25] P. Alvarez-Cartelle, *Lepton universality, flavour and number violation in B and τ decays at LHCb*, *PoS CKM2016* (2017) 065 (cit. on p. 5).
- [26] F. Jegerlehner and A. Nyffeler, *The Muon g-2*, *Phys. Rept.* **477** (2009) 1, arXiv: [0902.3360 \[hep-ph\]](#) (cit. on pp. 5, 76).
- [27] R. N. Mohapatra and G. Senjanovic, *Neutrino Mass and Spontaneous Parity Nonconservation*, *Phys. Rev. Lett.* **44** (1980) 912, [,231(1979)] (cit. on p. 5).
- [28] F. Wilczek, *Problem of Strong P and T Invariance in the Presence of Instantons*, *Phys. Rev. Lett.* **40** (1978) 279 (cit. on p. 6).
- [29] S. Weinberg, *A New Light Boson?* *Phys. Rev. Lett.* **40** (1978) 223 (cit. on p. 6).
- [30] R. D. Peccei and H. R. Quinn, *CP Conservation in the Presence of Instantons*, *Phys. Rev. Lett.* **38** (1977) 1440, [,328(1977)] (cit. on p. 6).
- [31] R. D. Peccei and H. R. Quinn, *Constraints Imposed by CP Conservation in the Presence of Instantons*, *Phys. Rev.* **D16** (1977) 1791 (cit. on p. 6).

-
- [32] M. T. Frandsen et al., *LHC and Tevatron Bounds on the Dark Matter Direct Detection Cross-Section for Vector Mediators*, *JHEP* **07** (2012) 123, arXiv: 1204.3839 [hep-ph] (cit. on pp. 9, 18, 28, 29, 57).
- [33] E. Aprile, *The XENONIT Dark Matter Search Experiment*, *Springer Proc. Phys.* **148** (2013) 93, arXiv: 1206.6288 [astro-ph.IM] (cit. on pp. 11, 17).
- [34] R. Agnese et al., *Search for Low-Mass Weakly Interacting Massive Particles with SuperCDMS*, *Phys. Rev. Lett.* **112** (2014) 241302, arXiv: 1402.7137 [hep-ex] (cit. on pp. 11, 16).
- [35] R. Agnese et al., *New Results from the Search for Low-Mass Weakly Interacting Massive Particles with the CDMS Low Ionization Threshold Experiment*, *Phys. Rev. Lett.* **116** (2016) 071301, arXiv: 1509.02448 [astro-ph.CO] (cit. on pp. 11, 16).
- [36] G. Angloher et al., *Results on light dark matter particles with a low-threshold CRESST-II detector*, *Eur. Phys. J.* **C76** (2016) 25, arXiv: 1509.01515 [astro-ph.CO] (cit. on pp. 11, 16, 31).
- [37] D. S. Akerib et al., *LUX-ZEPLIN (LZ) Conceptual Design Report*, (2015), arXiv: 1509.02910 [physics.ins-det] (cit. on p. 11).
- [38] D. S. Akerib et al., *Results from a search for dark matter in the complete LUX exposure*, *Phys. Rev. Lett.* **118** (2017) 021303, arXiv: 1608.07648 [astro-ph.CO] (cit. on p. 11).
- [39] A. Tan et al., *Dark Matter Results from First 98.7 Days of Data from the PandaX-II Experiment*, *Phys. Rev. Lett.* **117** (2016) 121303, arXiv: 1607.07400 [hep-ex] (cit. on pp. 11, 31).
- [40] A. H. Abdelhameed et al., *Description of CRESST-III Data*, (2019), arXiv: 1905.07335 [astro-ph.CO] (cit. on pp. 11, 16).
- [41] A. H. Abdelhameed et al., *First results from the CRESST-III low-mass dark matter program*, (2019), arXiv: 1904.00498 [astro-ph.CO] (cit. on pp. 11, 16).
- [42] R. Agnese et al., *Search for Low-Mass Dark Matter with CDMSlite Using a Profile Likelihood Fit*, *Phys. Rev.* **D99** (2019) 062001, arXiv: 1808.09098 [astro-ph.CO] (cit. on pp. 11, 16).
- [43] R. Agnese et al., *First Dark Matter Constraints from a SuperCDMS Single-Charge Sensitive Detector*, *Phys. Rev. Lett.* **121** (2018) 051301, [erratum: *Phys. Rev. Lett.* 122,no.6,069901(2019)], arXiv: 1804.10697 [hep-ex] (cit. on pp. 11, 16).
- [44] J. Xia et al., *PandaX-II Constraints on Spin-Dependent WIMP-Nucleon Effective Interactions*, *Phys. Lett.* **B792** (2019) 193, arXiv: 1807.01936 [hep-ex] (cit. on pp. 11, 16).
- [45] V. A. Kudryavtsev, *Recent Results from LUX and Prospects for Dark Matter Searches with LZ*, *Universe* **5** (2019) 73 (cit. on pp. 11, 16, 17).
- [46] D. S. Akerib et al., *Projected WIMP Sensitivity of the LUX-ZEPLIN (LZ) Dark Matter Experiment*, (2018), arXiv: 1802.06039 [astro-ph.IM] (cit. on pp. 11, 17).

- [47] E. Aprile et al., *The XENONIT Dark Matter Experiment*, *Eur. Phys. J.* **C77** (2017) 881, arXiv: [1708.07051 \[astro-ph.IM\]](#) (cit. on pp. 11, 17).
- [48] D. S. Akerib et al., *The LUX-ZEPLIN (LZ) Experiment*, (2019), arXiv: [1910.09124 \[physics.ins-det\]](#) (cit. on pp. 11, 17).
- [49] K. Pushkin,
Direct search for WIMP dark matter particles with the LUX-ZEPLIN (LZ) detector,
Nucl. Instrum. Meth. **A936** (2019) 162 (cit. on pp. 11, 17).
- [50] E. Aprile et al., *A Search for Light Dark Matter Interactions Enhanced by the Migdal effect or Bremsstrahlung in XENONIT*, (2019), arXiv: [1907.12771 \[hep-ex\]](#) (cit. on pp. 11, 17).
- [51] E. Aprile et al.,
Constraining the spin-dependent WIMP-nucleon cross sections with XENONIT,
Phys. Rev. Lett. **122** (2019) 141301, arXiv: [1902.03234 \[astro-ph.CO\]](#)
(cit. on pp. 11, 17).
- [52] E. Aprile et al., *Light Dark Matter Search with Ionization Signals in XENONIT*, (2019), arXiv: [1907.11485 \[hep-ex\]](#) (cit. on pp. 11, 17).
- [53] E. Aprile et al., *XENONIT Dark Matter Data Analysis: Signal Reconstruction, Calibration and Event Selection*, *Phys. Rev.* **D100** (2019) 052014, arXiv: [1906.04717 \[physics.ins-det\]](#) (cit. on pp. 11, 17).
- [54] M. Aguilar et al., *Cosmic-ray positron fraction measurement from 1 to 30-GeV with AMS-01*, *Phys. Lett.* **B646** (2007) 145, arXiv: [astro-ph/0703154 \[ASTRO-PH\]](#) (cit. on pp. 11, 18).
- [55] O. Adriani et al.,
An anomalous positron abundance in cosmic rays with energies 1.5-100 GeV,
Nature **458** (2009) 607, arXiv: [0810.4995 \[astro-ph\]](#) (cit. on pp. 11, 18).
- [56] D. Hooper, P. Blasi, and P. D. Serpico,
Pulsars as the Sources of High Energy Cosmic Ray Positrons, *JCAP* **0901** (2009) 025, arXiv: [0810.1527 \[astro-ph\]](#) (cit. on p. 11).
- [57] G. Bertone et al., *Gamma-ray and radio tests of the $e+e-$ excess from DM annihilations*, *JCAP* **0903** (2009) 009, arXiv: [0811.3744 \[astro-ph\]](#) (cit. on p. 11).
- [58] S. Galli et al., *CMB constraints on Dark Matter models with large annihilation cross-section*, *Phys. Rev.* **D80** (2009) 023505, arXiv: [0905.0003 \[astro-ph.CO\]](#) (cit. on p. 11).
- [59] M. Ackermann et al., *Measurement of separate cosmic-ray electron and positron spectra with the Fermi Large Area Telescope*, *Phys. Rev. Lett.* **108** (2012) 011103, arXiv: [1109.0521 \[astro-ph.HE\]](#) (cit. on pp. 11, 18).
- [60] M. G. Aartsen et al.,
Search for dark matter annihilations in the Sun with the 79-string IceCube detector,
Phys. Rev. Lett. **110** (2013) 131302, arXiv: [1212.4097 \[astro-ph.HE\]](#) (cit. on pp. 11, 18).
- [61] S. Adrian-Martinez et al.,
First results on dark matter annihilation in the Sun using the ANTARES neutrino telescope,
JCAP **1311** (2013) 032, arXiv: [1302.6516 \[astro-ph.HE\]](#) (cit. on pp. 11, 18).

- [62] M. Aguilar et al., *First Result from the Alpha Magnetic Spectrometer on the International Space Station: Precision Measurement of the Positron Fraction in Primary Cosmic Rays of 0.5–350 GeV*, *Phys. Rev. Lett.* **110** (2013) 141102 (cit. on pp. 11, 18).
- [63] M. Ackermann et al., *Search for Gamma-ray Spectral Lines with the Fermi Large Area Telescope and Dark Matter Implications*, *Phys. Rev.* **D88** (2013) 082002, arXiv: 1305.5597 [astro-ph.HE] (cit. on pp. 11, 18).
- [64] M. Ackermann et al., *Searching for Dark Matter Annihilation from Milky Way Dwarf Spheroidal Galaxies with Six Years of Fermi Large Area Telescope Data*, *Phys. Rev. Lett.* **115** (2015) 231301, arXiv: 1503.02641 [astro-ph.HE] (cit. on pp. 11, 18).
- [65] A. Drlica-Wagner et al., *Search for Gamma-Ray Emission from DES Dwarf Spheroidal Galaxy Candidates with Fermi-LAT Data*, *Astrophys. J.* **809** (2015) L4, arXiv: 1503.02632 [astro-ph.HE] (cit. on pp. 11, 18).
- [66] M. Ajello et al., *A Search for Cosmic-ray Proton Anisotropy with the Fermi Large Area Telescope*, (2019), arXiv: 1903.02905 [astro-ph.HE] (cit. on pp. 11, 18).
- [67] H. Niederhausen, “Recent IceCube Measurements Using High Energy Neutrinos,” *18th Conference on Elastic and Diffractive Scattering (EDS Blois 2019) Quy Nhon, Vietnam, June 23-29, 2019*, 2019, arXiv: 1909.12182 [astro-ph.HE] (cit. on pp. 11, 18).
- [68] D. Soldin, “Recent Results of Cosmic Ray Measurements from IceCube and IceTop,” *HAWC Contributions to the 36th International Cosmic Ray Conference (ICRC2019)*, 2019, arXiv: 1909.04423 [astro-ph.HE] (cit. on pp. 11, 18).
- [69] C. Tönnis, *Indirect searches for dark matter with the ANTARES neutrino telescope*, *PoS ICHEP2018* (2019) 840 (cit. on pp. 11, 18).
- [70] A. Sánchez Losa, *Latest results on high-energy cosmic neutrino searches with the ANTARES neutrino telescope*, *EPJ Web Conf.* **210** (2019) 03004 (cit. on pp. 11, 18).
- [71] O. Buchmueller, M. J. Dolan, and C. McCabe, *Beyond Effective Field Theory for Dark Matter Searches at the LHC*, *JHEP* **01** (2014) 025, arXiv: 1308.6799 [hep-ph] (cit. on p. 11).
- [72] V. Khachatryan et al., *Search for dark matter, extra dimensions, and unparticles in monojet events in proton–proton collisions at $\sqrt{s} = 8$ TeV*, *Eur. Phys. J.* **C75** (2015) 235, arXiv: 1408.3583 [hep-ex] (cit. on pp. 11, 35).
- [73] G. Aad et al., *Search for new particles in events with one lepton and missing transverse momentum in pp collisions at $\sqrt{s} = 8$ TeV with the ATLAS detector*, *JHEP* **09** (2014) 037, arXiv: 1407.7494 [hep-ex] (cit. on p. 11).
- [74] G. Aad et al., *Search for new phenomena in events with a photon and missing transverse momentum in pp collisions at $\sqrt{s} = 8$ TeV with the ATLAS detector*, *Phys. Rev.* **D91** (2015) 012008, [Erratum: *Phys. Rev.* D92, no.5, 059903(2015)], arXiv: 1411.1559 [hep-ex] (cit. on p. 11).

- [75] V. Khachatryan et al., *Search for new phenomena in monophoton final states in proton-proton collisions at $\sqrt{s} = 8$ TeV*, *Phys. Lett.* **B755** (2016) 102, arXiv: [1410.8812 \[hep-ex\]](#) (cit. on p. 11).
- [76] V. Khachatryan et al., *Search for physics beyond the standard model in final states with a lepton and missing transverse energy in proton-proton collisions at $\sqrt{s} = 8$ TeV*, *Phys. Rev.* **D91** (2015) 092005, arXiv: [1408.2745 \[hep-ex\]](#) (cit. on p. 11).
- [77] G. Aad et al., *Search for new phenomena in final states with an energetic jet and large missing transverse momentum in pp collisions at $\sqrt{s} = 8$ TeV with the ATLAS detector*, *Eur. Phys. J.* **C75** (2015) 299, [Erratum: *Eur. Phys. J.*C75,no.9,408(2015)], arXiv: [1502.01518 \[hep-ex\]](#) (cit. on p. 11).
- [78] G. Aad et al., *Search for Dark Matter in Events with Missing Transverse Momentum and a Higgs Boson Decaying to Two Photons in pp Collisions at $\sqrt{s} = 8$ TeV with the ATLAS Detector*, *Phys. Rev. Lett.* **115** (2015) 131801, arXiv: [1506.01081 \[hep-ex\]](#) (cit. on p. 11).
- [79] G. Aad et al., *Search for dark matter produced in association with a Higgs boson decaying to two bottom quarks in pp collisions at $\sqrt{s} = 8$ TeV with the ATLAS detector*, *Phys. Rev.* **D93** (2016) 072007, arXiv: [1510.06218 \[hep-ex\]](#) (cit. on p. 11).
- [80] G. Busoni et al., *Recommendations on presenting LHC searches for missing transverse energy signals using simplified s -channel models of dark matter*, (2016), ed. by A. Boveia et al., arXiv: [1603.04156 \[hep-ex\]](#) (cit. on pp. 11, 27).
- [81] V. C. Rubin and W. K. Ford Jr., *Rotation of the Andromeda Nebula from a Spectroscopic Survey of Emission Regions*, *Astrophys. J.* **159** (1970) 379 (cit. on p. 12).
- [82] T. S. van Albada et al., *The Distribution of Dark Matter in the Spiral Galaxy NGC-3198*, *Astrophys. J.* **295** (1985) 305 (cit. on p. 12).
- [83] K. G. Begeman, A. H. Broeils, and R. H. Sanders, *Extended rotation curves of spiral galaxies - Dark haloes and modified dynamics*, **249** (1991) 523 (cit. on p. 12).
- [84] J. Bekenstein and M. Milgrom, *Does the missing mass problem signal the breakdown of Newtonian gravity?* *Astrophys. J.* **286** (1984) 7 (cit. on p. 12).
- [85] E. Corbelli and P. Salucci, *The Extended Rotation Curve and the Dark Matter Halo of M33*, *Mon. Not. Roy. Astron. Soc.* **311** (2000) 441, arXiv: [astro-ph/9909252 \[astro-ph\]](#) (cit. on p. 21).
- [86] D. Clowe et al., *A direct empirical proof of the existence of dark matter*, *Astrophys. J.* **648** (2006) L109, arXiv: [astro-ph/0608407 \[astro-ph\]](#) (cit. on p. 12).
- [87] D. Clowe, A. Gonzalez, and M. Markevitch, *Weak lensing mass reconstruction of the interacting cluster 1E0657-558: Direct evidence for the existence of dark matter*, *Astrophys. J.* **604** (2004) 596, arXiv: [astro-ph/0312273 \[astro-ph\]](#) (cit. on p. 12).
- [88] F. Zwicky, *Die Rotverschiebung von extragalaktischen Nebeln*, *Helv. Phys. Acta* **6** (1933) 110, [Gen. Rel. Grav.41,207(2009)] (cit. on p. 14).

- [89] C. L. Bennett et al., *Four-Year [ITAL]COBE[/ITAL] DMR Cosmic Microwave Background Observations: Maps and Basic Results*, *The Astrophysical Journal* **464** (1996) L1, URL: <https://doi.org/10.1086%2F310075> (cit. on p. 15).
- [90] P. A. R. Ade et al., *Planck 2013 results. XVI. Cosmological parameters*, *Astron. Astrophys.* **571** (2014) A16, arXiv: 1303.5076 [astro-ph.CO] (cit. on pp. 15, 22).
- [91] C. L. Bennett et al., *NINE-YEAR WILKINSON MICROWAVE ANISOTROPY PROBE (WMAP) OBSERVATIONS: FINAL MAPS AND RESULTS*, *The Astrophysical Journal Supplement Series* **208** (2013) 20, URL: <https://doi.org/10.1088%2F0067-0049%2F208%2F2%2F20> (cit. on p. 22).
- [92] E. W. Kolb and M. S. Turner, *The Early Universe*, *Front. Phys.* **69** (1990) 1 (cit. on pp. 16, 28, 29).
- [93] N. Aghanim et al., *Planck 2018 results. VI. Cosmological parameters*, (2018), arXiv: 1807.06209 [astro-ph.CO] (cit. on p. 16).
- [94] D. S. Akerib et al., *First results from the LUX dark matter experiment at the Sanford Underground Research Facility*, *Phys. Rev. Lett.* **112** (2014) 091303, arXiv: 1310.8214 [astro-ph.CO] (cit. on p. 16).
- [95] M. Schumann, *Direct Detection of WIMP Dark Matter: Concepts and Status*, *J. Phys.* **G46** (2019) 103003, arXiv: 1903.03026 [astro-ph.CO] (cit. on p. 17).
- [96] C. Fu et al., *Spin-Dependent Weakly-Interacting-Massive-Particle-Nucleon Cross Section Limits from First Data of PandaX-II Experiment*, *Phys. Rev. Lett.* **118** (2017) 071301, [Erratum: *Phys. Rev. Lett.* 120, no. 4, 049902 (2018)], arXiv: 1611.06553 [hep-ex] (cit. on p. 17).
- [97] A. Alloul et al., *FeynRules 2.0 - A complete toolbox for tree-level phenomenology*, *Comput. Phys. Commun.* **185** (2014) 2250, arXiv: 1310.1921 [hep-ph] (cit. on pp. 18, 33, 59, 75).
- [98] J. Alwall et al., *MadGraph 5: going beyond*, *Journal of High Energy Physics* **2011** (2011) 1 (cit. on pp. 19, 29, 33, 59, 75).
- [99] T. Sjöstrand et al., *An introduction to PYTHIA 8.2*, *Computer Physics Communications* **191** (2015) 159 (cit. on pp. 19, 33, 41, 59, 75).
- [100] J. de Favereau et al., *DELPHES 3, A modular framework for fast simulation of a generic collider experiment*, *JHEP* **02** (2014) 057, arXiv: 1307.6346 [hep-ex] (cit. on pp. 19, 59, 74).
- [101] D. Dercks et al., *CheckMATE 2: From the model to the limit*, *Comput. Phys. Commun.* **221** (2017) 383, arXiv: 1611.09856 [hep-ph] (cit. on pp. 19, 59, 70, 74, 75).
- [102] J. L. Feng, *Dark matter candidates from particle physics and methods of detection*, arXiv preprint arXiv:1003.0904 (2010) (cit. on p. 27).
- [103] S. Banerjee et al., *WIMP Dark Matter in a Well-Tempered Regime: A case study on Singlet-Doublets Fermionic WIMP*, *JHEP* **11** (2016) 070, arXiv: 1603.07387 [hep-ph] (cit. on p. 27).

- [104] M. Hoferichter et al., *Improved limits for Higgs-portal dark matter from LHC searches*, *Phys. Rev. Lett.* **119** (2017) 181803, arXiv: 1708.02245 [hep-ph] (cit. on p. 27).
- [105] P. Athron et al., *Status of the scalar singlet dark matter model*, *Eur. Phys. J.* **C77** (2017) 568, arXiv: 1705.07931 [hep-ph] (cit. on p. 27).
- [106] A. DiFranzo et al., *Simplified Models for Dark Matter Interacting with Quarks*, *JHEP* **11** (2013) 014, [Erratum: JHEP01,162(2014)], arXiv: 1308.2679 [hep-ph] (cit. on p. 27).
- [107] J. Abdallah et al., *Simplified Models for Dark Matter Searches at the LHC*, *Phys. Dark Univ.* **9-10** (2015) 8, arXiv: 1506.03116 [hep-ph] (cit. on p. 27).
- [108] M. Aaboud et al., *Search for dark matter and other new phenomena in events with an energetic jet and large missing transverse momentum using the ATLAS detector*, *JHEP* **01** (2018) 126, arXiv: 1711.03301 [hep-ex] (cit. on pp. 27, 57, 59, 63–65).
- [109] A. M. Sirunyan et al., *Search for dark matter produced with an energetic jet or a hadronically decaying W or Z boson at $\sqrt{s} = 13$ TeV*, *JHEP* **07** (2017) 014, arXiv: 1703.01651 [hep-ex] (cit. on pp. 27, 57, 64, 65).
- [110] A. M. Sirunyan et al., *Search for dijet resonances in proton-proton collisions at $\sqrt{s} = 13$ TeV and constraints on dark matter and other models*, *Phys. Lett.* **B769** (2017) 520, [Erratum: Phys. Lett.B772,882(2017)], arXiv: 1611.03568 [hep-ex] (cit. on pp. 27, 57).
- [111] M. Aaboud et al., *Search for new phenomena in dijet events using 37 fb^{-1} of pp collision data collected at $\sqrt{s} = 13$ TeV with the ATLAS detector*, *Phys. Rev.* **D96** (2017) 052004, arXiv: 1703.09127 [hep-ex] (cit. on pp. 27, 57, 65).
- [112] M. Aaboud et al., *Search for low-mass dijet resonances using trigger-level jets with the ATLAS detector in pp collisions at $\sqrt{s}=13$ TeV*, (2018), arXiv: 1804.03496 [hep-ex] (cit. on p. 27).
- [113] M. Bauce, “Search for new physics in dijet final states in ATLAS and CMS,” *5th Large Hadron Collider Physics Conference (LHCP 2017) Shanghai, China, May 15-20, 2017*, 2017, arXiv: 1709.04754 [hep-ex], URL: <http://inspirehep.net/record/1623560/files/arXiv:1709.04754.pdf> (cit. on p. 27).
- [114] K. S. Babu, C. F. Kolda, and J. March-Russell, *Implications of generalized Z - Z-prime mixing*, *Phys. Rev.* **D57** (1998) 6788, arXiv: hep-ph/9710441 [hep-ph] (cit. on p. 27).
- [115] E. Dudas et al., *(In)visible Z-prime and dark matter*, *JHEP* **08** (2009) 014, arXiv: 0904.1745 [hep-ph] (cit. on p. 27).
- [116] E. Accomando et al., *Z-prime physics with early LHC data*, *Phys. Rev.* **D83** (2011) 075012, arXiv: 1010.6058 [hep-ph] (cit. on p. 27).
- [117] P. J. Fox et al., *An Effective Z-prime*, *Phys. Rev.* **D84** (2011) 115006, arXiv: 1104.4127 [hep-ph] (cit. on p. 27).
- [118] M. T. Frandsen et al., *Direct detection of dark matter in models with a light Z-prime*, *JHEP* **09** (2011) 128, arXiv: 1107.2118 [hep-ph] (cit. on p. 27).

- [119] A. Alves, S. Profumo, and F. S. Queiroz, *The dark Z portal: direct, indirect and collider searches*, *JHEP* **04** (2014) 063, arXiv: [1312.5281 \[hep-ph\]](#) (cit. on p. 27).
- [120] G. Jungman, M. Kamionkowski, and K. Griest, *Supersymmetric dark matter*, *Physics Reports* **267** (1996) 195 (cit. on p. 27).
- [121] A. Kvellestad, “First SUSY results with GAMBIT,” *2017 European Physical Society Conference on High Energy Physics (EPS-HEP 2017) Venice, Italy, July 5-12, 2017*, 2017, arXiv: [1710.02503 \[hep-ph\]](#), URL: <http://inspirehep.net/record/1628996/files/arXiv:1710.02503.pdf> (cit. on p. 27).
- [122] E. Bagnaschi et al., *Likelihood Analysis of the pMSSM11 in Light of LHC 13-TeV Data*, (2017), arXiv: [1710.11091 \[hep-ph\]](#) (cit. on p. 27).
- [123] F. Kahlhoefer et al., *Implications of unitarity and gauge invariance for simplified dark matter models*, *JHEP* **02** (2016) 016, arXiv: [1510.02110 \[hep-ph\]](#) (cit. on pp. 28, 32).
- [124] D. Decamp et al., *ALEPH: A detector for electron-positron annihilations at LEP*, *Nucl. Instrum. Meth. A* **294** (1990) 121, [Erratum: *Nucl. Instrum. Meth. A* 303,393(1991)] (cit. on pp. 28, 33).
- [125] D. Buskulic et al., *Performance of the ALEPH detector at LEP*, *Nucl. Instrum. Meth. A* **360** (1995) 481 (cit. on pp. 28, 33).
- [126] M. Chala et al., *Constraining Dark Sectors with Monojets and Dijets*, *JHEP* **07** (2015) 089, arXiv: [1503.05916 \[hep-ph\]](#) (cit. on pp. 30, 35).
- [127] C. Patrignani et al., *Review of Particle Physics*, *Chin. Phys.* **C40** (2016) 100001 (cit. on p. 31).
- [128] C. Amole et al., *Dark Matter Search Results from the PICO-60 C₃F₈ Bubble Chamber*, *Phys. Rev. Lett.* **118** (2017) 251301, arXiv: [1702.07666 \[astro-ph.CO\]](#) (cit. on p. 31).
- [129] C. Degrande et al., *UFO - The Universal FeynRules Output*, *Comput. Phys. Commun.* **183** (2012) 1201, arXiv: [1108.2040 \[hep-ph\]](#) (cit. on pp. 33, 59, 75).
- [130] R. Barate et al., *Searches for sleptons and squarks in e⁺e⁻ collisions...*, *Physics Letters B* **469** (1999) 303 (cit. on p. 34).
- [131] A. Heister et al., *Search for stable hadronizing squarks and gluinos in e⁺e⁻ collisions up to...*, *Eur. Phys. J. C* **31** (2003) 327 (cit. on pp. 34, 35, 42).
- [132] R. Barate et al., *Searches for charginos and neutralinos in e⁺e⁻ collisions at $\sqrt{s} = 161\text{-GeV}$ and 172-GeV* , *Eur. Phys. J. C* **2** (1998) 417, arXiv: [hep-ex/9710012 \[hep-ex\]](#) (cit. on pp. 34, 35, 41).
- [133] R. Barate et al., *Search for charginos and neutralinos in e⁺e⁻ collisions...*, *Eur. Phys. J. C* **11** (1999) 193 (cit. on pp. 34, 35).
- [134] R. Barate et al., *Search for supersymmetric particles in e⁺e⁻ collisions at \sqrt{s} up to 202-GeV and mass limit for the lightest neutralino*, *Phys. Lett. B* **499** (2001) 67, arXiv: [hep-ex/0011047 \[hep-ex\]](#) (cit. on pp. 34, 35).

- [135] G. Abbiendi, O. Collaboration, et al.,
Search for chargino and neutralino production at $\sqrt{s}=189$ GeV at LEP,
The European Physical Journal C-Particles and Fields **14** (2000) 187 (cit. on pp. 34, 35).
- [136] A. Heister et al., *Absolute mass lower limit for the lightest neutralino of the MSSM...*,
Phys. Lett. **B583** (2004) 247 (cit. on pp. 34, 35).
- [137] R. Barate et al., *Search for invisible Higgs boson decays in e^+e^- collisions...*,
Physics Letters B **450** (1999) 301 (cit. on pp. 34, 35).
- [138] M. Acciarri et al., *Missing mass spectra in hadronic events from e^+e^- collisions ...*,
Physics Letters B **418** (1998) 389 (cit. on pp. 34, 35).
- [139] R. Barate et al., *Search for an invisibly decaying Higgs boson in e^+e^- collisions at 189-GeV*,
Phys. Lett. **B466** (1999) 50 (cit. on pp. 34, 35).
- [140] P. J. Fox et al., *Missing Energy Signatures of Dark Matter at the LHC*,
Phys. Rev. **D85** (2012) 056011, arXiv: 1109.4398 [hep-ph] (cit. on p. 35).
- [141] D. Decamp et al., *Searches for new particles in Z decays using the ALEPH detector*,
Phys. Rept. **216** (1992) 253 (cit. on pp. 37, 38, 40).
- [142] D. Buskulic et al.,
Mass limit for the standard model Higgs boson with the full LEP-1 ALEPH data sample,
Phys. Lett. **B384** (1996) 427 (cit. on pp. 37, 38).
- [143] D. Buskulic et al., *Four jet final state production in e^+e^- collisions at center-of-mass energies of 130-GeV and 136-GeV*, *Z. Phys.* **C71** (1996) 179 (cit. on p. 39).
- [144] R. Barate et al., *Four jet final state production in e^+e^- collisions at center-of-mass energies ranging from 130-GeV to 184-GeV*, *Phys. Lett.* **B420** (1998) 196 (cit. on p. 39).
- [145] R. Barate et al., *Search for the neutral Higgs bosons of the MSSM in e^+e^- collisions at \sqrt{s} from 130-GeV to 172-GeV*, *Phys. Lett.* **B412** (1997) 173 (cit. on p. 39).
- [146] R. Barate et al., *Search for the Standard Model Higgs boson in e^+e^- collisions at $\sqrt{s} = 161$ -GeV, 170-GeV and 172-GeV*, *Phys. Lett.* **B412** (1997) 155 (cit. on p. 39).
- [147] R. Barate et al.,
Search for the standard model Higgs boson at the LEP-2 collider near $\sqrt{s} = 183$ -GeV,
Phys. Lett. **B440** (1998) 403, [Phys. Lett.B447,336(1999)],
arXiv: hep-ex/9811032 [hep-ex] (cit. on p. 39).
- [148] R. Barate et al., *Search for the neutral Higgs bosons of the standard model and the MSSM in e^+e^- collisions at $\sqrt{s} = 189$ -GeV*, *Eur. Phys. J.* **C17** (2000) 223 (cit. on p. 39).
- [149] J. Nielsen, "Search for neutral Higgs bosons in e^+e^- collisions at \sqrt{s} less than = 196-GeV,"
Lepton and photon interactions at high energies. Proceedings, 19th International Symposium, LP'99, Stanford, USA, August 9-14, 1999, 1999, arXiv: hep-ex/9908016 [hep-ex],
URL: http://inspirehep.net/record/505113/files/arXiv:hep-ex_9908016.pdf
(cit. on p. 39).
- [150] R. Barate et al., *Searches for neutral Higgs bosons in e^+e^- collisions at center-of-mass energies from 192-GeV to 202-GeV*, *Phys. Lett.* **B499** (2001) 53,
arXiv: hep-ex/0010062 [hep-ex] (cit. on p. 39).

-
- [151] R. Barate et al., *Observation of an excess in the search for the standard model Higgs boson at ALEPH*, *Phys. Lett.* **B495** (2000) 1, arXiv: [hep-ex/0011045 \[hep-ex\]](#) (cit. on p. 39).
- [152] A. Heister et al., *Final results of the searches for neutral Higgs bosons in e^+e^- collisions at \sqrt{s} up to 209-GeV*, *Phys. Lett.* **B526** (2002) 191, arXiv: [hep-ex/0201014 \[hep-ex\]](#) (cit. on p. 39).
- [153] D. Decamp et al., *Search for the neutral Higgs bosons of the MSSM and other two doublet models*, *Phys. Lett.* **B265** (1991) 475 (cit. on p. 40).
- [154] M. Duerr and P. Fileviez Perez, *Theory for Baryon Number and Dark Matter at the LHC*, *Phys. Rev.* **D91** (2015) 095001, arXiv: [1409.8165 \[hep-ph\]](#) (cit. on p. 54).
- [155] V. Khachatryan et al., *Search for heavy resonances decaying to tau lepton pairs in proton-proton collisions at $\sqrt{s} = 13$ TeV*, *JHEP* **02** (2017) 048, arXiv: [1611.06594 \[hep-ex\]](#) (cit. on p. 57).
- [156] M. Aaboud et al., *Search for new high-mass phenomena in the dilepton final state using 36 fb^{-1} of proton-proton collision data at $\sqrt{s} = 13$ TeV with the ATLAS detector*, *JHEP* **10** (2017) 182, arXiv: [1707.02424 \[hep-ex\]](#) (cit. on pp. 57, 69).
- [157] M. Aaboud et al., *Search for additional heavy neutral Higgs and gauge bosons in the ditau final state produced in 36 fb^{-1} of pp collisions at $\sqrt{s} = 13$ TeV with the ATLAS detector*, *JHEP* **01** (2018) 055, arXiv: [1709.07242 \[hep-ex\]](#) (cit. on pp. 57, 74).
- [158] A. M. Sirunyan et al., *Search for high-mass resonances in dilepton final states in proton-proton collisions at $\sqrt{s} = 13$ TeV*, *JHEP* **06** (2018) 120, arXiv: [1803.06292 \[hep-ex\]](#) (cit. on pp. 57, 69, 74).
- [159] J. R. Ellis and R. A. Flores, *Elastic supersymmetric relic - nucleus scattering revisited*, *Phys. Lett.* **B263** (1991) 259 (cit. on p. 57).
- [160] M. Aaboud et al., *Search for squarks and gluinos in final states with jets and missing transverse momentum using 36 fb^{-1} of $\sqrt{s} = 13$ TeV pp collision data with the ATLAS detector*, *Phys. Rev.* **D97** (2018) 112001, arXiv: [1712.02332 \[hep-ex\]](#) (cit. on pp. 59, 62).
- [161] M. Aaboud et al., *Search for a scalar partner of the top quark in the jets plus missing transverse momentum final state at $\sqrt{s}=13$ TeV with the ATLAS detector*, *JHEP* **12** (2017) 085, arXiv: [1709.04183 \[hep-ex\]](#) (cit. on pp. 59, 63).
- [162] T. A. collaboration, *Search for squarks and gluinos in events with an isolated lepton, jets and missing transverse momentum at $\sqrt{s} = 13$ TeV with the ATLAS detector*, (2016) (cit. on p. 59).
- [163] M. Aaboud et al., *Search for large missing transverse momentum in association with one top-quark in proton-proton collisions at $\sqrt{s} = 13$ TeV with the ATLAS detector*, *JHEP* **05** (2019) 041, arXiv: [1812.09743 \[hep-ex\]](#) (cit. on pp. 59, 63).
- [164] M. Aaboud et al., *Search for supersymmetry in events with b-tagged jets and missing transverse momentum in pp collisions at $\sqrt{s} = 13$ TeV with the ATLAS detector*, *JHEP* **11** (2017) 195, arXiv: [1708.09266 \[hep-ex\]](#) (cit. on pp. 59, 62).

- [165] M. Aaboud et al., *Search for resonances in the mass distribution of jet pairs with one or two jets identified as b-jets in proton-proton collisions at $\sqrt{s} = 13$ TeV with the ATLAS detector*, *Phys. Rev.* **D98** (2018) 032016, arXiv: 1805.09299 [hep-ex] (cit. on pp. 59, 61, 62).
- [166] A. M. Sirunyan et al., *Search for $t\bar{t}$ resonances in highly boosted lepton+jets and fully hadronic final states in proton-proton collisions at $\sqrt{s} = 13$ TeV*, *JHEP* **07** (2017) 001, arXiv: 1704.03366 [hep-ex] (cit. on pp. 59, 61).
- [167] M. Drees et al., *CheckMATE: Confronting your Favourite New Physics Model with LHC Data*, *Comput. Phys. Commun.* **187** (2015) 227, arXiv: 1312.2591 [hep-ph] (cit. on pp. 59, 70).
- [168] M. Cacciari, G. P. Salam, and G. Soyez, *FastJet User Manual*, *Eur. Phys. J.* **C72** (2012) 1896, arXiv: 1111.6097 [hep-ph] (cit. on pp. 59, 74).
- [169] M. Cacciari and G. P. Salam, *Dispelling the N^3 myth for the k_t jet-finder*, *Phys. Lett.* **B641** (2006) 57, arXiv: hep-ph/0512210 [hep-ph] (cit. on pp. 59, 74).
- [170] M. Cacciari, G. P. Salam, and G. Soyez, *The anti- k_t jet clustering algorithm*, *JHEP* **04** (2008) 063, arXiv: 0802.1189 [hep-ph] (cit. on pp. 59, 74).
- [171] A. L. Read, *Presentation of search results: The $CL(s)$ technique*, *J. Phys.* **G28** (2002) 2693, [11(2002)] (cit. on pp. 59, 74).
- [172] C. G. Lester and D. J. Summers, *Measuring masses of semiinvisibly decaying particles pair produced at hadron colliders*, *Phys. Lett.* **B463** (1999) 99, arXiv: hep-ph/9906349 [hep-ph] (cit. on pp. 59, 74).
- [173] A. Barr, C. Lester, and P. Stephens, *$m(T2)$: The Truth behind the glamour*, *J. Phys.* **G29** (2003) 2343, arXiv: hep-ph/0304226 [hep-ph] (cit. on pp. 59, 74).
- [174] H.-C. Cheng and Z. Han, *Minimal Kinematic Constraints and $m(T2)$* , *JHEP* **12** (2008) 063, arXiv: 0810.5178 [hep-ph] (cit. on pp. 59, 74).
- [175] Y. Bai et al., *Stop the Top Background of the Stop Search*, *JHEP* **07** (2012) 110, arXiv: 1203.4813 [hep-ph] (cit. on pp. 59, 74).
- [176] D. R. Tovey, *On measuring the masses of pair-produced semi-invisibly decaying particles at hadron colliders*, *JHEP* **04** (2008) 034, arXiv: 0802.2879 [hep-ph] (cit. on pp. 59, 74).
- [177] G. Polesello and D. R. Tovey, *Supersymmetric particle mass measurement with the boost-corrected contranverse mass*, *JHEP* **03** (2010) 030, arXiv: 0910.0174 [hep-ph] (cit. on pp. 59, 74).
- [178] K. T. Matchev and M. Park, *A General method for determining the masses of semi-invisibly decaying particles at hadron colliders*, *Phys. Rev. Lett.* **107** (2011) 061801, arXiv: 0910.1584 [hep-ph] (cit. on pp. 59, 74).
- [179] M. L. Mangano et al., *Matching matrix elements and shower evolution for top-quark production in hadronic collisions*, *JHEP* **01** (2007) 013, arXiv: hep-ph/0611129 [hep-ph] (cit. on p. 60).
- [180] M. Aaboud et al., *Search for light resonances decaying to boosted quark pairs and produced in association with a photon or a jet in proton-proton collisions at $\sqrt{s} = 13$ TeV with the ATLAS detector*, *Phys. Lett.* **B788** (2019) 316, arXiv: 1801.08769 [hep-ex] (cit. on p. 65).

-
- [181] A. M. Sirunyan et al., *Search for low mass vector resonances decaying into quark-antiquark pairs in proton-proton collisions at $\sqrt{s} = 13$ TeV*, *JHEP* **01** (2018) 097, arXiv: 1710.00159 [hep-ex] (cit. on p. 65).
- [182] R. N. Mohapatra and R. E. Marshak, *Local B-L Symmetry of Electroweak Interactions, Majorana Neutrinos and Neutron Oscillations*, *Phys. Rev. Lett.* **44** (1980) 1316, [Erratum: *Phys. Rev. Lett.* 44,1643(1980)] (cit. on p. 69).
- [183] X. G. He et al., *NEW Z-prime PHENOMENOLOGY*, *Phys. Rev.* **D43** (1991) 22 (cit. on p. 69).
- [184] S. Amrith et al., *LHC Constraints on a B – L Gauge Model using Contur*, (2018), arXiv: 1811.11452 [hep-ph] (cit. on p. 69).
- [185] S. Schael et al., *Fermion pair production in e^+e^- collisions at 189-209-GeV and constraints on physics beyond the standard model*, *Eur. Phys. J.* **C49** (2007) 411, arXiv: hep-ex/0609051 [hep-ex] (cit. on p. 70).
- [186] G. Abbiendi et al., *Tests of the standard model and constraints on new physics from measurements of fermion pair production at 189-GeV to 209-GeV at LEP*, *Eur. Phys. J.* **C33** (2004) 173, arXiv: hep-ex/0309053 [hep-ex] (cit. on p. 70).
- [187] E. Ma, D. P. Roy, and S. Roy, *Gauged L(mu) - L(tau) with large muon anomalous magnetic moment and the bimaximal mixing of neutrinos*, *Phys. Lett.* **B525** (2002) 101, arXiv: hep-ph/0110146 [hep-ph] (cit. on pp. 70, 76).
- [188] K. Asai, K. Hamaguchi, and N. Nagata, *Predictions for the neutrino parameters in the minimal gauged $U(1)_{L_\mu-L_\tau}$ model*, *Eur. Phys. J.* **C77** (2017) 763, arXiv: 1705.00419 [hep-ph] (cit. on p. 70).
- [189] K. Asai et al., *Minimal Gauged $U(1)_{L_\alpha-L_\beta}$ Models Driven into a Corner*, *Phys. Rev.* **D99** (2019) 055029, arXiv: 1811.07571 [hep-ph] (cit. on p. 70).
- [190] A. Biswas, S. Choubey, and S. Khan, *Neutrino Mass, Dark Matter and Anomalous Magnetic Moment of Muon in a $U(1)_{L_\mu-L_\tau}$ Model*, *JHEP* **09** (2016) 147, arXiv: 1608.04194 [hep-ph] (cit. on pp. 70, 71, 76).
- [191] A. Biswas, S. Choubey, and S. Khan, *FIMP and Muon ($g - 2$) in a $U(1)_{L_\mu-L_\tau}$ Model*, *JHEP* **02** (2017) 123, arXiv: 1612.03067 [hep-ph] (cit. on pp. 70, 71, 76).
- [192] W. Altmannshofer et al., *Neutrino Trident Production: A Powerful Probe of New Physics with Neutrino Beams*, *Phys. Rev. Lett.* **113** (2014) 091801, arXiv: 1406.2332 [hep-ph] (cit. on pp. 70, 72, 76).
- [193] J. L. Rainbolt and M. Schmitt, *Branching fraction for Z decays to four leptons and constraints on new physics*, (2018), arXiv: 1805.05791 [hep-ex] (cit. on p. 70).
- [194] A. M. Sirunyan et al., *Search for an $L_\mu - L_\tau$ gauge boson using $Z \rightarrow 4\mu$ events in proton-proton collisions at $\sqrt{s} = 13$ TeV*, Submitted to: *Phys. Lett.* (2018), arXiv: 1808.03684 [hep-ex] (cit. on pp. 70, 74, 76–78).
- [195] K. Harigaya et al., *Muon $g-2$ and LHC phenomenology in the $L_\mu - L_\tau$ gauge symmetric model*, *JHEP* **03** (2014) 105, arXiv: 1311.0870 [hep-ph] (cit. on p. 70).

- [196] F. del Aguila et al., *Collider limits on leptophilic interactions*, *JHEP* **03** (2015) 059, arXiv: [1411.7394 \[hep-ph\]](#) (cit. on p. 70).
- [197] F. Elahi and A. Martin, *Constraints on $L_\mu - L_\tau$ interactions at the LHC and beyond*, *Phys. Rev.* **D93** (2016) 015022, arXiv: [1511.04107 \[hep-ph\]](#) (cit. on p. 70).
- [198] F. Capozzi et al., *Neutrino masses and mixings: Status of known and unknown 3ν parameters*, *Nucl. Phys.* **B908** (2016) 218, arXiv: [1601.07777 \[hep-ph\]](#) (cit. on p. 72).
- [199] P. A. R. Ade et al., *Planck 2015 results. XIII. Cosmological parameters*, *Astron. Astrophys.* **594** (2016) A13, arXiv: [1502.01589 \[astro-ph.CO\]](#) (cit. on p. 72).
- [200] F. Calore et al., *A Tale of Tails: Dark Matter Interpretations of the Fermi GeV Excess in Light of Background Model Systematics*, *Phys. Rev.* **D91** (2015) 063003, arXiv: [1411.4647 \[hep-ph\]](#) (cit. on p. 72).
- [201] S. Chatrchyan et al., *The CMS Experiment at the CERN LHC*, *JINST* **3** (2008) S08004 (cit. on p. 74).
- [202] G. Aad et al., *The ATLAS Experiment at the CERN Large Hadron Collider*, *JINST* **3** (2008) S08003 (cit. on p. 74).
- [203] V. Khachatryan et al., *Search for a standard model-like Higgs boson in the $\mu^+\mu^-$ and e^+e^- decay channels at the LHC*, *Phys. Lett.* **B744** (2015) 184, arXiv: [1410.6679 \[hep-ex\]](#) (cit. on p. 74).
- [204] S. Chatrchyan et al., *Measurement of the W^+W^- Cross section in pp Collisions at $\sqrt{s} = 7$ TeV and Limits on Anomalous $WW\gamma$ and WWZ couplings*, *Eur. Phys. J.* **C73** (2013) 2610, arXiv: [1306.1126 \[hep-ex\]](#) (cit. on p. 74).
- [205] V. Khachatryan et al., *Measurement of the transverse momentum spectrum of the Higgs boson produced in pp collisions at $\sqrt{s} = 8$ TeV using $H \rightarrow WW$ decays*, *JHEP* **03** (2017) 032, arXiv: [1606.01522 \[hep-ex\]](#) (cit. on p. 74).
- [206] V. Khachatryan et al., *Measurement of the W^+W^- cross section in pp collisions at $\sqrt{s} = 8$ TeV and limits on anomalous gauge couplings*, *Eur. Phys. J.* **C76** (2016) 401, arXiv: [1507.03268 \[hep-ex\]](#) (cit. on p. 74).
- [207] G. Aad et al., *Search for type-III Seesaw heavy leptons in pp collisions at $\sqrt{s} = 8$ TeV with the ATLAS Detector*, *Phys. Rev.* **D92** (2015) 032001, arXiv: [1506.01839 \[hep-ex\]](#) (cit. on p. 74).
- [208] A. M. Sirunyan et al., *Search for dark matter and unparticles in events with a Z boson and missing transverse momentum in proton-proton collisions at $\sqrt{s} = 13$ TeV*, *JHEP* **03** (2017) 061, [Erratum: *JHEP*09,106(2017)], arXiv: [1701.02042 \[hep-ex\]](#) (cit. on p. 74).
- [209] A. M. Sirunyan et al., *Search for new phenomena in final states with two opposite-charge, same-flavor leptons, jets, and missing transverse momentum in pp collisions at $\sqrt{s} = 13$ TeV*, *JHEP* **03** (2018) 076, arXiv: [1709.08908 \[hep-ex\]](#) (cit. on p. 74).
- [210] A. M. Sirunyan et al., *Search for new physics in events with a leptonically decaying Z boson and a large transverse momentum imbalance in proton-proton collisions at $\sqrt{s} = 13$ TeV*, *Eur. Phys. J.* **C78** (2018) 291, arXiv: [1711.00431 \[hep-ex\]](#) (cit. on p. 74).

- [211] A. M. Sirunyan et al., *Search for new physics in events with two soft oppositely charged leptons and missing transverse momentum in proton-proton collisions at $\sqrt{s} = 13$ TeV*, *Phys. Lett.* **B782** (2018) 440, arXiv: [1801.01846 \[hep-ex\]](#) (cit. on pp. 74, 77).
- [212] A. M. Sirunyan et al., *Combined search for electroweak production of charginos and neutralinos in proton-proton collisions at $\sqrt{s} = 13$ TeV*, *JHEP* **03** (2018) 160, arXiv: [1801.03957 \[hep-ex\]](#) (cit. on pp. 74, 76).
- [213] A. M. Sirunyan et al., *Measurements of properties of the Higgs boson decaying to a W boson pair in pp collisions at $\sqrt{s} = 13$ TeV*, Submitted to: *Phys. Lett.* (2018), arXiv: [1806.05246 \[hep-ex\]](#) (cit. on pp. 74, 77).
- [214] A. M. Sirunyan et al., *Search for supersymmetric partners of electrons and muons in proton-proton collisions at $\sqrt{s} = 13$ TeV*, Submitted to: *Phys. Lett.* (2018), arXiv: [1806.05264 \[hep-ex\]](#) (cit. on p. 74).
- [215] A. M. Sirunyan et al., *Searches for pair production of charginos and top squarks in final states with two oppositely charged leptons in proton-proton collisions at $\sqrt{s} = 13$ TeV*, Submitted to: *JHEP* (2018), arXiv: [1807.07799 \[hep-ex\]](#) (cit. on pp. 74, 77).
- [216] M. Aaboud et al., *Search for electroweak production of supersymmetric particles in final states with two or three leptons at $\sqrt{s} = 13$ TeV with the ATLAS detector*, (2018), arXiv: [1803.02762 \[hep-ex\]](#) (cit. on p. 74).
- [217] M. Aaboud et al., *Constraints on off-shell Higgs boson production and the Higgs boson total width in $ZZ \rightarrow 4\ell$ and $ZZ \rightarrow 2\ell 2\nu$ final states with the ATLAS detector*, (2018), arXiv: [1808.01191 \[hep-ex\]](#) (cit. on p. 74).
- [218] A. M. Sirunyan et al., *Search for dark matter produced in association with a Higgs boson decaying to $\gamma\gamma$ or $\tau^+\tau^-$ at $\sqrt{s} = 13$ TeV*, *JHEP* **09** (2018) 046, arXiv: [1806.04771 \[hep-ex\]](#) (cit. on p. 74).
- [219] A. M. Sirunyan et al., *Search for supersymmetry in events with a τ lepton pair and missing transverse momentum in proton-proton collisions at $\sqrt{s} = 13$ TeV*, (2018), arXiv: [1807.02048 \[hep-ex\]](#) (cit. on p. 74).
- [220] M. Aaboud et al., *Search for lepton-flavor violation in different-flavor, high-mass final states in pp collisions at $\sqrt{s} = 13$ TeV with the ATLAS detector*, Submitted to: *Phys. Rev.* (2018), arXiv: [1807.06573 \[hep-ex\]](#) (cit. on p. 74).
- [221] V. Khachatryan et al., *A search for pair production of new light bosons decaying into muons*, *Phys. Lett.* **B752** (2016) 146, arXiv: [1506.00424 \[hep-ex\]](#) (cit. on p. 74).
- [222] A. M. Sirunyan et al., *Measurements of the $pp \rightarrow ZZ$ production cross section and the $Z \rightarrow 4\ell$ branching fraction, and constraints on anomalous triple gauge couplings at $\sqrt{s} = 13$ TeV*, *Eur. Phys. J.* **C78** (2018) 165, [Erratum: *Eur. Phys. J.*C78,no.6,515(2018)], arXiv: [1709.08601 \[hep-ex\]](#) (cit. on pp. 74, 76).
- [223] A. M. Sirunyan et al., *Evidence for associated production of a Higgs boson with a top quark pair in final states with electrons, muons, and hadronically decaying τ leptons at $\sqrt{s} = 13$ TeV*, *JHEP* **08** (2018) 066, arXiv: [1803.05485 \[hep-ex\]](#) (cit. on p. 74).

- [224] M. Aaboud et al., *ZZ → ℓ⁺ℓ⁻ℓ'⁺ℓ'⁻ cross-section measurements and search for anomalous triple gauge couplings in 13 TeV pp collisions with the ATLAS detector*, *Phys. Rev. D* **97** (2018) 032005, arXiv: 1709.07703 [hep-ex] (cit. on p. 74).
- [225] M. Aaboud et al., *Measurement of the Higgs boson coupling properties in the H → ZZ* → 4ℓ decay channel at √s = 13 TeV with the ATLAS detector*, *JHEP* **03** (2018) 095, arXiv: 1712.02304 [hep-ex] (cit. on p. 74).
- [226] M. Aaboud et al., *Search for doubly charged scalar bosons decaying into same-sign W boson pairs with the ATLAS detector*, Submitted to: *Eur. Phys. J.* (2018), arXiv: 1808.01899 [hep-ex] (cit. on p. 74).
- [227] A. M. Sirunyan et al., *Search for an exotic decay of the Higgs boson to a pair of light pseudoscalars in the final state of two muons and two τ leptons in proton-proton collisions at √s = 13 TeV*, (2018), arXiv: 1805.04865 [hep-ex] (cit. on p. 74).
- [228] A. M. Sirunyan et al., *Search for electroweak production of charginos and neutralinos in multilepton final states in proton-proton collisions at √s = 13 TeV*, *JHEP* **03** (2018) 166, arXiv: 1709.05406 [hep-ex] (cit. on pp. 74, 76, 77).
- [229] V. Khachatryan et al., *Search for light bosons in decays of the 125 GeV Higgs boson in proton-proton collisions at √s = 8 TeV*, *JHEP* **10** (2017) 076, arXiv: 1701.02032 [hep-ex] (cit. on p. 74).
- [230] S. R. Mishra et al., *Neutrino tridents and W Z interference*, *Phys. Rev. Lett.* **66** (1991) 3117 (cit. on pp. 76, 78).
- [231] D. Geiregat et al., *First observation of neutrino trident production*, *Phys. Lett.* **B245** (1990) 271 (cit. on p. 76).
- [232] J. P. Lees et al., *Search for a muonic dark force at BABAR*, *Phys. Rev. D* **94** (2016) 011102, arXiv: 1606.03501 [hep-ex] (cit. on p. 76).
- [233] E. J. Chun et al., *Searching for flavored gauge bosons*, *JHEP* **02** (2019) 093, [erratum: *JHEP*07,024(2019)], arXiv: 1811.04320 [hep-ph] (cit. on p. 76).
- [234] S. Agostinelli et al., *GEANT4: A Simulation toolkit*, *Nucl. Instrum. Meth.* **A506** (2003) 250 (cit. on p. 76).
- [235] M. Drees and M. Nojiri, *Neutralino - nucleon scattering revisited*, *Phys. Rev. D* **48** (1993) 3483, arXiv: hep-ph/9307208 [hep-ph] (cit. on p. 109).
- [236] K. Freese, J. A. Frieman, and A. Gould, *Signal Modulation in Cold Dark Matter Detection*, *Phys. Rev. D* **37** (1988) 3388 (cit. on p. 113).

Appendix

A.1 The Cross Section of N - χ Scattering from Contact Operator

In detector experiments, the standard cross section σ_0 is usually used,

$$\sigma_0^{(i)} \equiv \int_0^{4m_r^2 v^2} dq^2 \frac{d\sigma^{(i)}(q=0)}{dq^2} = \int_0^{4m_r^2 v^2} dq^2 \frac{C_i}{\pi v^2}, \quad (\text{A.1})$$

where $m_r = \frac{m_\chi m_N}{m_\chi + m_N}$ is reduced mass, and C_i is defined in 2.7. Then, the final expression is

$$\sigma^{(i)} = \int_0^{4m_r^2 v^2} dq^2 \frac{d\sigma}{dq^2} = \int_0^{4m_r^2 v^2} dq^2 \frac{C_i}{\pi v^2} F_i^2(q^2) = \int_0^{4m_r^2 v^2} dq^2 \frac{\sigma_0^{(i)}}{4m_r^2 v^2} F_i^2(q^2). \quad (\text{A.2})$$

Additionally, we can always use the following expression to generalize the standard cross section to the real cross section,

$$\frac{d\sigma^{(i)}}{dq^2} = \frac{\sigma_0^{(i)}}{4m_r^2 v^2} F_i^2(q^2). \quad (\text{A.3})$$

A.1.1 Contact Operator

The general contact operators for spinor DM are all scalar combinations of

$$\bar{\chi}(1, \gamma^5, \gamma_\mu, \gamma_\mu \gamma^5) \chi \bar{q}(1, \gamma^5, \gamma^\mu, \gamma^\mu \gamma^5) q.$$

To give an example, we calculate the spin-dependent and spin-independent cross section for Majorana DM, which does not have vector couplings, i.e. $\bar{\chi} \gamma^\mu \chi = 0$. Therefore, since the suppression from the low velocity, the most important terms are $S_q \bar{\chi} \chi \bar{q} q$ and $A_q \bar{\chi} \gamma_\mu \gamma^5 \chi \bar{q} \gamma^\mu \gamma^5 q$ for spin-independent and spin-dependent interactions respectively [235]. For m_χ hitting on m_N , $q_{max} = 2m_r v$, where $m_r = \frac{m_\chi m_N}{m_\chi + m_N}$ is reduced mass and $q = p - p'$ is momentum transfer during scattering. For the form factor F , its normalization condition is $F^2(0) = 1$. Moreover, if the nucleus is point-like, $F^2(q^2) = 1$.

A.1.2 Spin-independent Interaction

The effective coupling of spin-independent DM-nucleon interaction is

$$\sum_q S_q \langle N | \bar{q}q | N \rangle = \sum_q S_q \lambda_q \bar{N}N, \quad (\text{A.4})$$

where λ_q describes how quarks form the certain nucleon. Therefore, it can be measured experimentally through nuclear physics. Obviously, it should be the same for protons and neutrons in nucleus for different quarks. Therefore,

$$\mathcal{L}^{(1)} = \sum_q S_q \lambda_q \bar{\chi}\chi \bar{N}N, \quad (\text{A.5})$$

$$\Rightarrow \text{For proton, } \sum_q S_q \lambda_q \bar{\chi}\chi \bar{N}N \equiv f_p \bar{\chi}\chi \bar{p}p; \quad (\text{A.6})$$

$$\Rightarrow \text{For neutron, } \sum_q S_q \lambda_q \bar{\chi}\chi \bar{N}N \equiv f_n \bar{\chi}\chi \bar{n}n. \quad (\text{A.7})$$

For nucleus scattering amplitude, we should sum up all protons and neutrons components inside. Thus,

$$C_s = (Zf_p + (A - Z)f_n)^2. \quad (\text{A.8})$$

From the definition in A.1,

$$\sigma_0^{(1)} = \int_0^{4m_r^2 v^2} dq^2 \frac{C_s}{\pi v^2} = \frac{4m_r^2}{\pi} (Zf_p + (A - Z)f_n)^2. \quad (\text{A.9})$$

Then, according to formula A.3, the final expression is

$$\sigma^{(1)} = \int_0^{4m_r^2 v^2} dq^2 \frac{d\sigma}{dq^2} = \int_0^{4m_r^2 v^2} dq^2 \frac{C_s}{\pi v^2} F^2(q^2) = \int_0^{4m_r^2 v^2} dq^2 \frac{\sigma_0^{(1)}}{4m_r^2 v^2} F^2(q^2). \quad (\text{A.10})$$

If the nucleus is not point-like, we need to know form factor explicitly. For spin-independent interaction, form factor can be chosen approximately as an exponential distribution.

A.1.3 Spin-dependent Interaction

Similarly with spin-independent interaction, we need to find C_A , beginning from

$$\sum_q A_q \langle N | \bar{q}\gamma_\mu \gamma^5 q | N \rangle = \sum_q A_q \Delta_q \bar{N}S_\mu N, \quad (\text{A.11})$$

where Δ_q is the quark content of nucleon, which can be measured experimentally from the scattering of electron and nucleon, and S_μ is the spin vector. Therefore the effective Lagrangian is,

$$\mathcal{L}^{(2)} = \sum_q A_q \Delta_q \bar{\chi}\gamma^\mu \gamma^5 \chi \bar{N}S_\mu N. \quad (\text{A.12})$$

Using $|MJ\rangle$ to express nucleus M with total angular momentum J , we can use the effective Lagrangian of DM–nucleon scattering to write the DM–nucleus scattering amplitude,

$$|\mathcal{M}|^2 = |\langle MJ|\mathcal{L}|MJ\rangle|^2 = \langle J^2 \rangle \left| \sum_{\text{nuclei}} \sum_q A_q \Delta_q \frac{\langle S \rangle}{J} \right|^2, \quad (\text{A.13})$$

where J is total angular momentum, and $\frac{\langle S \rangle}{J}$ is fraction of spin component. Moreover, to distinguish between the neutron and proton, we need to define parameter for them respectively, i.e.

$$\sum_{\text{protons}} \sum_q A_q \Delta_q \frac{\langle S \rangle}{J} = a_p \frac{\langle S_p \rangle}{J}, \quad \langle S_p \rangle = \langle M_p | S_\mu | M_p \rangle, \quad a_p = \left(\sum_q A_q \Delta_q \right)_{\text{proton}}; \quad (\text{A.14})$$

$$\sum_{\text{neutrons}} \sum_q A_q \Delta_q \frac{\langle S \rangle}{J} = a_n \frac{\langle S_n \rangle}{J}, \quad \langle S_n \rangle = \langle M_n | S_\mu | M_n \rangle, \quad a_n = \left(\sum_q A_q \Delta_q \right)_{\text{neutron}}; \quad (\text{A.15})$$

$$\Rightarrow C_A = \langle J^2 \rangle \left| a_p \frac{\langle S_p \rangle}{J} + a_n \frac{\langle S_n \rangle}{J} \right|^2 = J(J+1)\Lambda^2, \quad \Lambda = \frac{1}{J}(a_p \langle S_p \rangle + a_n \langle S_n \rangle). \quad (\text{A.16})$$

Using the new parameters we defined, we find the expression of standard cross section for spin-dependent interaction,

$$\sigma_0^{(2)} = \int_0^{4m_r^2 v^2} dq^2 \frac{d\sigma(q=0)}{dq^2} = \int_0^{4m_r^2 v^2} dq^2 \frac{C_A}{\pi v^2} = \frac{4m_r^2}{\pi} \Lambda^2 J(J+1), \quad (\text{A.17})$$

and it can be generalized to $\sigma^{(2)}$ through formula A.3.

A.2 Interaction Rates in Detector

A.2.1 General Formula

The interaction rate, which is the relevant quantity for direct search experiments, and is usually measured in events/(kg * day), takes the form

$$dR = \frac{\rho_0}{m_\chi m_N} v f(v) dv d\sigma \Rightarrow MdR = \frac{\rho_0}{m_\chi} N v f(v) dv d\sigma, \quad (\text{A.18})$$

where MdR is the total interaction rate in our detector, $\frac{\rho_0}{m_\chi}$ is the number density of χ , and $N \equiv \frac{M}{m_N}$ is the total number of nuclei in detector. For the velocity distribution $f(v)$, its normalization condition is $\int_0^\infty f(v) dv = 1$. We use recoil energy, $Q = q^2/(2m_N)$, instead of the momentum transfer q . In center of momentum frame,

$$q^2 = 2m_r^2 v^2 (1 - \cos \theta) \Rightarrow Q = \frac{q^2}{2m_N} = \frac{m_r^2 v^2}{m_N} (1 - \cos \theta) \Rightarrow dQ = \frac{dq^2}{2m_N}, \quad (\text{A.19})$$

and the lower and upper limits are

$$v_{min} = \sqrt{\frac{2Qm_N}{m_r^2}}, \quad v_{max} \rightarrow \infty. \quad (\text{A.20})$$

Therefore,

$$\frac{dR}{dQ} = \frac{2\rho_0}{m_\chi} v f(v) dv \frac{d\sigma}{dq^2} = \frac{2\rho_0}{m_\chi} v f(v) dv \frac{\sigma_0}{4m_r^2 v^2} F^2(Q) = \frac{\rho_0 \sigma_0}{2m_r^2 m_\chi} F^2(Q) \frac{f(v)}{v} dv, \quad (\text{A.21})$$

then integrate from $v_{min} = \sqrt{\frac{Qm_N}{2m_r^2}}$ to $v_{max} \rightarrow \infty$,

$$\frac{dR}{dQ} = \frac{\rho_0 \sigma_0}{2m_r^2 m_\chi} F^2(Q) \int_{v_{min}}^{\infty} \frac{f(v)}{v} dv, \quad (\text{A.22})$$

$$\Rightarrow R = \frac{\rho_0 \sigma_0}{\sqrt{\pi} v_0 m_\chi m_r^2} \int_{E_T}^{E_{max}} T(Q) F^2(Q) dQ, \quad T(Q) = \frac{\sqrt{\pi}}{2} v_0 \int_{v_{min}}^{\infty} \frac{f(v)}{v} dv, \quad (\text{A.23})$$

where $T(Q)$ is a dimensionless parameter, $v_0 = 220$ km/s is circular speed of the sun around galactic center, and recoil energy Q is from E_T to E_{max} .

A.2.2 A Simple Case for Maxwellian Halo

Maxwellian halo has a Gaussian velocity distribution,

$$f'(\vec{v}) d^3v = \left(\frac{1}{v_0 \sqrt{\pi}} \right)^3 e^{-v^2/v_0^2} d^3v \rightarrow 4\pi v^2 dv \left(\frac{1}{v_0 \sqrt{\pi}} \right)^3 e^{-v^2/v_0^2} = \frac{4v^2}{\sqrt{\pi} v_0^3} e^{-v^2/v_0^2} dv = f(v) dv. \quad (\text{A.24})$$

From the velocity distribution, we firstly calculate the dimensionless parameter $T(Q)$ and differential interaction rate,

$$T(Q) = \frac{\sqrt{\pi}}{2} v_0 \int_{v_{min}}^{\infty} \frac{4v}{\sqrt{\pi} v_0^3} e^{-v^2/v_0^2} dv = e^{-v_{min}^2/v_0^2} = e^{-\frac{m_N Q}{2m_r^2 v_0^2}}, \quad (\text{A.25})$$

$$\Rightarrow \frac{dR}{dQ} = \frac{\rho_0 \sigma_0}{\sqrt{\pi} v_0 m_\chi m_r^2} e^{-\frac{m_N Q}{2m_r^2 v_0^2}} F^2(Q). \quad (\text{A.26})$$

Moreover, if we only consider the threshold energy E_T without the upper limit of energy, and use the simplest point-like condition, $F^2 = 1$, the formula reduces to

$$\Rightarrow R = \frac{\rho_0 \sigma_0}{\sqrt{\pi} v_0 m_\chi m_r^2} \int_{E_T}^{\infty} dQ e^{-\frac{m_N Q}{2m_r^2 v_0^2}} = \frac{2\rho_0 \sigma_0 v_0^2}{\sqrt{\pi} m_\chi m_N} e^{-\frac{E_T m_N}{2m_r^2 v_0^2}}. \quad (\text{A.27})$$

Therefore, we can compare the observed R with the model related σ_0 and m_χ . If we consider the relative velocity between sun and earth, the calculation of the total R is more complicated.

A.2.3 Relative Movement Between Earth and Sun

If we consider not only the circular motion of the Sun around galactic center, but also the motion between the Sun and the Earth, the total the velocity is

$$\vec{v} = \vec{v}_e + \vec{v}_\chi, \quad (\text{A.28})$$

where v_χ is the velocity of DM in our experimental frame. From Ref. [236], we know

$$v_e = v_0 \left(1.05 + 0.07 \cos\left(2\pi\left(t - \frac{153 \pm 1.3}{365}\right)\right) \right), \quad t = \frac{\text{time}}{1 \text{ year}}; \quad (\text{A.29})$$

$$f(v_\chi)dv_\chi = \frac{v_\chi dv_\chi}{\sqrt{\pi}v_e v_0} \left(\exp\left(-\frac{(v_\chi - v_e)^2}{v_0^2}\right) - \exp\left(-\frac{(v_\chi + v_e)^2}{v_0^2}\right) \right). \quad (\text{A.30})$$

Therefore, we can repeat the integration procedure in formula A.25 and A.27 to find $T(Q)$ and R , i.e.

$$T(Q) = \frac{\sqrt{\pi}}{2} v_0 \int_{v_{min}}^{\infty} \frac{dv_\chi}{v_e v_0 \sqrt{\pi}} \left(\exp\left(-\frac{(v_\chi - v_e)^2}{v_0^2}\right) - \exp\left(-\frac{(v_\chi + v_e)^2}{v_0^2}\right) \right) \quad (\text{A.31})$$

$$\begin{aligned} &= \frac{\sqrt{\pi}v_0}{4v_e} \int_{v_{min}}^{\infty} d\frac{v_\chi}{v_0} \frac{2}{\sqrt{\pi}} \left(\exp\left(-\frac{(v_\chi - v_e)^2}{v_0^2}\right) - \exp\left(-\frac{(v_\chi + v_e)^2}{v_0^2}\right) \right) \\ &= \frac{\sqrt{\pi}v_0}{4v_e} \left(\text{erf}\left(\frac{v_{min} + v_e}{v_0}\right) - \text{erf}\left(\frac{v_{min} - v_e}{v_0}\right) \right); \end{aligned}$$

$$R = \frac{\rho_0 \sigma_0}{4v_e m_\chi m_r^2} \int_{E_T}^{E_{max}} dQ \left(\text{erf}\left(\frac{v_{min} + v_e}{v_0}\right) - \text{erf}\left(\frac{v_{min} - v_e}{v_0}\right) \right) F^2(Q). \quad (\text{A.32})$$

Again using $F^2 = 1$ for point-like case, we can integrate out the formula analytically. The integration for the first term is

$$\begin{aligned} \int_{E_T}^{E_{max}} dQ \text{erf}\left(\sqrt{\frac{m_N Q}{2m_r^2 v_0^2}} + \frac{v_e}{v_0}\right) &= \int_{E_T}^{E_{max}} d\frac{Qm_N}{2m_r^2 v_0^2} \frac{2m_r^2 v_0^2}{m_N} \text{erf}\left(\sqrt{\frac{m_N Q}{2m_r^2 v_0^2}} + \frac{v_e}{v_0}\right) \\ &= \frac{2m_r^2 v_0^2}{m_N} \int_a^b dx \text{erf}(\sqrt{x} + c) \equiv \frac{2m_r^2 v_0^2}{m_N} \Pi_+, \end{aligned} \quad (\text{A.33})$$

where $x(E) = Em_N/2m_r^2 v_0^2$, $a = x(E_T)$, $b = x(E_{max})$, and $c = v_e/v_0$. Therefore,

$$\begin{aligned} \Pi_+ &= \frac{1}{\sqrt{\pi}} \left((\sqrt{b} - c) \exp(-(\sqrt{b} + c)^2) - (\sqrt{a} - c) \exp(-(\sqrt{a} + c)^2) \right) \\ &\quad - \frac{1}{2} \left((1 - 2b + 2c^2) \text{erf}(\sqrt{b} - c) - (1 - 2a + 2c^2) \text{erf}(\sqrt{a} - c) \right). \end{aligned} \quad (\text{A.34})$$

Taking $c \rightarrow -c$, we find Π_- , and the total interaction rate is therefore

$$R = \frac{\rho_0 \sigma_0 v_0^2}{2v_e m_\chi m_N} (\Pi_+ - \Pi_-).$$

Since v_e changes yearly, the interaction rate R also periodically changes, and it reaches the peak on June 02 approximately.

A.3 Best Cut Efficiencies of LEP Analysis

The tables list the best cut efficiencies that we get from all LEP analysis referenced in chapter 3 for our model described in the same chapter.

$m_R = 5 \text{ GeV}$				
m_χ/GeV	2.5	3.0	3.5	4.0
ϵ	7.67%	11.63%	14.32%	16.17%
m_χ/GeV	4.5	5	5.5	6.0
ϵ	16.18%	15.80%	13.44%	13.67%
m_χ/GeV	6.5	7.0	7.5	8.0
ϵ	13.67%	13.54%	12.88%	12.70%
m_χ/GeV	8.5	9.0	9.5	10.0
ϵ	12.72%	12.51%	13.06%	13.20%

Table A.1: Cut efficiencies for $m_R = 5 \text{ GeV}$. The efficiencies are around 13%, and are normally not enough for the signal. We have assumed pure axial vector coupling, $g_q^V = g_\chi^V = 0$.

$m_R = 2 \text{ GeV}$				
m_χ/GeV	1.0	1.2	1.4	1.6
ϵ	10.29%	13.61%	14.53%	15.82%
m_χ/GeV	1.8	2.0	2.2	2.4
ϵ	16.30%	16.57%	17.40%	17.64%
m_χ/GeV	2.6	2.8	3.0	3.2
ϵ	19.19%	19.59%	19.11%	18.85%
m_χ/GeV	3.4	3.6	3.8	4.0
ϵ	19.94%	16.50%	14.93%	15.63%

Table A.2: Cut efficiencies for $m_R = 2 \text{ GeV}$. The efficiencies are better than those of 5 GeV in general. We have assumed pure axial vector coupling, $g_q^V = g_\chi^V = 0$.

$m_R = 1 \text{ GeV}$				
m_χ/GeV	0.5	0.6	0.7	0.8
ϵ	11.86%	13.99%	14.57%	15.34%
m_χ/GeV	0.9	1.0	1.1	1.2
ϵ	14.89%	14.92%	16.14%	16.19%
m_χ/GeV	1.3	1.4	1.5	1.6
ϵ	16.24%	16.31%	16.56%	16.30%
m_χ/GeV	1.7	1.8	1.9	2.0
ϵ	17.13%	17.06%	17.62%	18.02%

Table A.3: Cut efficiencies for $m_R = 1 \text{ GeV}$. The result is similar with the case $m_R = 2 \text{ GeV}$. We have assumed pure axial vector coupling, $g_q^V = g_\chi^V = 0$.

m/GeV	$m_R = 5$	2	1
$m_\chi = 4$	16.17%	15.63%	14.15%
4.5	16.18%	12.69%	12.68%
5	15.80%	12.07%	12.84%
5.5	13.44%	11.64%	12.92%
6	13.67%	12.50%	12.00%
6.5	13.67%	11.30%	11.65%
7	13.54%	11.07%	11.99%
7.5	12.88%	11.30%	11.46%
8	12.70%	11.07%	11.34%
8.5	12.72%	11.55%	11.75%
9	12.51%	11.39%	11.53%
9.5	13.06%	11.21%	11.25%
10	13.20%	11.84%	11.42%

Table A.4: Comparison for various values of m_R . We have assumed pure axial vector coupling, $g_q^V = g_\chi^V = 0$.

183 GeV Experiment					
m_R/GeV	1.0	1.5	2.0	2.5	3.0
ϵ	27.73%	27.58%	27.30%	27.57%	27.77%
m_R/GeV	3.5	4.0	4.5	5.0	5.5
ϵ	27.37%	27.14%	27.47%	26.96%	26.24%
m_R/GeV	6.0	6.5	7.0	7.5	8.0
ϵ	26.77%	25.62%	25.69%	24.74%	25.08%
m_R/GeV	8.5	9.0	9.5	10.0	10.5
ϵ	24.51%	23.13%	18.80%	18.93%	18.19%
m_R/GeV	11.0	11.5	12.0	12.5	13.0
ϵ	19.24%	19.28%	19.15%	19.55%	19.69%
m_R/GeV	13.5	14.0	14.5	15.0	
ϵ	19.31%	20.05%	20.35%	19.71%	

Table A.5: Cut efficiencies of our signal from 4-jet topology in ZH search. We have assumed pure axial vector coupling, $g_q^V = 0$.

209 GeV Experiment					
m_R/GeV	1.0	1.5	2.0	2.5	3.0
ϵ	21.87%	22.18%	22.23%	21.95%	21.81%
m_R/GeV	3.5	4.0	4.5	5.0	5.5
ϵ	21.83%	22.49%	22.23%	21.32%	21.54%
m_R/GeV	6.0	6.5	7.0	7.5	8.0
ϵ	21.05%	20.65%	20.75%	19.74%	19.12%
m_R/GeV	8.5	9.0	9.5	10.0	
ϵ	19.15%	18.40%	14.24%	14.17%	

Table A.6: Cut efficiencies of our signal from 4-jet topology in ZH search. Every value is lower than the corresponding one of 183 GeV. We have assumed pure axial vector coupling, $g_q^V = 0$.

List of Figures

1.1	Quarks (red), Leptons (green), gauge bosons (blue), and the Higgs boson in Standard Model.	6
1.2	The figure summarizes the experiments of DM. The direct detection focuses on the scattering between nuclei (SM particles) and DM particles. The indirect detection focuses on the SM products from DM annihilation. The collider searches focus on the collision of the SM particles that have DM particles in the final states.	7
2.1	The visible lights with different colors show galaxies. The pink area is the X-ray photo. The blue area is the mass distribution from gravitational lensing. If we assume the luminous mass approximately agrees the baryonic matter shown by the X-ray photo, the luminous mass is obviously distinct from the total mass.	13
2.2	The figure is the bound of spin-independent cross sections. The lines above are the exclusion plot for 90% CL, while the dashed line is the neutrino floor from the measurement of the background in coherent $N\nu$ scattering. The bound for spin-independent interaction is on the sum of neutron and proton, e.g. C_s in A.1.	14
2.3	The figure is the bound of spin-dependent cross sections. The upper figure is for neutron, while the lower figure is for proton.	20
2.4	Upper figure is Messier 101, an example of spiral galaxy. It is clear to see the bulge in the center, and the spiral arm extended from the center. Lower figure is rotation curve of Messier 33 [85]. The expected curve and the observed curve are obviously distinct, especially in the large distance area.	21
2.5	The result in the first figure is based on the data collected by Wilkinson Microwave Anisotropy Probe (WMAP) in 9 years [91]. More red means hotter, while more blue means colder in the figure. The second figure is the comparison between the best theoretical estimation from Λ -CDM model and the recent observation [90]. In the upper part of the second figure, the definition of y -axis is $D_l = l(l + 1)C_l/2\pi$, while x -axis is multipole l . The blue points are the maximum-likelihood estimates from the observed data by Planck satellite. The red line is the best fit from Λ -CDM model. Additionally, the lower part of the second figure shows the residuals.	22
2.6	The figure shows the “Freeze out” procedure of DM. It does not use time (t) and number density (n) directly. In the figure, $x \equiv m/T$, where m is the mass of DM and T is the temperature, and $Y \equiv n/s$, where n is the number density of DM and s is the entropy. Along with the increasing time, the temperature should decrease, meaning larger x . Additionally, n and s decrease simultaneously, as the expansion of the universe. Therefore, it is better to use Y to show the constant tail.	23

3.1	Leading order diagrams contributing to the final state (3.16) in our model. Note that the mediator R is always off-shell in the region of parameter space we are interested in.	34
3.2	The upper frame depicts the bound on $\sqrt{g_q g_\chi}$. The solid (green) curve shows the bound on g^A from the unitarity condition (3.15). The dashed (red) curve shows the bound on g^A from the combination of the unitarity condition and our recasting of the ALEPH squark pair search limits. The lower frame shows the upper bound on the total signal cross section at $\sqrt{s} = 208$ GeV from our recasting of the ALEPH limits. In these figures the mass of the mediator $m_R = 1$ GeV. Here all vector couplings have been set to zero, i.e. $g_q = g_q^A$, $g_\chi = g_\chi^A$.	46
3.3	The meaning of the curves in the lower frames, and of the solid and dashed curves in the upper frames, is as in Fig. 3.2, but for mediator mass $m_R = 2$ GeV. For $m_\chi \geq 3.6$ GeV the solid and dashed curves coincide, i.e. the unitarity condition gives the stronger bound on the axial vector coupling. The dotted (blue) lines show the upper bound on the vector coupling that we derive from the ALEPH search, i.e. for these curves, $g_q g_\chi = g_q^V g_\chi^V$; the axial vector couplings were chosen such that the unitarity limit is saturated. In this mass range the upper bound on the signal cross section shown in the lower frames also uses the maximal axial vector coupling allowed by unitarity.	47
3.4	The meaning of the curves in the lower frames, and of the solid and dashed curves in the upper frames, is as in Fig. 3.2, but for mediator mass $m_R = 5$ GeV. For $m_\chi \geq 4.5$ GeV the solid and dashed curves coincide, i.e. the unitarity condition gives the stronger bound on the axial vector coupling. The dotted (blue) lines show the upper bound on the vector coupling that we derive from the ALEPH search, i.e. for these curves, $g_q g_\chi = g_q^V g_\chi^V$; the axial vector couplings were chosen such that the unitarity limit is saturated. In this mass range the upper bound on the signal cross section shown in the lower frames also uses the maximal axial vector coupling allowed by unitarity.	48
3.5	The upper frame depicts the bound on $\sqrt{g_q^V g_\chi^V}$, while the lower one shows the upper bound on the total signal cross section at $\sqrt{s} = 208$ GeV from our recasting of the ALEPH limits; all axial vector couplings have been set to zero. The green, blue and red curves are for $m_R = 5, 2$ and 1 GeV, respectively. For $m_\chi > 30$ GeV the bound on g^V is weaker than the perturbativity condition (3.14).	49
3.6	The upper frame shows upper bounds on the couplings of the mediator. The solid lines are from the unitarity condition (3.15), while the dashed lines are from our recasting of the ALEPH squark search; both sets of curves refer to axial vector couplings. If the unitarity constraint is stronger, we allow non-vanishing vector couplings; their upper bounds, derived from the ALEPH data, are shown by the dot-dashed curves. If $g^A = 0$, the unitarity condition are irrelevant, and the bounds on g^V become weaker. They are shown by the dotted curves. The green, blue and red curves are for $m_R = 5, 2$ and 1 GeV, respectively. The lower frame shows the corresponding upper bound on the total signal cross section before cuts at $\sqrt{s} = 208$ GeV.	50

3.7 The upper frame depicts bounds on couplings of the mediator. The solid lines show the unitarity bound on the axial vector coupling. The other curves depict bounds from our recasting of the ALEPH LEP1 limits. The dotted lines are the upper limits on g^V for $g^A = 0$, while the dashed lines are the upper limits on g^A for $g^V = 0$. The purple, green, blue and red curves are for $m_R = 10, 5, 2$ and 1 GeV, respectively. For $m_\chi > 30$ GeV the bound on g^V is always weaker than the perturbativity condition (3.14). For $m_\chi > 23$ GeV the LEP1 bound on g^A is weaker than the unitarity condition (3.15), and is therefore not shown any more. The lower frame shows the upper bound on the total signal cross section at $\sqrt{s} = 91$ GeV; we use the same conventions as in the upper frame. 51

3.8 Bounds on the (axial) vector coupling to b quarks (upper) and total cross section (lower) we derive from our recasting of the ALEPH Higgs searches in the 4-jet channel. In both frames the lower (red) curves correspond to data taken at $\sqrt{s} = 183$ GeV, while the upper (blue) curves correspond to data taken at $\sqrt{s} = 209$ GeV. The dashed curves have been obtained with vanishing vector couplings, while the dot-dashed curves are for $g_q^V = 1$. The dotted magenta curves show the upper bounds for vanishing axial vector couplings. The solid (green) curve in the upper frame shows the upper bound on g_b^A from the unitarity constraint (3.15) applied to the b quark. 52

3.9 Upper bounds on the couplings (upper) and total cross section (lower) from our re-casting of an ALEPH LEP2 4-jet analysis. The notation is as in Fig. 3.8, except that we only show results for the analysis at $\sqrt{s} = 183$ GeV which again has the highest sensitivity. For $g^A = 0$, shown by the dotted curve, the LEP2 bound is only stronger than the perturbativity condition (3.14) if $m_R < 35$ GeV. The unitarity bound on g_b^A becomes weaker for higher m_R , and is no longer relevant. However, for $m_\chi > 70$ GeV the perturbativity condition is stronger than our “experimental” bound, both for $g_q^V = 0$ and for $g_q^V = 1$ 53

4.1 Examples of Feynman diagrams contributing to mono-jet + \cancel{E}_T (left), di-jet + \cancel{E}_T (center) and di-jet resonance (right) final states; in the former two cases it is assumed that the mediator R decays into two dark sector particles, which escape detection, whereas in the latter case R is assumed to decay into a quark antiquark pair. The diagram to the right is unique (with different initial states contributing), and the one on the left is unique up to crossing; however, many additional diagrams, with different combinations of partons in the initial and final states and different propagators, contribute to R +di-jet production. 60

4.2 Loop diagrams contributing to R +jet production from gluon fusion. 62

- 4.3 The upper frame shows the bound on the squared coupling of the mediator to quarks times the relevant branching ratio of the mediator that we derive by recasting various LHC bounds (dashed and dot-dashed curves). The lower solid curve shows the unitarity bound (4.1) on the axial vector coupling, and the thin solid lines in the top-left corner show constraints from recast LEP constraints in Chapter 3 based on analyses by the ALEPH collaboration. For $g^A = 0$ only vector couplings g_q^V are allowed with $q = s, c, b, t$, while for $g^V = 0$ only axial vector couplings g_q^A are allowed with $q = b, t$. LHC missing E_T results are from the combination of mono-jet and multi-jet analyses. The lower frame shows the upper bound on the total cross sections from the missing E_T analyses. 66
- 5.1 Examples of Feynman diagrams for $pp \rightarrow Z' l^+ l^-$ (left), $pp \rightarrow Z' \nu_l \bar{\nu}_l$ (center) and $pp \rightarrow Z' l \nu_l$ (right). For the left diagram, both visible (leptonic) and invisible Z' decays (into neutrinos or DM particles) contribute to signal processes, but for the central and right diagram only Z' decays into a charged lepton pair were considered. The Z' boson can also be emitted off the other lepton, and W^+ exchange diagrams also contribute. In the event generation the Z' is allowed to be off-shell. 74
- 5.2 The upper limit on the new coupling $g_{\mu\tau}$ (upper) and the corresponding cross section before cuts (lower). The upper frame also shows the value of the coupling indicated by the measurement of the anomalous magnetic moment of the muon (shaded area), as well as a summary of existing constraints (lower dot-dashed curve); see the text for further details. 79
- 5.3 The effect of Z' decays into dark matter particles on the constraint from $2l$ final states, for $g_{\mu\tau} = 1$ and $q_{\text{DM}} = 1$ (upper) and 2 (lower). In the gray region below the diagonal these decays are kinematically forbidden, i.e. the result of Fig. 5.2 holds. The green region is excluded by analyses of 2μ final states at $\sqrt{s} = 13$ TeV; in the absence of $Z' \rightarrow \text{DM}$ decays these analyses exclude the region between the horizontal lines. The pink region is excluded by analyses of 4μ final states, which are only mildly affected by $Z' \rightarrow \text{DM}$ decays; this includes the entire green region. 80
- 6.1 The figure shows the feature importance from XGBoost. The x -axis is the variables with leading importance we use in our Machine Learning. Larger importance means more important variables. E , p_x , p_y , p_z , and p_T are the 4-momenta and transverse momentum of the final state leptons and the most energetic jet, while the number 0 – 2 means the position in the energetic series. η and ϕ are the angular position of final state objects. Missing p_T is the missing transverse momentum. m_T and m_{T2} are 2 kinds of transverse mass, H_T is the scalar sum of jet transverse momenta, and $m_{\mu^+\mu^-}$ is the invariant mass of the di-muon pair that minimize the value of $|m_Z - m_{\mu^+\mu^-}|$ 84
- 6.2 The figure shows the optimized bound from $3l$ -signal. The upper figure drops all the signal and background data with $\cancel{p}_T > 100$ GeV before training, while the lower figure drops data with $\cancel{p}_T > 10$ GeV. 85

List of Tables

3.1	Cuts designed to reduce the SM background to the two jet plus missing E_T signal. The cuts listed above the last horizontal double line are mostly directed against two-photon events, whereas the cuts below this double line help to remove background events containing on-shell W or Z bosons. See the text for further details.	41
3.2	Cut Efficiencies for $m_R = 5$ GeV and $m_R/2 \leq m_\chi \leq 2m_R$. ϵ_A has been computed with pure axial vector coupling, $g_q^V = g_\chi^V = 0$, while ϵ_V is the efficiency for pure vector coupling, assumed to be the same for s, c and b quarks, while $g_\chi^A = g_q^A = 0$	43
3.3	Cut Efficiencies for $m_R = 2$ GeV and $m_R/2 \leq m_\chi \leq 2m_R$. We have assumed pure axial vector coupling, $g_q^V = g_\chi^V = 0$	44
3.4	Cut Efficiencies for $m_R = 1$ GeV and $m_R/2 \leq m_\chi \leq 2m_R$. We have assumed pure axial vector coupling, $g_q^V = g_\chi^V = 0$	44
5.1	All analyses used in this chapter for leptophilic mediator.	74
A.1	Cut efficiencies for $m_R = 5$ GeV. The efficiencies are around 13%, and are normally not enough for the signal. We have assumed pure axial vector coupling, $g_q^V = g_\chi^V = 0$	114
A.2	Cut efficiencies for $m_R = 2$ GeV. The efficiencies are better than those of 5 GeV in general. We have assumed pure axial vector coupling, $g_q^V = g_\chi^V = 0$	114
A.3	Cut efficiencies for $m_R = 1$ GeV. The result is similar with the case $m_R = 2$ GeV. We have assumed pure axial vector coupling, $g_q^V = g_\chi^V = 0$	115
A.4	Comparison for various values of m_R . We have assumed pure axial vector coupling, $g_q^V = g_\chi^V = 0$	115
A.5	Cut efficiencies of our signal from 4-jet topology in ZH search. We have assumed pure axial vector coupling, $g_q^V = 0$	116
A.6	Cut efficiencies of our signal from 4-jet topology in ZH search. Every value is lower than the corresponding one of 183 GeV. We have assumed pure axial vector coupling, $g_q^V = 0$	116